A NOTE

The authors would appreciate receiving your comments on the attached research report. Additional copies of the report are available to those interested. Please send your comments and report requests to:

Professor S. Shyam Sunder
Department of Civil Engineering
Massachusetts Institute of Technology
77 Massachusetts Avenue, Rm 1-274
Cambridge, Massachusetts 02139, USA

Telephone: (617) 253-7118

Errata: Please read "high homologous temperatures" for "thermorheologically high temperatures" on Page 23 and elsewhere in the text.

CONSTITUTIVE MODELING OF SEA ICE WITH APPLICATIONS TO INDENTATION PROBLEMS

by

Seng-Kiong Ting
Graduate Research Assistant

S. Shyam Sunder
Winslow Associate Professor of Civil Engineering

CENTER FOR SCIENTIFIC EXCELLENCE
IN OFFSHORE ENGINEERING

CSEOE Research Report No. 3
Department of Civil Engineering Research Report No. R85-15
Constructed Facilities Division Order No. 779

Prepared for

THE STANDARD OIL COMPANY (OHIO)
MINERALS MANAGEMENT SERVICE, US DOI

October, 1985

The finite element formulation for general viscoplastic behavior (including nonlinear viscoelasticity) is based on the displacement method and is derived from a weighted equilibrium -rate equation. A bi-level solution algorithm, which enables (fast) convergence in problems where inelastic deformations dominate, has been developed to solve the pseudo-force form of the nonlinear governing equations. At each time step, a successive substituion type iteration is applied to the system (global) equations of motion while a Newton-Raphson or tangent type nonlinear equation solver combined with the α-method of numerical time integration is applied to the constitutive equation at the Gauss integration points in the finite element grid. Variable interface conditions between the ice feature and the structure can be simulated to bound the effects of interface adfreeze and friction. In particular, a "free" interface condition, which represents no interface adfreeze or friction, is simulated by an adaptive procedure that prevents normal tensile stresses from developing at the interface.

The interaction of an ice sheet with a vertically faced indenter is an important loading condition in the Arctic for cylindrical structures and for conical structures with grounded rubble pile or accreted ice foot. Numerical simulations are performed under plane stress conditions to study the sea ice indentation problem under steady state creep conditions. The major factors affecting ice load prediction during indentation are identified and the relative magnitude of the various sources of uncertainty is assessed. Among the factors addressed are: (i) choice of material model for describing the mechanical behavior of sea ice, i.e., isotropic versus anisotropic, pressure-sensitive versus pressure -insensitve and plastic versus nonlinear viscoelastic; (ii) influence of natural variability in the mechanical properties of sea ice; (iii) the choice between approximate (bound and strain path) and "exact" methods of analysis for predicting global forces and local pressures and the ability of each to model interface adfreeze and friction, and spatial and temporal variability of the strainrate field; (iv) the influence of grounded rubble pile or accreted ice foot; and (v) the prediction of local pressures or pressure-area curves that are used in the design of structural members.

FOREWORD

The grant by The Standard Oil Company (Ohio) to establish a Center for Scientific Excellence in Offshore Engineering at MIT is shared by the Department of Civil Engineering and the Department of Ocean Engineering. Initiated in September 1983, the Center provides $400,000 per year to support coordinated research in collaboration with Sohio to develop the technology necessary for an overall evaluation of alternative structural concepts for offshore oil exploration and production platforms located in the extreme environmental conditions of the North American Arctic. This interdisciplinary effort encompasses basic and applied research on ice & structural, geotechnical, risk & reliability, and hydrodynamic aspects of Arctic offshore engineering.

This report summarizes the progress todate on a project entitled "Numerical Modeling of Ice-Strucutre Interaction" funded by the Center at a level of $75,000 per year for the period 1983-88 and by the Minerals Management Service of the U.S. Department of the Interior at a level of $60,000 per year for the period 1984-87. The project involves the following three major areas of study:

- Development of constitutive models to characterize the mechanical behavior of sea ice.
- Development of finite element methods of analysis to account for the simultaneous occurrence of viscous (rate-dependent) and fracture behavior in ice, and variable conditions of contact between ice and structure.
- Numerical simulation of ice-structure interaction processes for selected ice features and structural configurations to predict global forces and local pressures.

The principal investigators for the project are Professor S. Shyam Sunder and Professor Jerome J. Connor. The following graduate students have participated in this project: Dr. Seng-Kiong Ting, Mr. Fadi S. Chehayeb and Mr. Jaideep Ganguly.

The authors of this report would like to express their gratitude to the following for their support and encouragement: Professors Jerome Connor, Charles Ladd, Mohsen Baligh, Tomasz Wierzbicki and Daniele Veneziano at MIT; Mr. Terry Walden of Sohio and Mr. Charles Smith of MMS; Professor Erland Schulson of Dartmouth College; Professor William Sackinger of University of Alaska; Drs. Devinder Sodhi, Jerome Johnson, Gordon Cox and Ms. Jacqueline Richter-Menge of USA CRREL; Dr. Ken Croasdale of Croasdale and

Associates; Dr. Ian Jordaan of DnV (Canada); Dr. Vitoon Vivatrat of Brian Watt Associates; Dr. Tony Wang of Exxon; Mr. John Krieder of ARCTEC; and Dr. Michael Rojansky of Ben Gerwick Inc.

TABLE OF CONTENTS

	Page
ABSTRACT	1
FOREWORD	3
TABLE OF CONTENTS	5
LIST OF FIGURES	8
LIST OF TABLES	12
LIST OF SYMBOLS	13
Chapter 1 - INTRODUCTION	15
1.1 Background	15
1.2 Objectives of Present Research	19
1.3 Organization	20
Chapter 2 - CONTINUUM MODELING OF SEA ICE BEHAVIOR	23
2.1 Introduction	23
2.2 Uniaxial Model Formulation	27
2.3 Variable Loading History Simulation	36
2.4 Calibration With Uniaxial Experimental Data	40
2.5 Multiaxial Model Formulation and Calibration	73
2.6 Summary	85
Chapter 3 - YIELDING AND FRACTURE MODELING OF SEA ICE BEHAVIOR	88
3.1 Introduction	88
3.2 Prediction Of First Crack Occurrence	89
3.3 Multiaxial Model Formulation	104
3.4 Summary	114

Page

Chapter 4 - APPROXIMATE ANALYTICAL SOLUTION FOR INDENTATION 116
4.1 Introduction 116
4.2 Bound Method versus Strain Path Method 121
4.3 Kinematic Modeling Of Ice Sheet 126
4.4 Ice Pressures For Power-Law Creep 136
4.5 Comparison With Other Studies 148
4.6 Summary 153

Chapter 5 - FINITE ELEMENT ANALYSIS OF PLANE STRESS INDENTATION 156
5.1 Introduction 156
5.2 Material Modeling 157
5.3 Finite Element Formulation 160
5.4 Numerical Simulations 167
5.5 Discussion Of Results 172
5.6 Summary 199

Chapter 6 - CONCLUSIONS AND RECOMMENDATIONS FOR FUTURE RESEARCH 205
6.1 Summary 205
6.2 Recommendations for Future Research 216

REFERENCES 219

Page

APPENDIX A - MATRICES USED IN CONSTITUTIVE MODEL 232

APPENDIX B - ORTHOTROPIC MATERIAL PARAMETERS 234

APPENDIX C - FREDERKING'S TESTS 240

APPENDIX D - UPPER BOUND SOLUTION 244

APPENDIX E - NONLINEAR EQUATION SOLVER 252

APPENDIX F - ANALYTICAL TESTS FOR CODE VERIFICATION 254

LIST OF FIGURES

Figure		Page
2.1	Generalized Maxwell Model.	28
2.2	Damage Parameter as a Function of Strain and Strainrate.	34
2.3	Strength of Columnar Pure and Sea Ice as a Function of Strainrate.	43
2.4	Strength of Columnar Pure and Sea Ice Corrected for the Effects of Brine Volume.	44
2.5	Strength of Columnar Sea Ice at Different Temperatures.	45
2.6	Stress-Strain Curves for Arctic Sea Ice Under Constant Strain Rate Loading (Wang, 1982).	47
2.7	Stress-Strain Plots for Wang's (1982) Model for Different Strainrates.	48
2.8	Stress-Strain Plots Under Constant Strainrate for Proposed Model.	49
2.9	Creep and Recovery of S-2 Ice at -41°C, 0.49 MPa Stress.	51
2.10	Creep and Recovery of S-2 Ice at -30°C, for Three Successive Loadings of 0.49 MPa.	52
2.11	Creep and Recovery of S-2 Ice at -19.8°C, 0.49 MPa Stress.	53
2.12	Creep and Recovery of Snow Ice (Brill and Camp Data, 1961).	55
2.13	Calculated Creep Curves (Wang, 1982).	58
2.14	Calculated Creep Curves Based on the Model.	59
2.15	Strength of Sea Ice as a Function of Stress-Rate.	60
2.16	Strength of Normalized Ice as a Function of Stress-Rate.	61
2.17	Stress-Strain Behavior Under Constant Stress-Rate Loading Conditions.	62

LIST OF FIGURES (CONT'D)

Figure		Page
2.18	Calculated Stress-Strain Curves for Unoriented Columnar Sea Ice Under Constant Stress-Rate Loading (Wang, 1982).	65
2.19	Effective Modulus versus Strainrate.	66
2.20	Ratio of Residual to Peak Stress as a Function of Strainrate.	67
2.21	Stress Relaxation.	69
2.22	Unloading and Reloading at Constant Strainrates, (Dash Lines for No Unloading).	70
2.23	Unload at Constant Stress-Rate of -5.0 Mpa s^{-1}, Reload at Constant Strainrate of 10^{-3} s^{-1}.	71
2.24	Unload at Constant Stress-Rate of -1.0 Mpa s^{-1}, Reload at Constant Strainrate of 10^{-3} s^{-1}, (Dash Line for No Unloading).	72
2.25	Cyclic Stress Load at 1 Hz.	74
2.26	C-Axis Orientation.	79
2.27	Normalized Shear Stress versus Confining Pressure.	83
3.1	Formation of First Cracks During Unaxial Compressive Creep Tests.	91
3.2	Formation of First Cracks Under Constant Stress-Rate Tests.	92
3.3	Stress at Which First Cracks Appear for Pure Ice Under Constant Stress-Rate Tests.	93
3.4	Stress at Which First Cracks Appear for Sea Ice Under Constant Stress-Rate Tests.	94
3.5	Strength of Pure Ice In Uniaxial Compression and Tension at -10°C (Palmer et al., 1982).	97
3.6	Strength of Columnar Ice.	98
3.7	Stress-Strain Plots Under Constant Strainrate for Proposed Model with Fracture.	99

LIST OF FIGURES (CONT'D)

Figure		Page
3.8	Tensile Fracture Strain Under Different Strainrate Loading Conditions.	101
3.9	Formation of First Cracks During Uniaxial Compressive Creep Tests.	103
3.10	Tensile Fracture Strength and Compressive Strength for Crack Nucleation.	106
3.11	Variation of p and k with Strainrates.	108
3.12	Limiting Flow Surface Under Plane Stress Condition at Low Strainrate.	109
3.13	Fracture Surface Under Plane Stress Condition at High Strainrate.	111
3.14	Interaction of the Fracture Surface with the Limiting Flow Surface Under Plane Stress Condition, Normalized by the Peak Compressive Stress.	112
3.15	Biaxial Failure Envelopes for Brittle Materials (Haynes, 1973).	113
4.1	Streamlines for the Superposition of a Point Source with a Uniform Flow (Kinematic Model A).	129
4.2	Streamlines for the Superposition of a Doublet with a Uniform Flow (Kinematic Model B).	132
5.1	Tests for Code Verification.	168
5.2	Finite Element Grid.	173
5.3	Normal Stress Distribution on Interface at Time Step 1 for $\beta_1=1$.	183
5.4	Normal Stress Distribution on Interface at Steady State for $\beta_1=1$.	184
5.5	Normal Stress Distribution on Interface at Steady State for $\beta_1=5$.	186

LIST OF FIGURES (CONT'D)

Figure		Page
5.6	Shear Distribution on Interface for Fixed Condition at Steady State for β_1=1.	187
5.7	Pressure-Area Curve.	189
5.8	Biaxial Stress States for Fixed Condition (β_1=1).	194
5.9	Biaxial Stress States for Free Condition (β_1=1).	195
5.10	Biaxial Stress States at Steady State for Fixed Condition.	196
5.11	Biaxial Stress States at Steady State for Free Condition.	197
5.12	Minimum Principal Strain Contours (Time Step 20).	198

LIST OF TABLES

Table		Page
4.1	Maximum Radial Strainrates on Ice-Structure Interface (sec^{-1}).	147
4.2	Maximum Radial Stresses on Ice-Structure Interface (psi).	147
4.3	Average Global Pressure Using Upper Bound Method with Friction (psi).	149
4.4	Average Global Pressure Based on Integrated Stress Field (psi).	149
4.5	Comparison of Average Global Pressures for Power-Law Creep with N=3 and Average Strainrate of U/2D.	151
5.1	Summary of Cases.	169
5.2	Summary of Results.	174
5.3	Multiplying Factors for Approximate Model (Eq. 5.23).	181

LIST OF SYMBOLS

a	parameter of power law model in reference direction
a_i	six parameters of orthotropic material model
$\underline{B}$	finite element transformation matrix
$\underline{C}$	linear elastic orthotropic compliance matrix
D	diameter of structure
$\underline{D}$	linear elastic orthotropic rigidity matrix
E	Young's modulus for transversely isotropic sea ice
$\underline{G}$	transformation matrix relating $\underline{S}^*$ to σ
$\underline{K}$	linear elastic stiffness matrix of finite element
$\underline{K}_G$	linear elastic global stiffness matrix
n	constant equal to $2N/(N+1)$
N	power law exponent
P	global force acting on structure
$\underline{P}$	applied load vector
$\underline{S}$	deviatoric stress vector
$\underline{S}^*$	pseudo deviatoric stress vector for orthotropic material
t	thickness of ice sheet
t_i	time at instant i
T	temperature
U	approach velocity of ice sheet
$\underline{U}$	nodal displacement vector

LIST OF SYMBOLS (CONT'D)

α	parameter in time integrator
β	constant equal to a_1+a_2
β_i	five ratios of maximum stress along x, z and the 45° axes on the y-z, x-y and z-x planes, respectively, to the stress in the reference y-direction
γ	ratios of stresses or pressures under different conditions
$\underline{\varepsilon}$	total strain vector
$\underline{\varepsilon}_{cr}$	creep strain vector
$\underline{\varepsilon}_I$	inelastic strain vector
ε_e	effective strainrate measure
θ	plane strain to plane stress conversion factor
λ	associative flow rule constant
ν	Poisson's ratio for transversely isotropic sea ice
$\underline{\sigma}$	stress vector
σ_e	effective stress measure
τ	ratio of confining pressure to axial stress
ϕ	scalar potential function
•	rate form is represented by a dot above the symbol

CHAPTER ONE

INTRODUCTION

1.1 BACKGROUND

As much as 30-40 percent of the U.S. undiscovered hydrocarbon recoverable reserves, comparable in magnitude to those of the Persian Gulf, are estimated to lie in the Arctic. The extraction of these resources in an economical and safe manner poses many technical challenges. The cost of building fixed offshore platforms for drilling and production in the Arctic is significantly influenced by ice loads.

Exciting new structural concepts for exploration and production platforms are now under intensive development to meet the severe design problems for fixed offshore platforms in the Arctic: a very short open water season, which necessitates preconstruction and towing to the site; massive global ice forces and extremely high local pressures; and often relatively weak foundation soils. In deeper waters, gravity caisson and conical strutures will probably replace the artificial islands that have been constructed thus far in shallow water. Conical structures are attractive since they induce flexural failures in ice, a material whose flexural strength is significantly lower than its compressive strength.

Both concrete and steel are being considered as the principal construction materials for Arctic structures. Steel structures pose severe problems due to local buckling and brittle fractures. New high strength lightweight concretes with high abrasion and freeze-thaw resistance are being developed to reduce the weight of concrete structures. The major design problem is obtaining suitable resistance to the large local ice loads (for both service and ultimate conditions), which result not only in large bending forces but also in much larger punching shear stresses than considered in current design codes. Existing numerical techniques for predicting shear stresses are both very expensive to use and subject to considerable inaccuracy.

The severe environment created by perennial ice features can lead to global forces and local pressures on structures which are several times greater than those from waves in non-Arctic environments. Typically, two levels of ice loading are considered for design purposes. Global ice loads govern the overall structural geometry and dimensions as well as the foundation design, while local ice pressures are likely to dictate wall thickness and local framing, and may well govern structural cost.

Most of the emphasis in research has been on predicting global forces. Only during recent years, as the focus changed from overall feasibility to preliminary and detailed design, has the importance of local pressures emerged. Recent work, (Watt, 1983), has shown that peak local pressures may be as high as three times the average pressure assumed for global load. It is widely recognized that significant uncertainties exist in the ice load models in use today and that some design loads may be overestimated by an order of magnitude. Research is necessary to quantify the uncertainties in ice loads and to develop improved load prediction models for the safe and economical design of structures.

Uncertainties in existing ice load models arise primarily from five sources:

- Incomplete modeling of the mechanical behavior of ice, including temperature and fracture effects.
- Empiricism in existing theoretical models resulting from the use of approximate analysis methods.
- Inadequate modeling of the contact forces at the ice-structure interface.
- Neglecting the effect of scale/size on material strength.
- Not accounting for the finiteness of environmental and other forces driving the ice features.

In order to quantify these uncertainties and to better predict global and local ice loads, numerical models are necessary for computer simulation of ice-structure interaction processes. In contrast to analytical methods, such models can realistically simulate the interaction accounting for spatial-temporal variability in the mechanical behavior of ice and for multiple modes of failure in ice.

The complexity of sea ice behavior is due mainly to:

- Strong dependence on rate of loading, which is spatially and temporally variable in ice features.
- Simultaneous occurrence of ductile, strain-softening, and brittle modes of deformation.
- Pressure sensitivity leading to different strengths in compression and tension (at moderate-to-high rates of loading) and to melting point depression.
- Material anisotropy leading to strength variation by a factor of three.
- Strong dependence on temperature, varying in first year ice from melting point at the water interface to perhaps -50°F at the air interface.
- Strong dependence on internal structure of ice (grain size, fabric, brine volume, salinity, porosity), which is spatially varying particularly in multi-year ice features.

A key aspect in the development of constitutive models is the need for accurate and consistent experimental data on ice, especially to characterize its behavior relating to tensile loading, cyclic loading, multiaxial loading, nucleation and interaction of cracks, material anisotropy, thermal and structural gradients, and fracture toughness. Currently available data is in many cases sufficient to postulate approximate constitutive models. Numerical simulations can help to establish the importance of more extensive experimentation in quantifying ice-structure interaction processes.

Finite element methods of analysis for simulating ice-structure interaction processes are affected by the following research concerns:

- Rate dependent material behavior with negligible elastic deformation.
- Initiation and propagation of cracks due to fracture.
- Simultaneous occurrence of rate dependent and fracture behavior.
- Adfreeze bond and friction at ice-structure interface.
- Time-varying contact between ice and structure and between fractured ice features.
- Strain-softening of ice.

1.2 OBJECTIVES OF PRESENT RESEARCH

The overall objectives of this research are to develop a constitutive model for sea ice and to use the model for studying ice indentation problems. The specific contributions include:

(1) Development of a rate sensitive damage model for describing the macroscale continuum behavior of sea ice.

(2) Development of a hybrid model to characterize both the continuum and fracture behavior of sea ice.

(3) Development of a finite element model for numerical simulation of sea ice indentation.

(4) Development of simplified mathematical models for predicting global ice forces and pressure-area curves during sea ice indentation.

1.3 ORGANIZATION

The rate sensitive damage model for macroscale continuum behavior of sea ice is described in Chapter 2. This model, based on a nonlinear generalization of the Maxwell differential model, is characterized by its ability to (a) decompose the various recoverable and irrecoverable components of strain, (b) represent continuously damaging or strain-softening material behavior in the ductile to brittle transition region, (c) capture the rate-dependent behavior of sea ice with rate-dependent model parameters, and (d) describe materially anisotropic mechanical behavior. Further, the model shows strong dependency of the creep and constant strainrate behavior. Calibration of the model is achieved with several independent sets of data, particularly those for first year sea ice.

Chapter 3 presents a rate-sensitive model in stress-strain domain for describing the macroscale fracture behavior of sea ice. This model, unified with the continuum model of Chapter 2, is characterized by its ability to (a) predict first crack occurrence or nucleation with a rate dependent limiting tensile strain criterion, (b) distinguish the mechanisms of multiaxial flow by creep and yielding which leads to ultimate failure by macrocracking or fracture, and (c) represent the yield under multiaxial states of stress with a Drucker-Prager failure surface. Calibration of the model is achieved with the limited existing experimental data base.

Chapter 4 describes two approximate methods of analysis for predicting global and local pressures during sea ice indentation in the creeping mode of deformation. The two methods are the upper bound and strain path methods. Theoretically postulated velocity fields required in the analysis are calibrated with field measurements. The results are compared with previously published indentation formulas.

In Chapter 5, a finite element method of analysis is developed and applied to study sea ice indentation in the creeping mode of deformation. The numerical algorithm is based on a pressure-insensitive orthotropic elastic-power law creep model for sea ice. Numerical simulations are performed under plane stress conditions to predict the influence of (i) interface adfreeze and friction, (ii) material anisotropy,

(iii) variability in parameters of the material model, (iv) rubble pile or grounded ice foot, and (v) ice sheet velocity on global forces and local pressures generated on a rigid cylindrical indenter. The results are compared with those from the approximate method of analysis discussed in Chapter 4. Interface pressure distributions are obtained in addition to contours of stress and strain. Pressure-area curves are constructed from the results and discussed.

Chapter 6 summarizes the conclusions of this study and provides recommendations for future research.

CHAPTER TWO

CONTINUUM MODELING OF SEA ICE BEHAVIOR

2.1 INTRODUCTION

Ice in general, and columnar sea ice in particular, is a very complex material which exhibits a wide range of behaviors often at the same time. As a consequence of its occurrence at thermorheologically high temperatures, the macroscale mechanical behavior of ice is strongly influenced by temperature and rate of loading, in addition to elasticity, plasticity, damage and fracture. In many applications ice behaves predominantly as a continuum undergoing deformation and a constitutive model which captures that behavior is necessary to simulate the deformation process.

Shapiro (1978) has presented a four element nonlinear viscoelastic model for sea ice which can be applied under general loading conditions. Under constant strainrate tests, this model predicts an approximately linear increase of strength with the logarithm of strainrate which appears to differ from available test data. Furthermore, this model cannot simulate the post-peak decrease of stress due to material damage.

Sinha (1978, 1979, 1983b) has proposed a simple thermorheological model to describe the uniaxial stress-strain-strainrate-temperature relationship for columnar-grained ice. The model, consisting of eight parameters, accounts for the instantaneous elastic, delayed elastic, and secondary creep components of strain. According to the model, the delayed elastic strain under creep loading conditions is directly proportional to the applied stress and grain size while its value reaches a maximum asymptotically with time. Calibration has been achieved with the extensive creep and constant stressrate tests conducted on columnar-grained ice by him and the creep data of Brill and Camp (1961).

Michel (1981) has proposed a similar model for ice based on dislocation theory. The model, consisting of a network of linear springs and nonlinear dashpots with nine parameters, has been applied under constant stress (creep) and strainrate conditions. Unlike Sinha's model, this formulation shows a peak followed by a stage of permanent creep at a lower stress. Calibration with limited data from Brill and Camp (1961) and his own tests suggests the need for adjustment of model parameters for each test case.

Wang (1982) has proposed a four parameter semi-empirical uniaxial model for sea ice in compression. Under constant strainrate conditions, the model displays a peak followed by a stage of permanent creep at a lower stress. The model has not been extended to allow decomposition of the various strain components. Furthermore, numerical problems associated with the mathematical formulation can arise under certain conditions during constant stressrate and creep loading. Calibration of the model has been performed with his constant strainrate and stressrate tests and with the creep data contained in Mellor (1980).

Morland and Spring (1981, 1982, 1983) have investigated viscoelastic fluid and solid relations of differential type as well as single integral representations for the nonlinear viscoelastic deformation of ice. In the fluid relation the constant stress and constant strainrate responses are neither completely independent nor completely dependent, so reflecting some common and some distinct properties. In the solid relation these two responses are completely independent and, in fact, are insufficient to determine the model without further reductions. Mellor (1980) conjectured that the two types of response should be dependent, which is the familiar linear result. While the differential fluid relation is closer to this conjecture, it cannot model anisotropy and strain jumps. In both types it is necessary to incorporate dependence of one or more response coefficients on both stress and strainrate or strain respectively, and covering adequate stress-strainrate or stress-strain domains by practical test programs is non-trivial. On the other hand, the single integral representation is sensitive to kernel detail, which in turn is dependent on strainrate histroy. Calibration of the formulations with experimental data has been very limited.

More recently, Karr (1984, 1985a, 1985b) has been investigating the use of continuous damage models for describing the uniaxial behavior of ice. His four parameter model for sea ice displays a peak followed by a stage of permanent creep at a lower stress and has been derived for constant strainrate loading conditions. For creep loading, an empirical approach is used in conjunction with the damage mechanics based stress-strain law for constant strainrate loading. The constant stressrate case has not been studied, and the methodology for strain decomposition under general loading conditions is unclear.

This chapter presents a rate-sensitive damage model for describing the macroscale continuum behavior of sea ice. The model, based on a nonlinear generalization of the Maxwell differential model, is characterized by its ability to (a) decompose the various recoverable and irrecoverable components of strain, (b) represent continuously damaging or strain-softening material behavior in the ductile to brittle transition region, (c) capture the rate-dependent behavior of sea ice with rate-independent model parameters, and (d) describe materially anisotropic mechanical behavior. Further, the model shows strong dependency of the creep and constant strainrate behavior. Calibration of the model is achieved with several independent sets of data, particularly those for first-year sea ice.

2.2 UNIAXIAL MODEL FORMULATION

The nonlinear generalization of the two element Maxwell fluid model consists of an elastic spring in series with a viscous dashpot (Fig. 2.1). The rate-sensitive spring represents recoverable strains and accounts for both instantaneous elasticity and delayed elasticity or primary creep. The viscous dashpot represents irrecoverable strains associated with nonlinear viscosity or secondary creep. Both the rate-sensitive spring and the nonlinear viscous dashpot are affected by material damage and as a result account for strain-softening or tertiary creep. The mathematical formulation of the two elements is discussed in what follows.

Rate-Sensitive Elastic Spring -- Most conventional materials are used at thermorheologically low temperatures where their elastic properties are relatively insensitive to rate of loading. The modulus of elasticity or Young's modulus for such materials is obtained from tests conducted at commonly encountered rates of loading and taken to be a constant. However, in certain high loading rate applications, e.g., blast and impact, it is known that the modulus of elasticity increases with rate. As a consequence of its occurrence at thermorheologically high temperatures, the

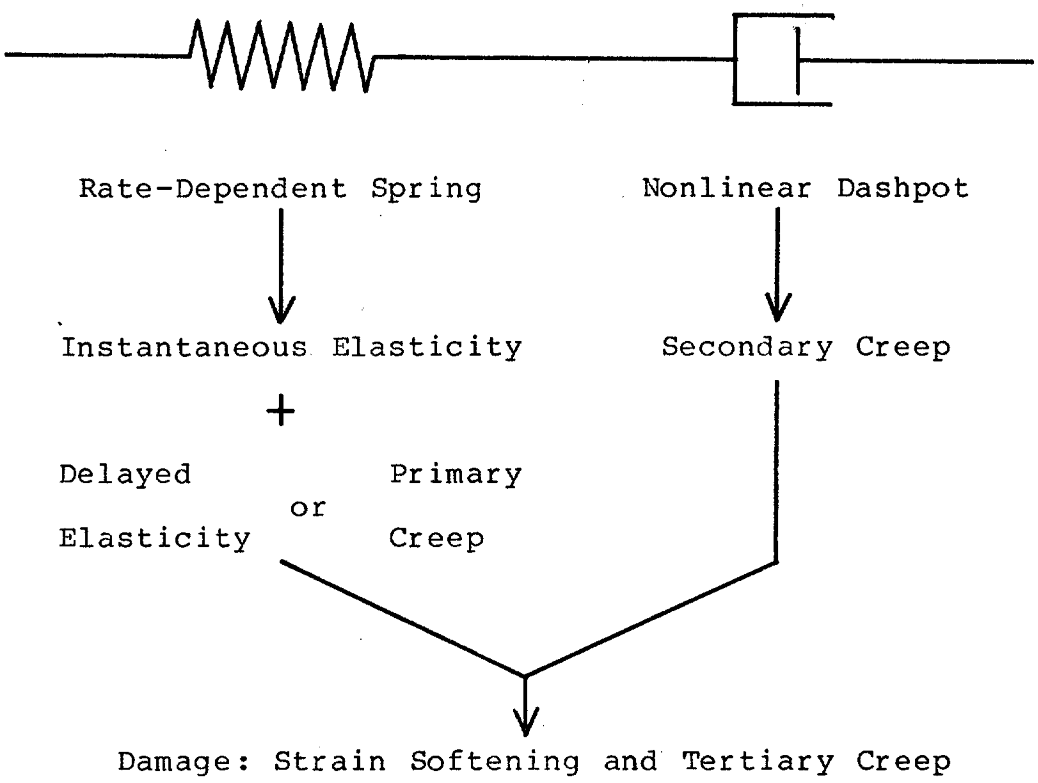
Rate-Dependent Spring
Nonlinear Dashpot
Instantaneous Elasticity
Secondary Creep
+
Delayed Elasticity
or
Primary Creep
Damage: Strain Softening and Tertiary Creep

Figure 2.1 Generalized Maxwell Model.

elastic modulus of ice is sensitive to even "slight" variations in rate of loading (Mellor, 1983) and cannot be taken as a constant. If the Young's modulus for ice, E, is defined to be the modulus value at very high rates of loading, then the variation of effective elastic modulus, E_{eff}, with rate may be expressed as:

$$E_{eff} = E\,[1 - r \exp(-A/E\,\dot{\varepsilon}^{1/N})] \qquad (2.1)$$

where $\dot{\varepsilon}$ is the strainrate, r and A are constants, and N is the power law index for ice. Equation 2.1 shows that the effective modulus tends to the Young's modulus as the strainrate approaches infinity. As the strainrate tends to zero, the effective modulus tends to (1-r)E, and for r equal to one, the effective modulus tends to zero. If r is zero, the effective modulus is rate-insensitive and equal to the Young's modulus. A value of r less than one is necessary to model stress relaxation, as explained later in this chapter.

The rate-sensitive elastic spring represents recoverable strains contributed both by instantaneous elasticity and by delayed elasticity. By defining the total elastic strain to be the sum of the strains due to these two components it is possible to model the rate-sensitive spring as the series combination of two springs, one with modulus equal to E, i.e., the Young's modulus, and the other with a modulus equal to E_d, the modulus of delayed elasticity. It then follows that:

$$1/E_{eff} = 1/E + 1/E_d \tag{2.2}$$

with:

$$E_d = E\ [1/r\ \exp(A/E\ \dot{\varepsilon}^{1/N}) - 1] \tag{2.3}$$

Equation 2.3 shows that the modulus of delayed elasticity tends to infinity at infinite strainrate and to [(1-r)/r]E at zero strainrate. In the latter case, the modulus tends to zero if r is one and to infinity if r is zero. Use of Eq. 2.2 shows that when the modulus of delayed elasticity is infinity, the effective modulus equals the Young's modulus. When the modulus of delayed elasticity is very small with respect to the Young's modulus, the effective modulus equals the modulus of delayed elasticity. This occurs at low strainrates. Research on the mechanical behavior of materials at thermorheologically high temperatures (Grant, 1971) has shown that delayed elasticity associated with grain boundary sliding does lead to the behavior predicted by this model.

Nonlinear Viscous Dashpot -- The secondary creep strain, ε_{sc}, in many materials including ice is assumed to follow the well known Glen's power law (Glen, 1955). The mathematical formulation of this law is as follows:

$$\sigma = (A/M)\ \dot{\varepsilon}_{sc}{}^{1/N} \tag{2.4}$$

where A and N are the constants in Eq. 2.1, and M is a third constant. Normally (A/M) is taken to be a single constant. However, since A is used to describe the primary creep strains, an additional degree of freedom in the form of the constant M is necessary to model secondary creep strains. The nonlinearity is associated with the dashpot constant $\sigma/\dot{\varepsilon}_{sc}$ which is a function of the secondary creep strainrate.

Continuous Damage Model -- In the transition from pure ductile to pure brittle behavior under compressive loading ice behaves as a continuum undergoing damage. Under tensile loading the transition region is much smaller and a continuum description of damage is of limited value. Damage in ice leads to tertiary creep under constant stress loading and to strain-softening under constant strainrate loading. Damage is almost nonexistant at very small strain and strainrate but increases as both strain and strainrate increase. Further, unloading a damaged material generally shows a reduction in the effective modulus of elasticity. Thus the phenomenon affects both the rate-sensitive spring and the nonlinear viscous dashpot. The development here is based on the hypothesis that this effect influences the constant A describing the creep resistance of ice, which appears in both the elements of the generalized Maxwell model. Defining D as a one-dimensional damage parameter and A_D as the damaged value of the constant A, it is possible to state that:

$$A_D = (1-D)A \tag{2.5}$$

where D=0 in the case of no damage, and the A's in Eqs. 2.1, 2.3 and 2.4 are replaced with A_D. In general, D varies between zero and one. For the case of total damage, i.e., D=1, the stress reduces to zero. This formulation is unlike some others which model damage with "negative" springs that have little physical appeal and can cause numerical problems, for example, in the form of stresses with wrong sign. The following mathematical form describes the dependence of the damage parameter on strain and strainrate, and satisfies the physical constraints identified above.

$$D=1-[\exp(-c_1 \varepsilon\dot{\varepsilon})+\exp(-c_2\dot{\varepsilon})\{1-\exp(-c_1 \varepsilon\dot{\varepsilon})\}] \qquad (2.6)$$

where c_1 and c_2 are constants. This equation shows that as strainrate approaches infinity D tends to one, i.e., the material is completely damaged. Further, as strain approaches infinity D tends to $[1 - \exp(-c_2\dot{\varepsilon})]$, i.e., there is a limiting value of damage at any given strainrate. The repeated use of c_1 in Eq. 2.6 is to ensure that D does not have a negative value.

Damage in a material is directly related to microcracking activity during deformation. Gold (1960) cites a paper by E. Brown (1926) who noted the presence of audible "crackling" of ice samples subject to compressive loads. Brown associated the audible crackling with the development of cracks in ice. He also noted that the crackling of the ice was related to the level of the stress applied and the temperature at which the test was conducted. In his own early research, Gold (1960) used a piezoelectric crystal frozen to the ice sample to acoustically monitor the fractures which took place in the ice. In his seminal paper more than a decade later, Gold (1972) reported the results of an extensive study on the process of failure of columnar-grained ice. He developed statistics on cracking activity based on visual observations during creep tests. His distribution of cracking activity followed an expression similar to Eq. 2.6 with strain as the variable. Stress and temperature were identified as additional variables that could affect cracking activity, but they were found to have limited effect on his test results. More recently, Zaretsky et al. (1979) and St. Lawrence and Cole (1982) have studied in detail the acoustic emissions from columnar-grained and fine-grained polycrystalline ice, respectively. Observations from the above test programs lend additional credibility to the general functional form of the proposed damage model.

The formulation of the damage parameter in Eq. 2.6 is appropriate under a given monotonic loading condition. For a variable loading history the evolution of the damage parameter is assumed to follow Miner's rule, i.e., the incremental damage accumulation depends only on the current state of damage and can be defined in terms of an equivalent strain at the instantaneous strainrate. This evolution of the damage parameter D with strain and strainrate is shown in Fig. 2.2.

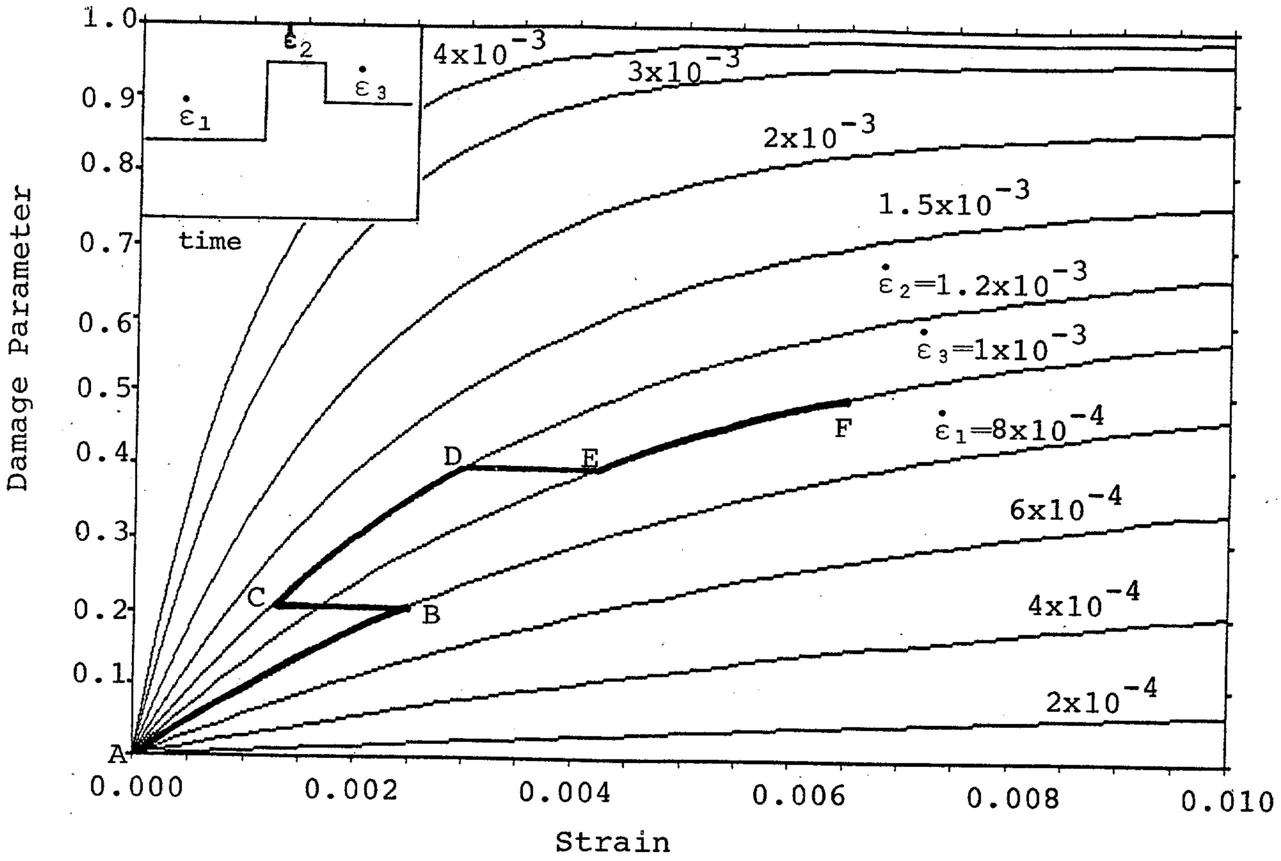

Figure 2.2 Damage Parameter as a Function of Strain and Strainrate.

For very low strainrates the accumulation of material damage is small and not of significance in modeling the behavior of sea ice.

Temperature Effects -- At rates of loading where no material damage is present in sea ice, the effect of temperature on the stress versus secondary creep strain relationship is characterized by an Arrhenius activation energy law. Mellor (1983) states that for temperatures greater than -10°C the law is not valid and that the complete empirical relation derived from experiments should be used to model the temperature dependence in such cases. Sinha (1978) has concluded that the variation of the delayed elastic or primary creep strain with temperature also follows an Arrhenius law. He found the activation energy for both the viscous flow and the delayed elastic deformation to be equal. Noting that the Young's modulus is relatively independent of temperature, Sinha found that creep strains obtained at various temperatures can be combined to give a master curve at some standard temperature.

The parameter A, which appears in Eqs. 2.1, 2.3 and 2.4, describes the creep strains in ice and is taken to follow the Arrhenius activation energy law to model temperature effects below -10°C, i.e.,

$$A = A_o \exp(Q/NRT) \qquad (2.7)$$

where T is the temperature in degrees Kelvin (0°C equals

273°K), A_o is a temperature independent constant, Q is the activation energy, and R is the universal gas constant. As the temperature reduces, the parameter A increases in value. In consequence, the effective elastic modulus tends to the Young's modulus and the nonlinear dashpot becomes highly viscous. Then ice displays a purely linear elastic material behavior with no rate or temperature sensitivity. At the same time, the model predicts that no continuum damage can occur in compression. This is realistic since at such temperatures ice behaves as a brittle material for which the transition from an undamaged state to a state with extensive macrocracking is almost instantaneous.

2.3. VARIABLE LOADING HISTORY SIMULATION

Governing Equations -- The rate-sensitive damage model for the continuum behavior of sea ice assumes that the total strainrate is the sum of the effective elastic strainrate and the nonlinear viscous strainrate, i.e.,

$$\dot{\varepsilon} = \dot{\sigma}/E_{eff} + \dot{\varepsilon}_{sc} \tag{2.8}$$

where $\dot{\varepsilon}_{sc}$ can be expressed as $\mu\sigma$ with

$$\mu = (M/A_D)^N \sigma^{N-1} \tag{2.9}$$

Alternatively, Eq. 2.8 can be expressed as:

$$\dot{\sigma} = E_{eff} (\dot{\varepsilon} - \dot{\varepsilon}_{sc}) \tag{2.10}$$

Using Eq. 2.2, Eqs. 2.8 and 2.10 can be rewritten in terms of

Young's modulus and total creep strainrate, $\dot{\varepsilon}_{cr}$, in the form given below.

$$\dot{\varepsilon} = \dot{\sigma}/E + \dot{\varepsilon}_{cr} \tag{2.11}$$

and

$$\dot{\sigma} = E(\dot{\varepsilon} - \dot{\varepsilon}_{cr}) \tag{2.12}$$

where

$$\dot{\varepsilon}_{cr} = \dot{\sigma}/E_d + \mu\sigma \tag{2.13}$$

For an ideal creep test, the instantaneous stressrate at the time of stress application is a Dirac delta function. It follows from Eq. 2.10 that the instantaneous total strainrate is a delta function and from Eq. 2.1 that the instantaneous effective modulus is equal to the Young's modulus. Further, for all time after application of the stress, the stressrate is zero. According to Eq. 2.10 this is possible only if the total strainrate equals the secondary creep strainrate for all time immediately after load application. Thus according to the model, the ideal creep curve should exhibit no primary creep strain. Tertiary creep strains may occur for large stresses as the total strain increases.

The stress-strain-strainrate behavior for loading conditions other than ideal creep cannot be obtained analytically. A numerical solution algorithm, applicable to constant strainrate, constant stressrate or variable loading history, is presented in what follows.

Solution Algorithm -- An iterative solution algorithm is developed to solve the nonlinear governing equation given in Eq. 2.12. At first the governing equation is integrated in time between t_i and t_{i+1} to yield:

$$\Delta\sigma = E\ (\Delta\varepsilon - \Delta\varepsilon_{cr}) \tag{2.14}$$

where Δ signifies the increment in the variables over the time increment $t_{i+1}-t_i$. The incremental creep strain which appears in this equation is obtained from Eq. 2.13 with the α-method of numerical time integration, i.e.,

$$\Delta\varepsilon_{cr} = \Delta\sigma/E_d + \Delta t\ \mu_\alpha\ \sigma_\alpha \tag{2.15}$$

where σ_α is a weighted average of the stress over the specified time interval, i.e.,

$$\sigma_\alpha = (1-\alpha)\ \sigma_i + \alpha\ \sigma_{i+1} \tag{2.16}$$

and μ_α is derived from Eq. 2.9 using Eq. 2.16. A value of α greater than or equal to 0.5 results in an unconditionally stable, implicit algorithm. The well-known trapezoidal rule and backward Euler method are obtained with α=0.5 and α=1, respectively. The total strain required in the evaluation of A_D in Eq. 2.9 is also estimated with the α-method. However, the total strainrate required in the computation of E_d and A_D, i.e., $\Delta\varepsilon/\Delta t$, is assumed to be a constant over the specified time interval and no weighting is necessary. This assumption is reasonable for small values of Δt.

For accelerating solution convergence in problems of interest dominated by creep strains, a numerical algorithm which combines a Newton-Raphson or tangent type nonlinear equation solver with the α-method is developed. The resulting equations are listed below:

$$[1 + E \frac{\partial \Delta \varepsilon_{cr}}{\partial \sigma_{i+1}}]^k \sigma_{i+1}{}^{k+1} = \sigma_i + E\ (\Delta\varepsilon - \Delta\varepsilon_{cr}{}^k) + E\ [\frac{\partial \Delta \varepsilon_{cr}}{\partial \sigma_{i+1}}]^k \sigma_{i+1}{}^k \qquad (2.17)$$

where $\Delta\varepsilon_{cr}{}^k$ is obtained by applying Eq. 2.15 after obtaining the stress quantities at iteration k, and similarly:

$$[\frac{\partial \Delta \varepsilon_{cr}}{\partial \sigma_{i+1}}]^k = 1/E_d + \Delta t\ \alpha\ \mu_\alpha{}^k\ N \qquad (2.18)$$

For a constant strainrate or strain controlled test, $\Delta\varepsilon$ and σ_i are known. Iteration using Eqs. 2.17 and 2.18 is necessary to obtain σ_{i+1} and $\Delta\varepsilon_{cr}$. In the process of computing the incremental creep strains, the primary, secondary and tertiary creep components of strain can be identified. For a constant stressrate or stress controlled test, $\Delta\sigma$ and ε_i are known. First, Eq. 2.14 is applied to estimate $\Delta\varepsilon$ assuming $\Delta\varepsilon_{cr}$ is zero. Then iteration with Eqs. 2.17 and 2.18 yields $\Delta\varepsilon_{cr}$ and in general an incorrect value of $\Delta\sigma$. Equation 2.14 is again applied with the correct value of $\Delta\sigma$ and the estimated $\Delta\varepsilon_{cr}$ to update $\Delta\varepsilon$. Iteration is then performed with Eqs. 2.17 and 2.18. This procedure is repeated until the solution converges, i.e., the stress increment predicted by Eq. 2.17 equals the specified stress increment. Convergence of the iterations in Eq. 2.17 is defined to occur when the absolute value of the relative change in stress between iterations k and k+1 is less than 0.01. Iteration is also stopped if the actual stress is zero at k and its absolute value is less than 0.01 at k+1. Application of this iterative scheme with $\alpha=1$ shows that convergence is typically obtained in 4 iterations.

2.4. CALIBRATION WITH UNIAXIAL EXPERIMENTAL DATA

The uniaxial model is calibrated with several independent sets of experimental data obtained from constant strainrate, creep and constant stressrate tests. In addition, predictions of the model with respect to (a) ratio of residual stress to peak stress versus strainrate, (b) stress relaxation, and (c) unloading and reloading are also explored. This calibration is based on the following values for the eight model parameters (the universal gas constant, $R=8.314\ \mathrm{J\ mol^{-1}\ K^{-1}}$):

$E = 9.5$ GPa
$r = 0.98$
$A_o = 0.00652$ MPa $s^{1/N}$
$N = 3$
$M = 1411.2$
$Q = 65{,}000$ J mol^{-1}
$c_1 = 2.28 \times 10^5$ s
$c_2 = 1028$ s

For the particular ice type, one of the data sets requires that $E=8.5$ GPa and $r=0.51$ for best fit.

Experimental data on sea ice is limited in comparison to that on pure ice. One way to enlarge the data base is to recognize that sea ice differs from pure ice only in the respect that it contains brine. The salinity of sea ice, S, is typically 3-10 ppt (parts per thousand). The brine volume ν is related to the temperature (°C) and the gross salinity through a general relationship derived by Frankenstein and Garner (1967):

$$\nu = 0.001\ S\ (0.53 - 49.2/T) \tag{2.19}$$

This equation breaks down for temperatures below -22.9°C and also if a significant amount of pore volume is occupied by air bubbles/gas. Brine pockets allow the ice to deform more easily and reduce the strength of the ice. Geometrical considerations (Weeks and Assur, 1967), similar to those in soil mechanics, show that for horizontal loading of ice containing vertically arranged cylindrical brine pockets the net section stress σ' is:

$$\sigma' = \sigma/[1-(\nu/\nu_o)^{1/2}] \tag{2.20}$$

where σ is the applied gross stress. The quantity ν_o corresponds physically to the brine volume at which sea ice loses all strength. A value of ν_o equal to 0.16 gives an optimum correction for a range of experimental observations (Sanderson, 1984). Equations 2.19 and 2.20 as well as the Arrhenius law are used to normalize sea ice stress data when necessary during calibration.

Constant Strainrate Tests -- The maximum stress (for convenience termed "strength" here) observed from constant strainrate tests on pure columnar (S-2) ice and columnar sea ice is plotted versus strainrate in Fig. 2.3. The data is widely scattered and ice strength may vary by an order of magnitude at any given strainrate. Normalizing the experimental data for temperature and salinity effects reduces the scatter by more than a factor of two. The reference temperature and brine volume are taken as -10°C and 0.0, respectively. Figure 2.4 contains this normalized data. The solid line in the figure represents the prediction of the rate-sensitive damage model proposed here. It is obvious that the model captures the overall trend of the data very well. For strainrates greater than 10^{-2} s^{-1} the continuum model of damage is invalid and a horizontal line representing fracture is drawn at a stress of 5 MPa. The dashed line in the figure is the familiar power-law model for secondary creep in ice which fails to model material damage resulting in strain-softening for strainrates between 10^{-4} s^{-1} and 10^{-2} s^{-1}.

Figure 2.5 shows the effects of temperature on the strength versus strainrate behavior. The maximum strength increases with decreasing temperature as expected and it occurs at lower strainrates. A variation in temperature from -10°C to -20°C appears to increase the normalized strength from about 10.0 MPa to 14.2 MPa, which is approximately 42%.

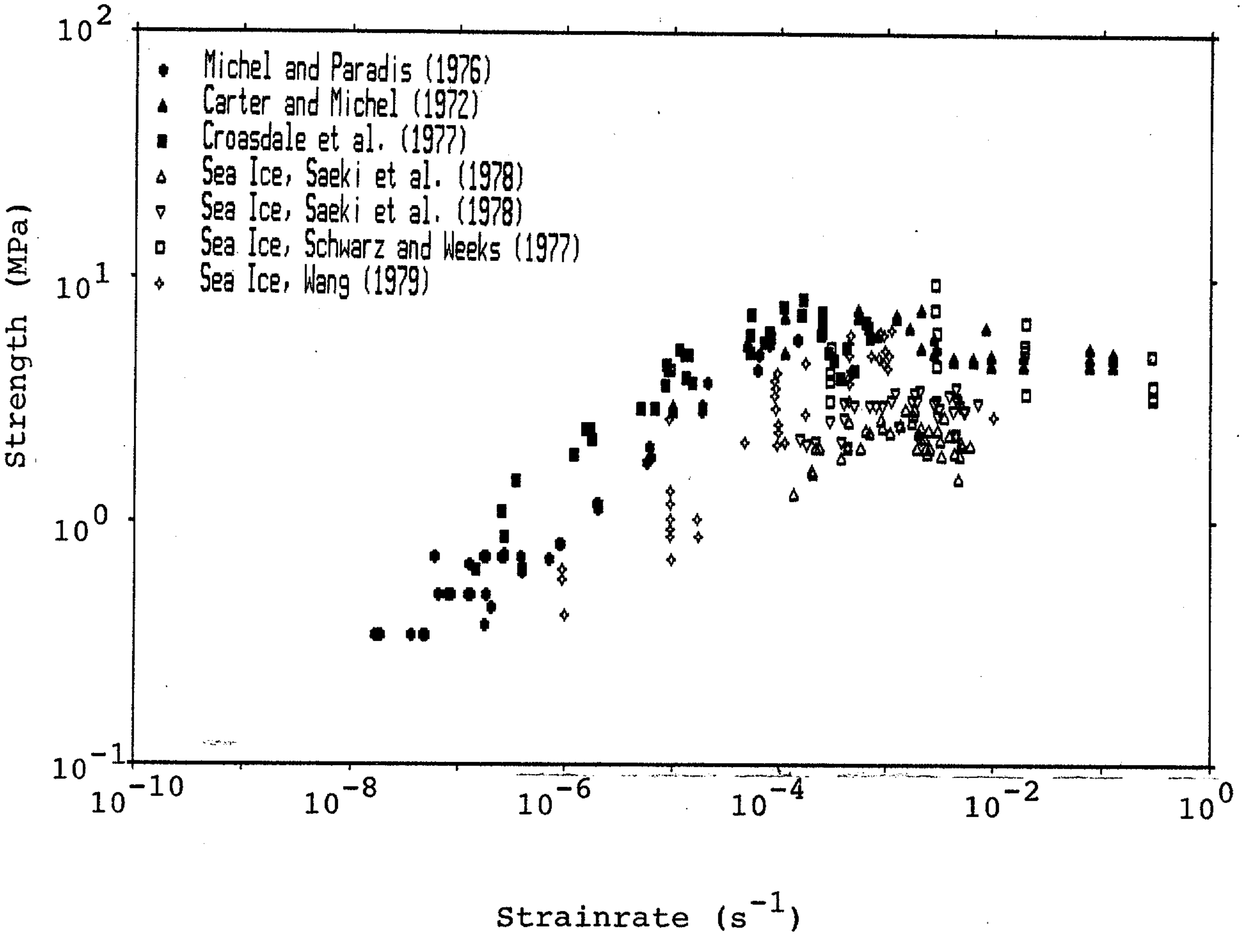

Figure 2.3 Strength of Columnar Pure and Sea Ice as a Function of Strainrate.

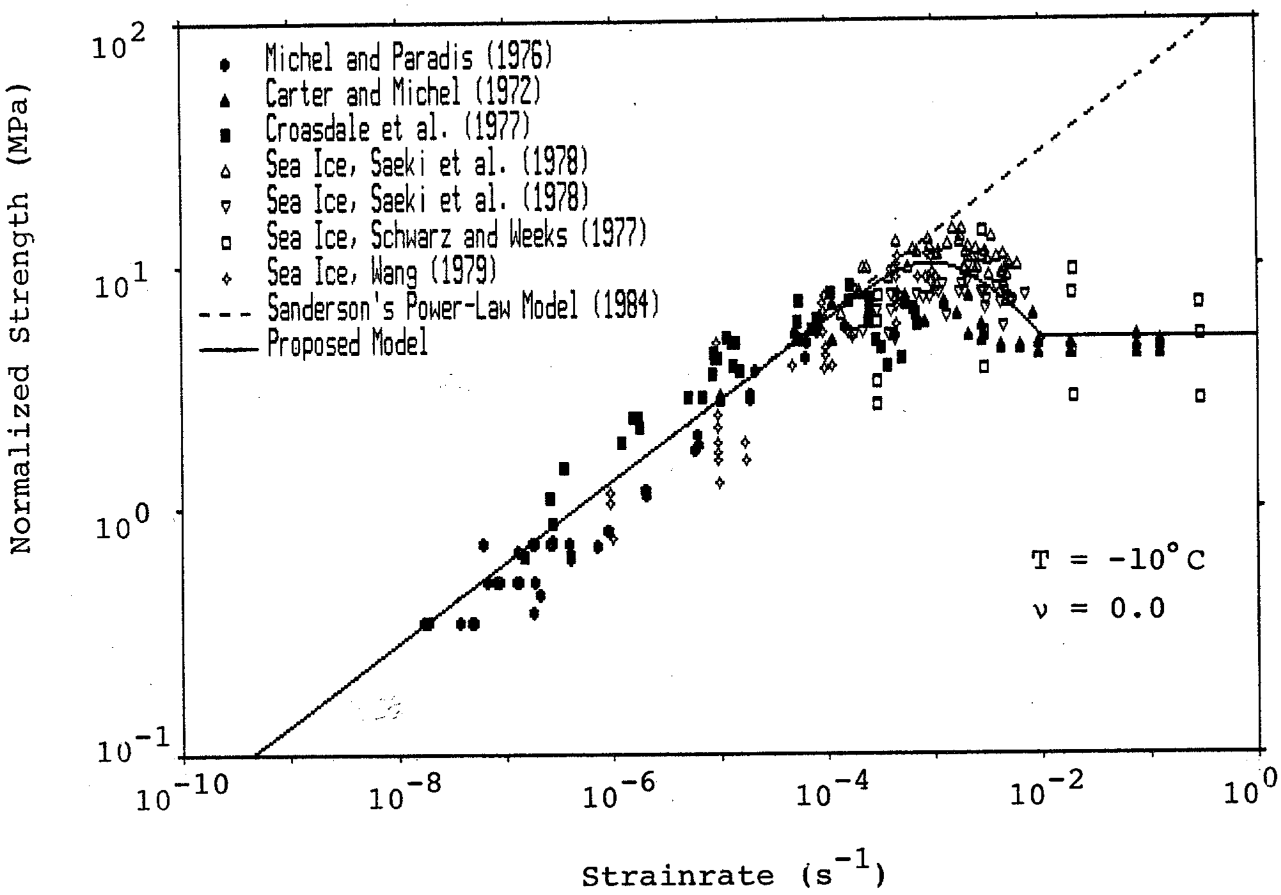

Figure 2.4 Strength of Columnar Pure and Sea Ice Corrected for the Effects of Brine Volume.

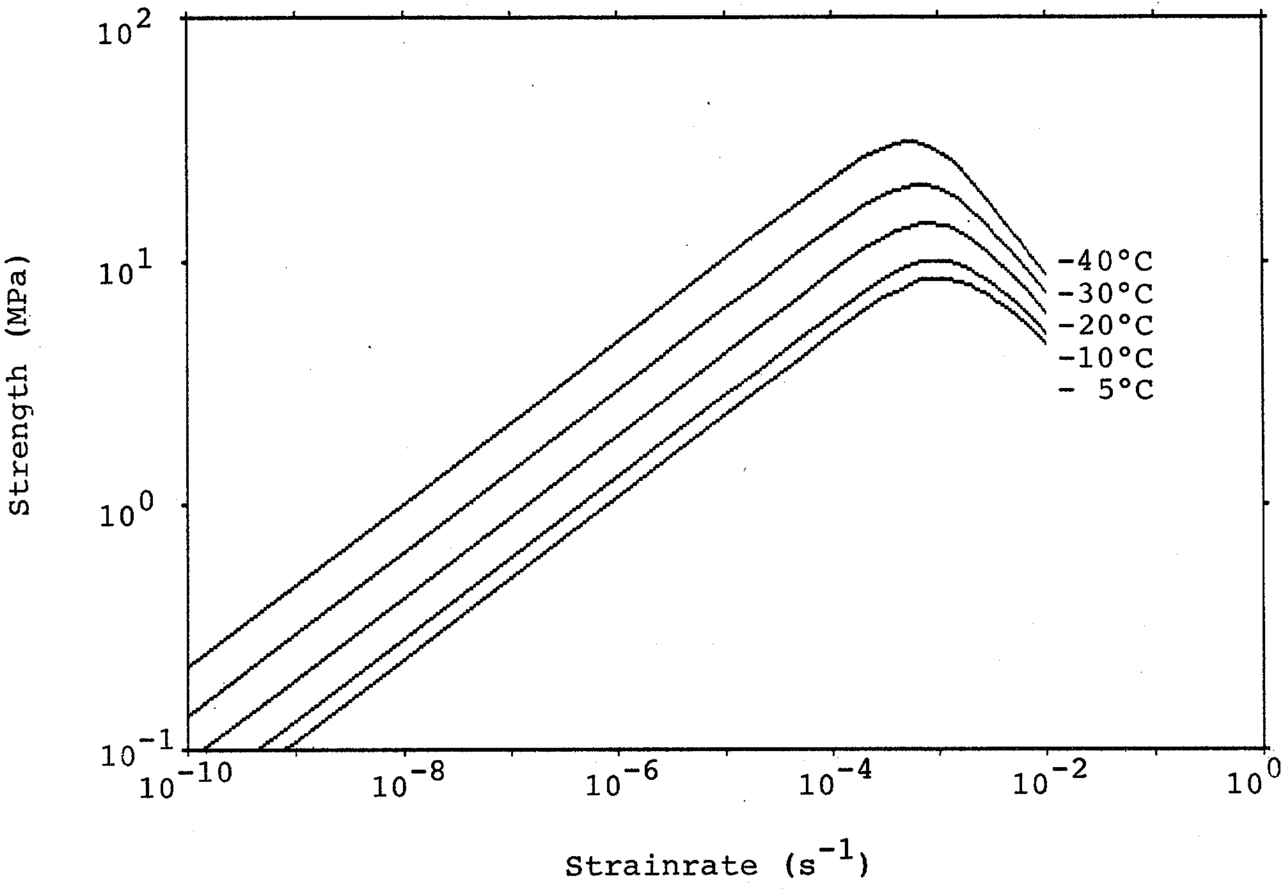

Figure 2.5 Strength of Columnar Sea Ice at Different Temperatures.

This is consistent with the experimental data of Schwarz and Weeks (1977) for sea ice at -10°C and -20°C. At lower temperature, where ice behavior is significantly brittle, it is possible that fracture by macrocracking may limit the strength even at strainrates below 10^{-2} s^{-1} and the peak in the strength-strainrate curve may be eliminated. Experimental data is currently inadequate to fully characterize this behavior.

Wang (1982) has conducted constant strainrate tests on columnar sea ice in the nominal strainrate range 10^{-6} s^{-1} to 10^{-3} s^{-1}. Examples of stress-strain curves observed by him are contained in Fig. 2.6, while those generated by his semi-empirical model are shown in Fig. 2.7. Figure 2.8 plots the predictions of the model proposed here up to a strainrate of 5×10^{-3} s^{-1}. Comparison of the three figures shows that the proposed model is able to capture the characteristics displayed by the experimental data. In fact, the model proposed here better fits the mean strength data contained in Wang (1982). Further, the model correctly predicts the observed lowering of residual stress at higher strainrates as a result of strain-softening.

Creep Tests -- Experimental limitations preclude the possibility of conducting an ideal creep test. In most cases a finite time equivalent to a few seconds is necessary to develop the nominal creep stress. This finite rise time

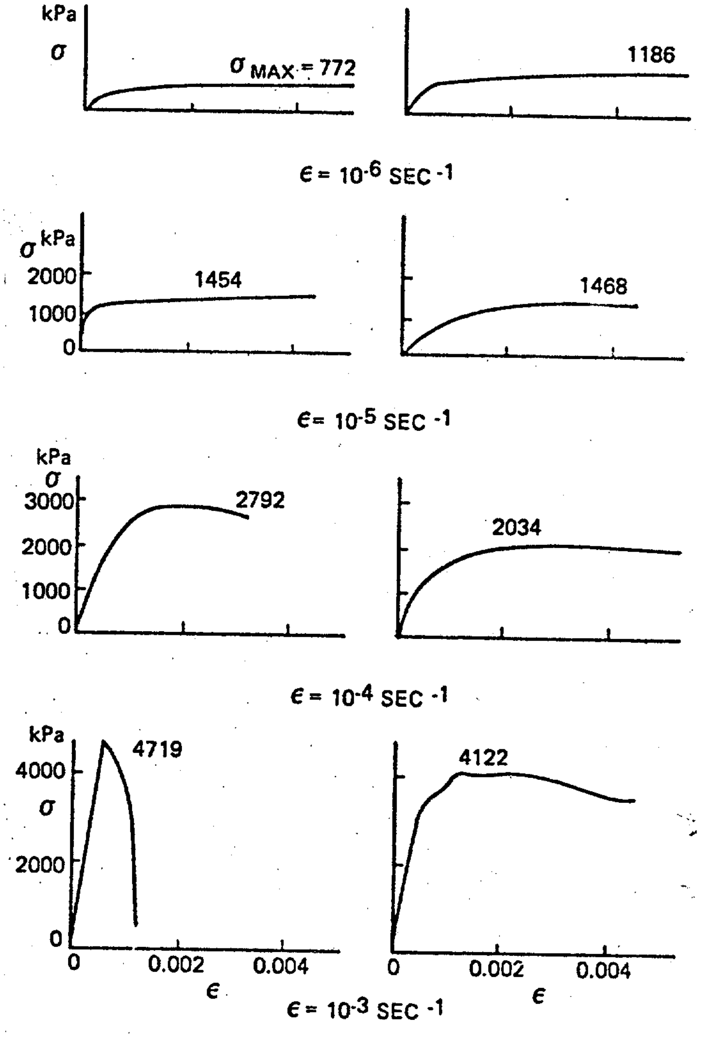

Figure 2.6 Stress-Strain Curves for Artic Sea Ice Under Constant Strain Rate Loading. (Wang, 1982)

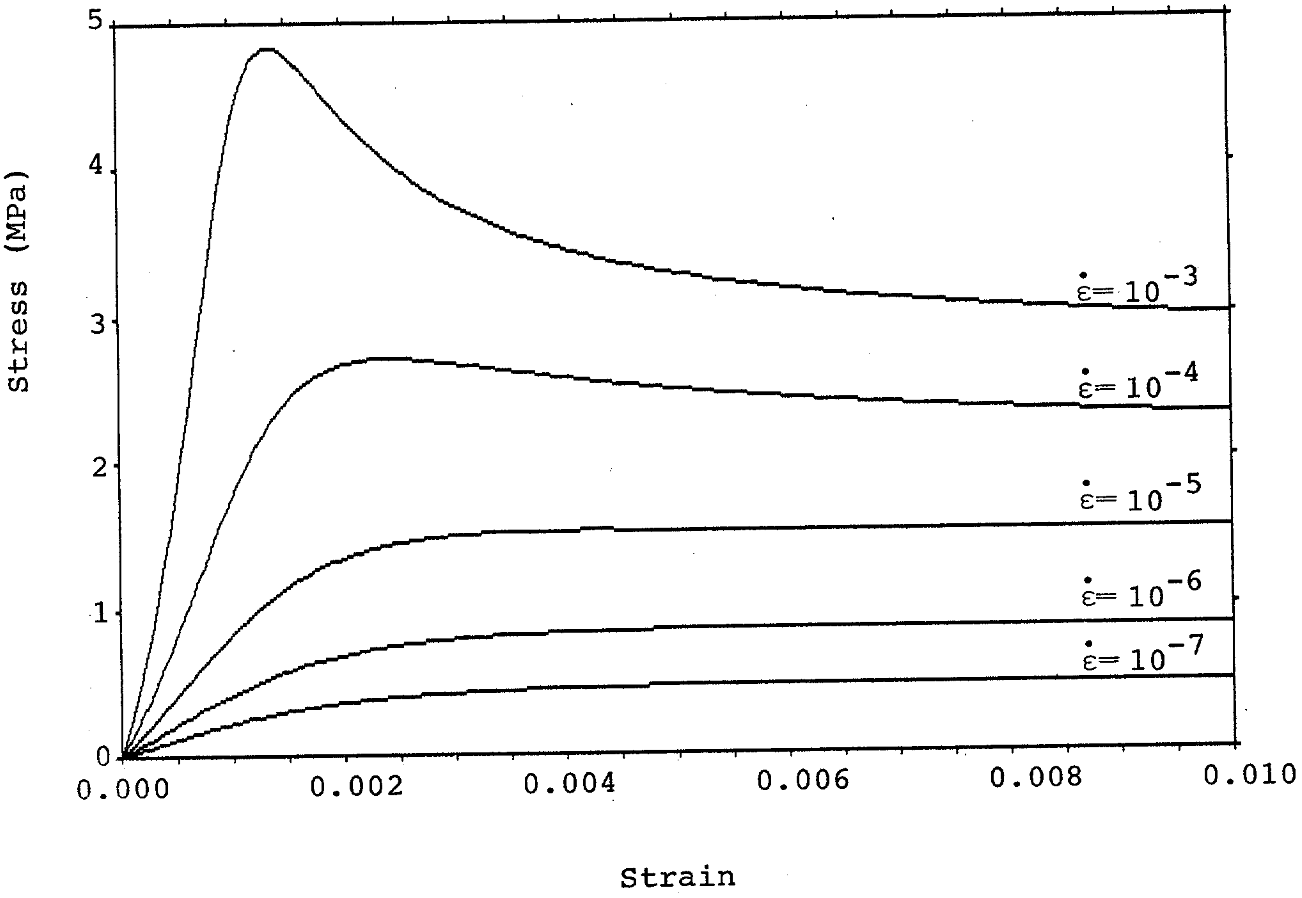

Figure 2.7 Stress-Strain Plots for Wang's (1982) Model for Different Strainrates.

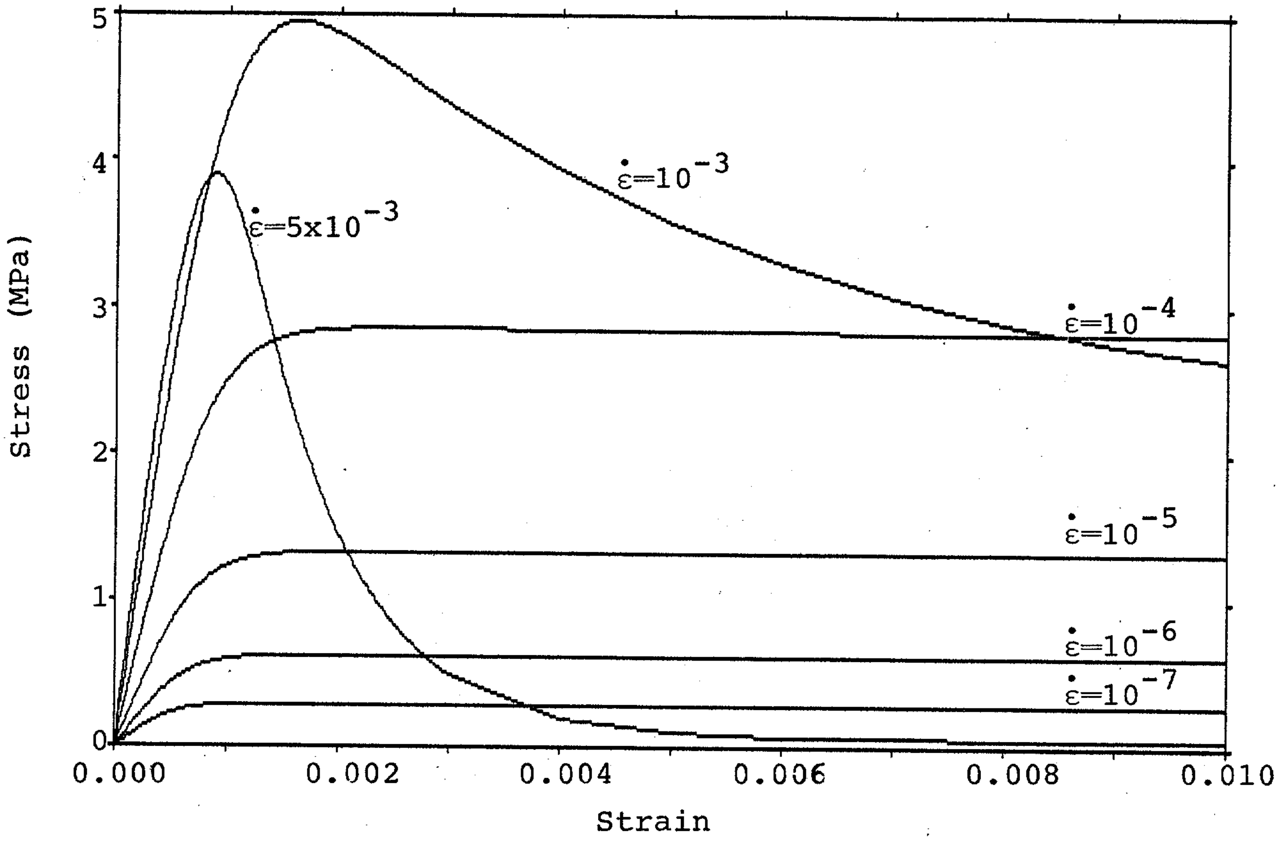

Figure 2.8 Stress-Strain Plots Under Constant Strainrate for Proposed Model.

effect may be modelled in general with a time-varying stress given by:

$$\sigma(t) = \sigma_n \, [1 - \exp(-at^b)] \tag{2.21}$$

where σ_n is the nominal creep stress, and a, b are constants. The rise time, t_r, is defined as the time required to reach 95% of the nominal creep stress. Given the rise time, the parameter a may be evaluated with:

$$a = - \ln 0.01/t_r{}^b \tag{2.22}$$

According to the proposed model, the rise time governs the extent of primary creep deformation associated with delayed elasticity.

Figures 2.9 to 2.11 present the creep test data observed by Sinha (1978) at a stress of 0.49 MPa and temperatures of -41°C, -30°C and -19.8°C, respectively. The predictions of creep strains and creep strain recovery associated with unloading for the model proposed here and that of Sinha (1978) are shown by the solid lines. The rise times as well as the finite times for unloading are indicated on the figures. The effect of varying the rise time is shown in Fig. 2.11b. In general the proposed model is able to describe the observed data as well if not better than Sinha's model. The tests at -30°C, Fig. 2.10, yield creep and recovery curves that are significantly variable under the same nominal conditions,

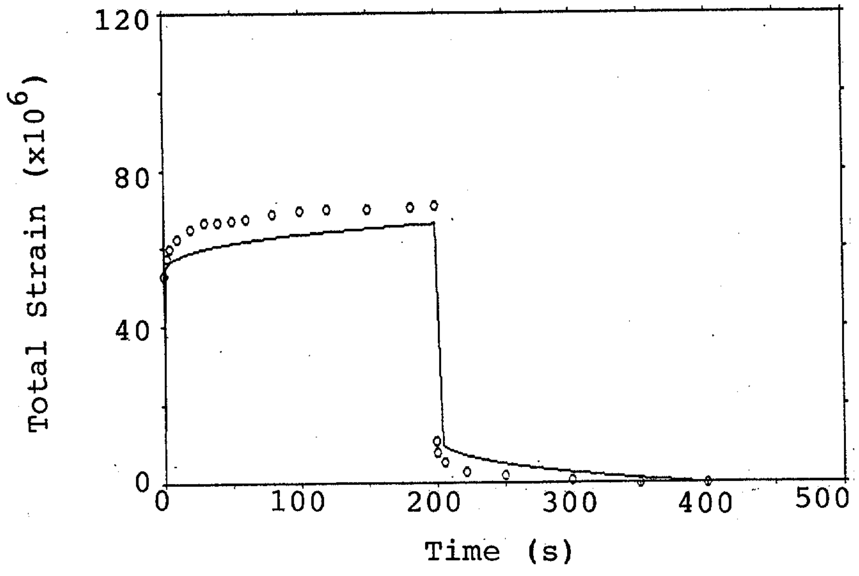

(a) Sinha's (1978) Model.

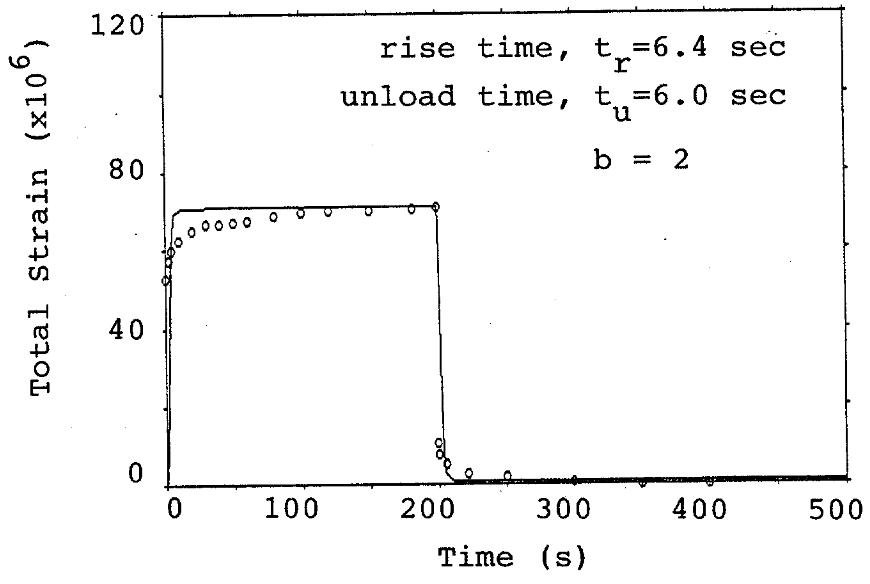

(b) Proposed Model.

Figure 2.9 Creep and Recovery of S-2 Ice at -41°C, 0.49 MPa Stress.

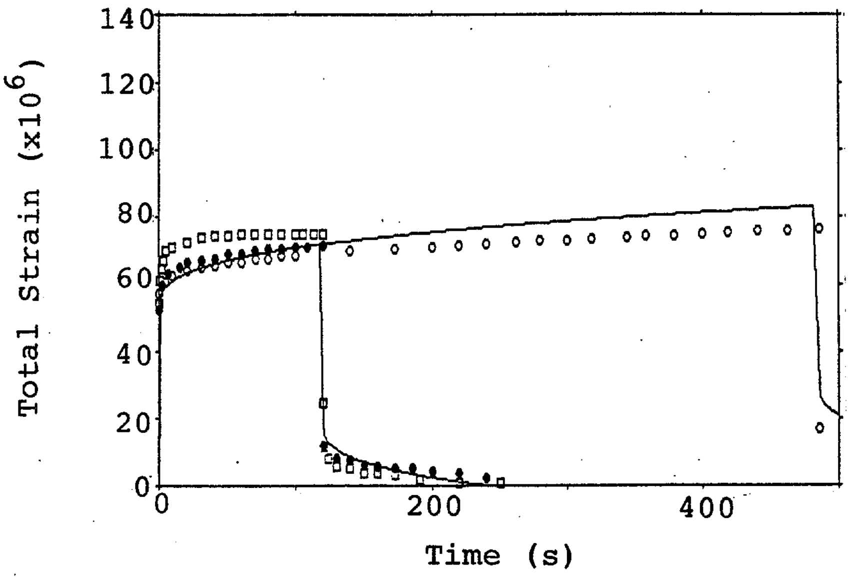

(a) Sinha's (1978) Model.

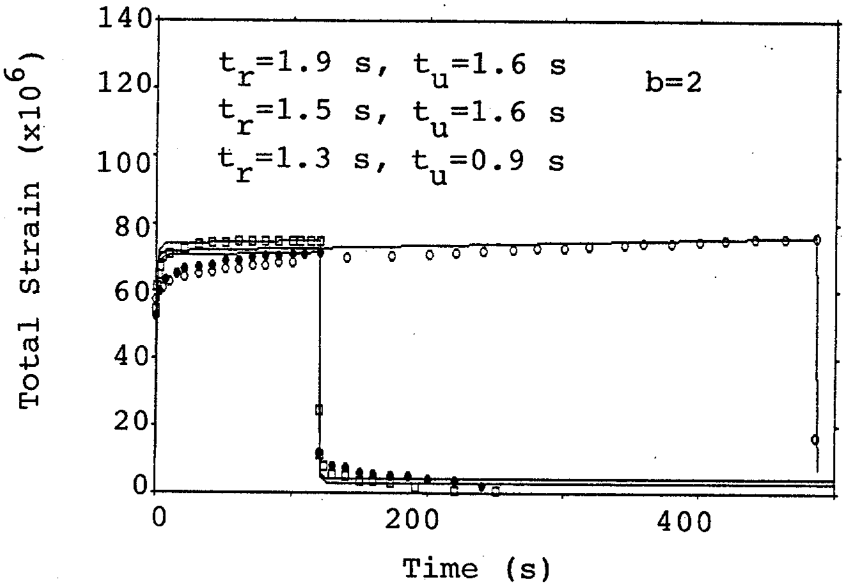

(b) Proposed Model.

Figure 2.10 Creep and Recovery of S-2 Ice at -30°C for Three Succesive Loadings of 0.49 MPa.

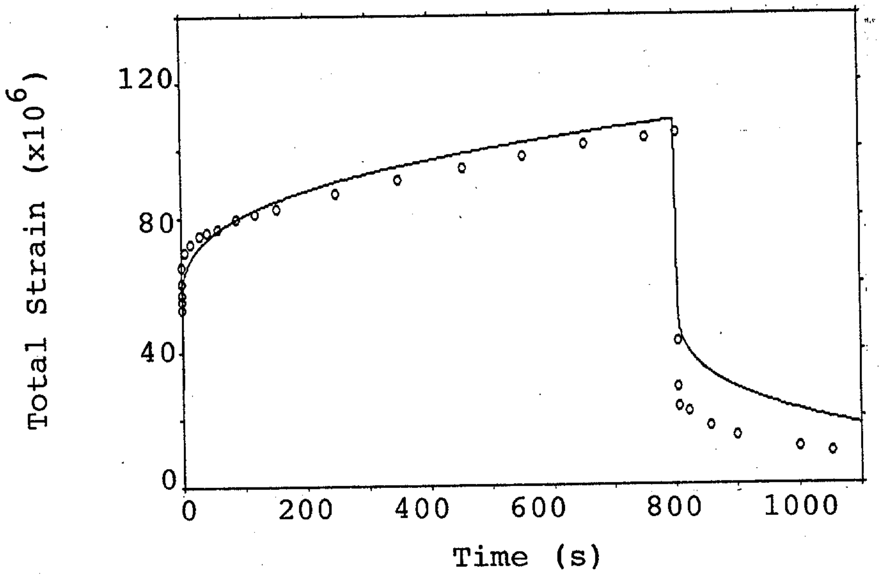

(a) Sinha's (1978) Model.

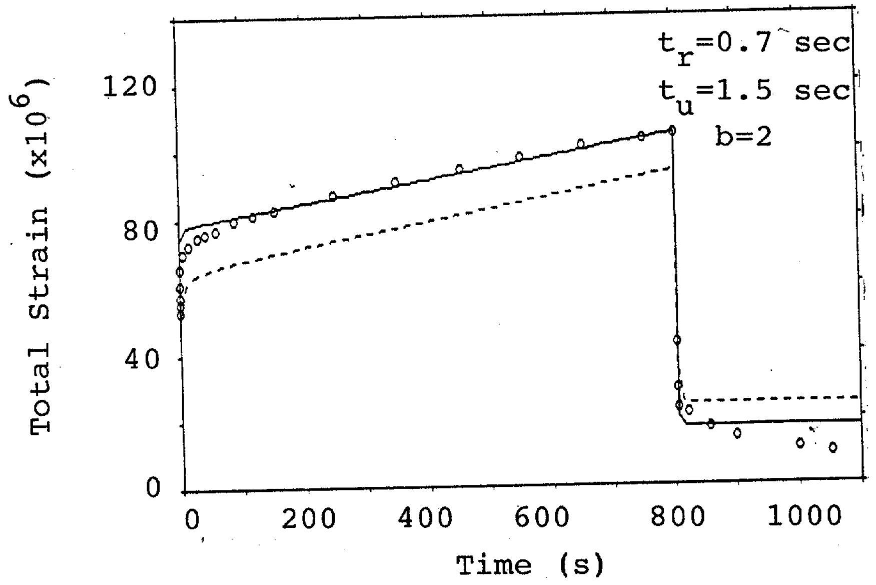

(b) Proposed Model (Dash Line for t_r=0.0)

Figure 2.11 Creep and Recovery of S-2 Ice at -19.8°C, 0.49 MPa Stress.

suggesting that most of the variability associated with the model predictions may be linked to this factor, i.e., difficulty in conducting repeatable creep tests. By changing the finite rise time from 1.3 to 1.9 seconds the proposed model is able to capture some of the variability, the remainder being the uncertainty in the finite rise time model and other experimental uncertainties not accounted for. It is also possible that some of the variability may be due to model uncertainty.

Figure 2.12a shows the experimental creep data of Brill and Camp (1961) for randomly oriented snow ice together with the predictions of the current model and the model of Sinha (1978). Two of the curves correspond to tests at -5°C and one to -10°C. It must be reiterated that the Arrhenius law loses validity at -5°C. The proposed model captures the overall data trend at -10°C and for the 0.232 MPa stress case at -5°C. The prediction is poor at -5°C for the 0.125 MPa stress case. Sinha's model however appears to fit the data quite well. To some extent this is made possible by the variation of grain size, a parameter which directly influences his formulation of the primary creep component of strain. The fit to the experimental data can be improved if the values of some of the model parameters are allowed to change within the limits of variability in material properties and experimental errors. By changing the value of b to 0.1 and using Q in the range of

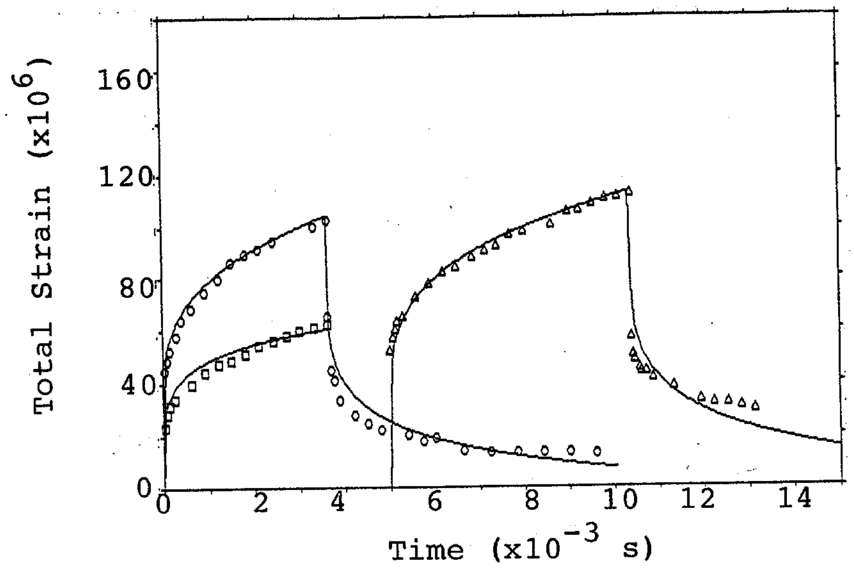

(a) Sinha's (1978) Model.

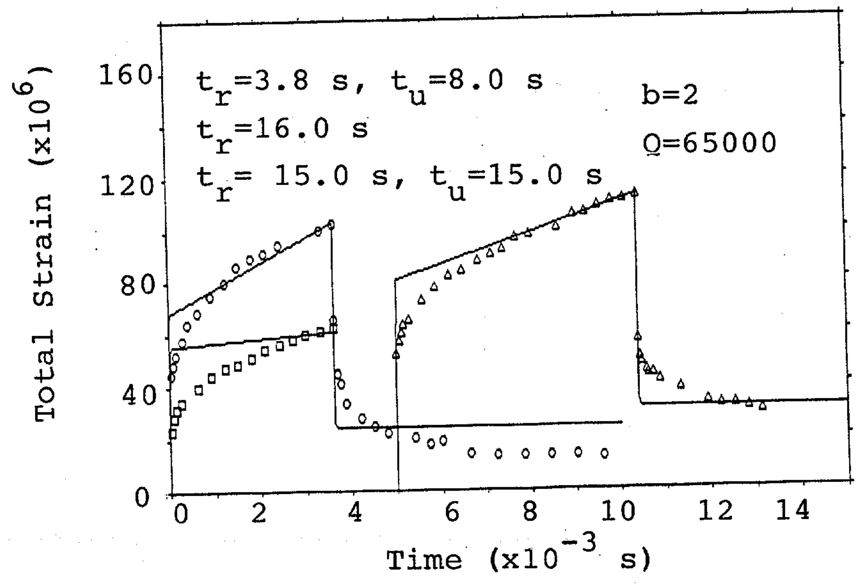

(b) Proposed Model.

Figure 2.12a Creep and Recovery of Snow Ice (Brill and Camp Data, 1961).

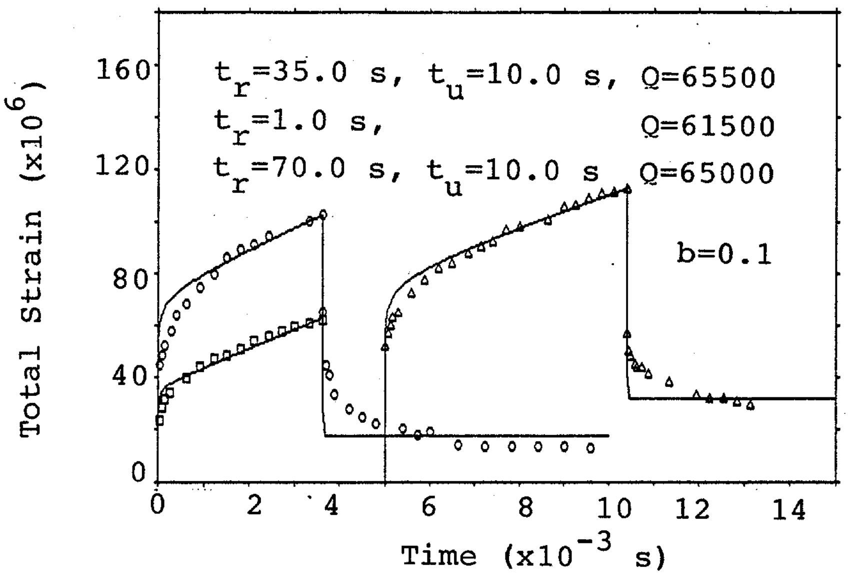

Figure 2.12b Creep and Recovery of Snow Ice (Brill and Camp Data, 1961)- Proposed Model.

61500 J mol^{-1} to 65500 J mol^{-1}, Fig. 2.12b shows a better fit to the experimental data.

Wang (1982) has generated creep curves using his semi-empirical model for sea ice as shown in Fig. 2.13. He found the curves to agree with experimental observations contained in Mellor (1980). Creep curves generated by the model proposed here are shown in Fig. 2.14. The proposed model provides good agreement with the curves of Wang.

Constant Stressrate Tests -- Experimental data obtained during constant stressrate tests is limited. Figure 2.15 contains the "strength" versus stressrate data for sea ice obtained from two independent sources. The data normalized for temperature and salinity effects is plotted in Fig. 2.16. The solid line in the figure is the prediction of the proposed model. For stressrates greater than about 0.05 MPa s^{-1}, the fracture strainrate of 10^{-2} s^{-1} is reached only after the stress exceeds 5 MPa, the fracture stress at this strainrate in constant strainrate tests. Assuming that in constant stressrate tests material failure is governed by the fracture strainrate, not fracture stress, the maximum stress just prior to fracture defines the strength. The validity of this assumption is justified since the model predicts the observed behavior quite well. For lower stressrates, the model over predicts the strength. A careful study of the stress-strain curves (see Fig. 2.17) shows that while they appear to reach their failure stress values at strain values of 1-5%, in

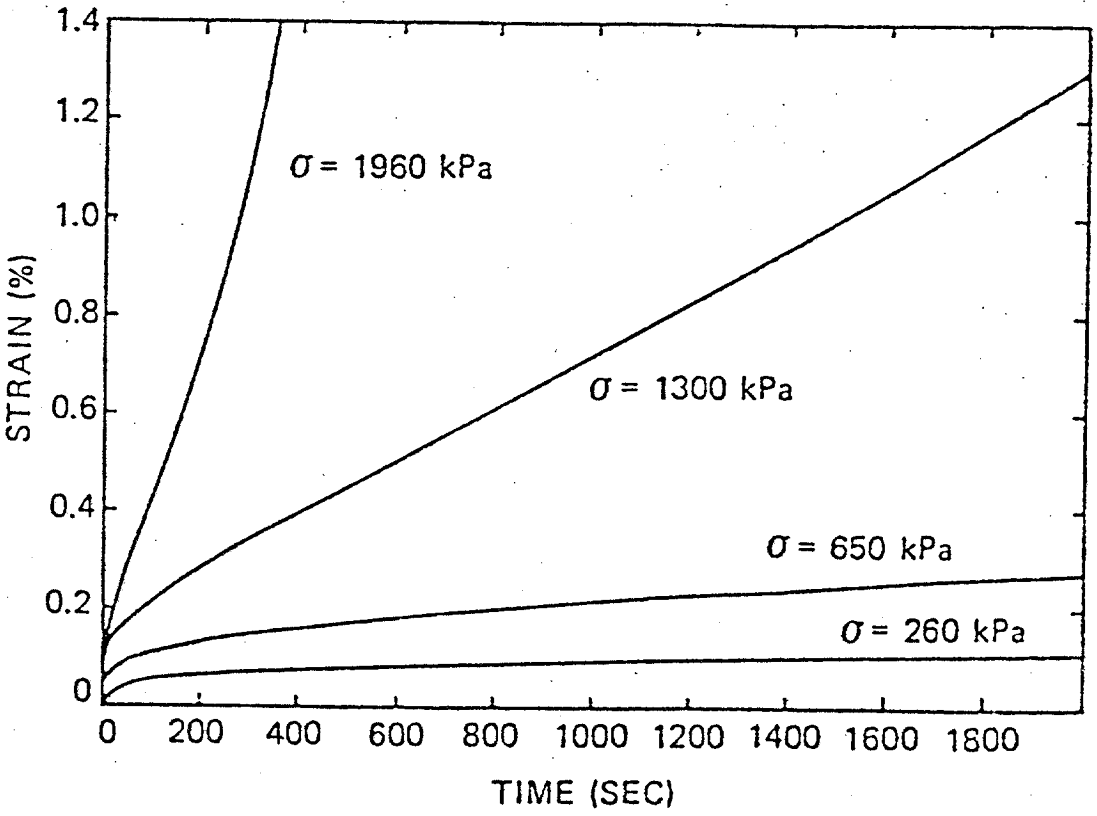

Figure 2.13 Calculated Creep Curves (Wang, 1982).

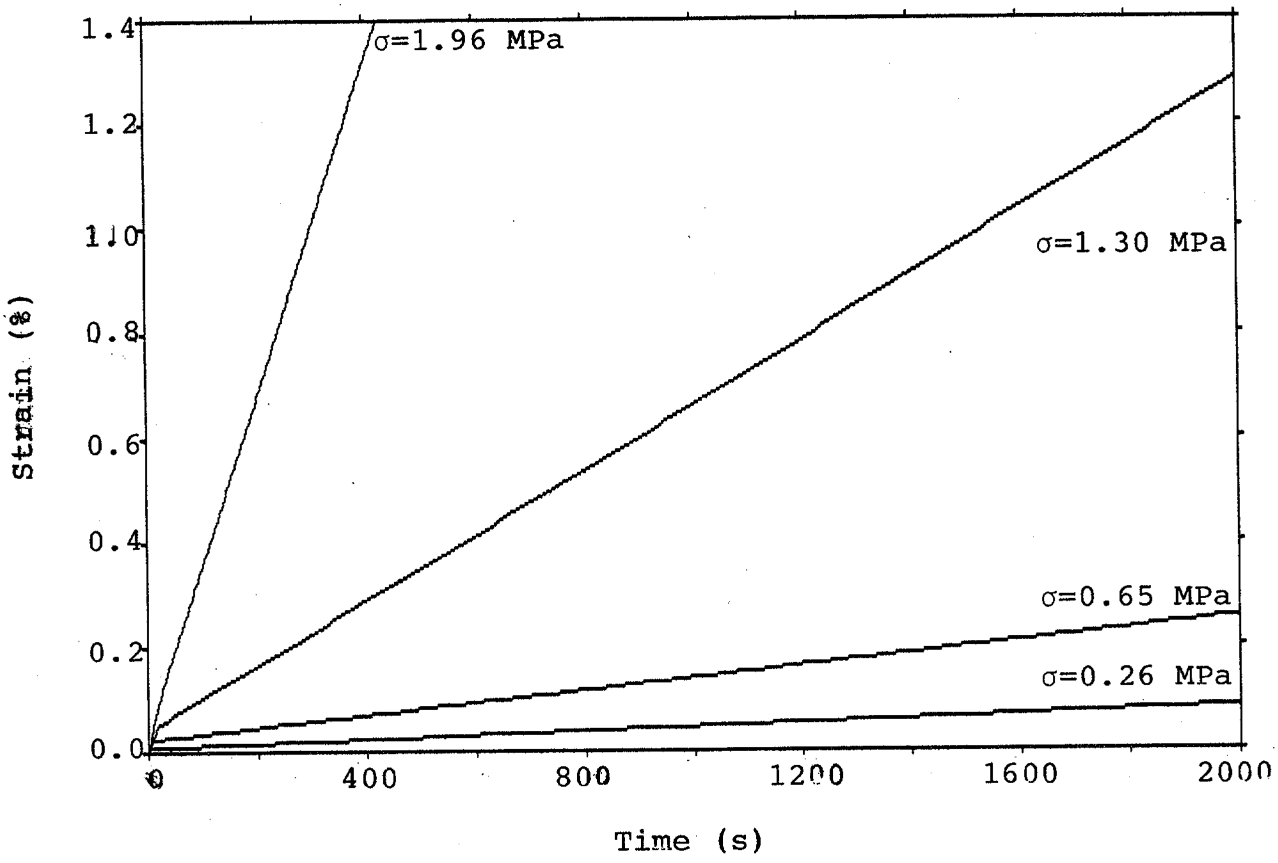

Figure 2.14 Calculated Creep Curves Based on the Model ($b=2$, $t_r=1.0$ sec.).

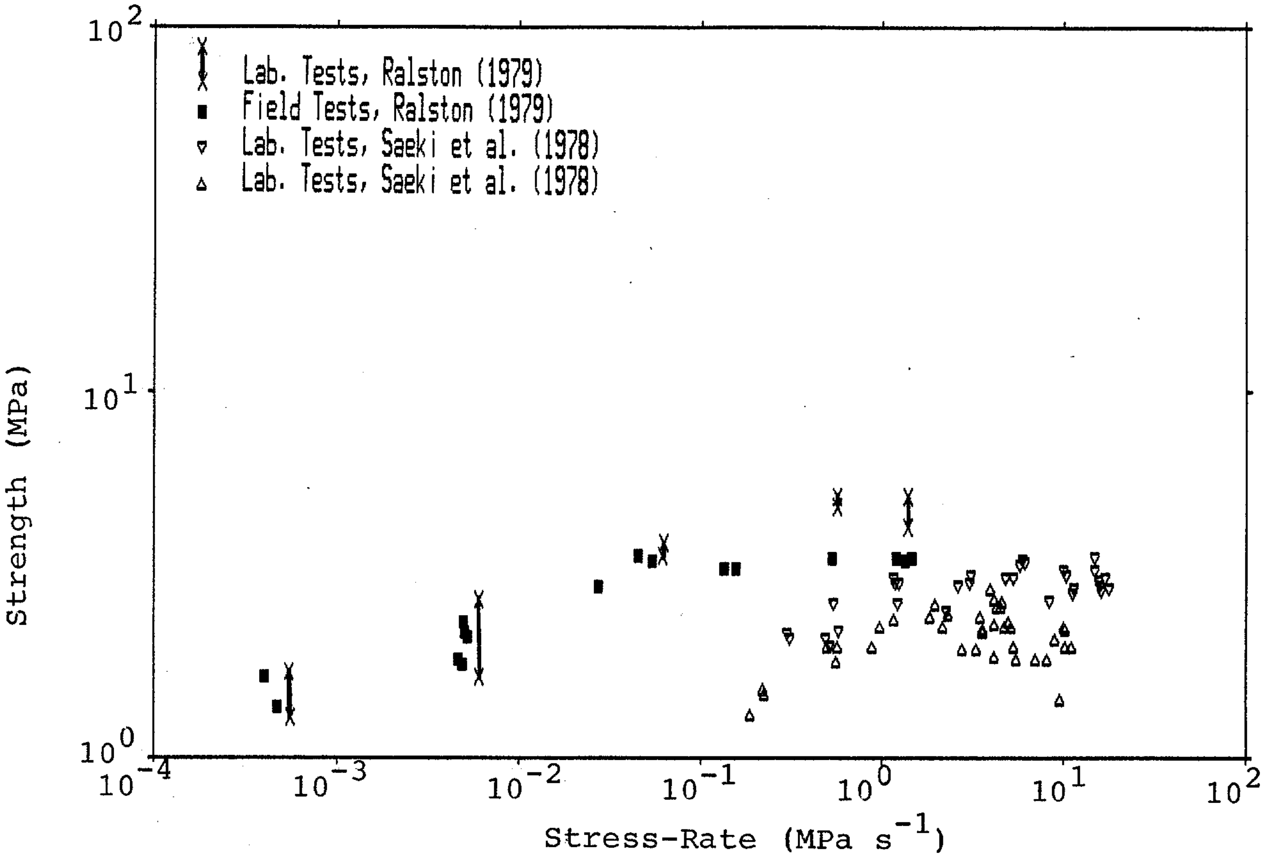

Figure 2.15 Strength of Sea Ice as a Function of Stress-Rate.

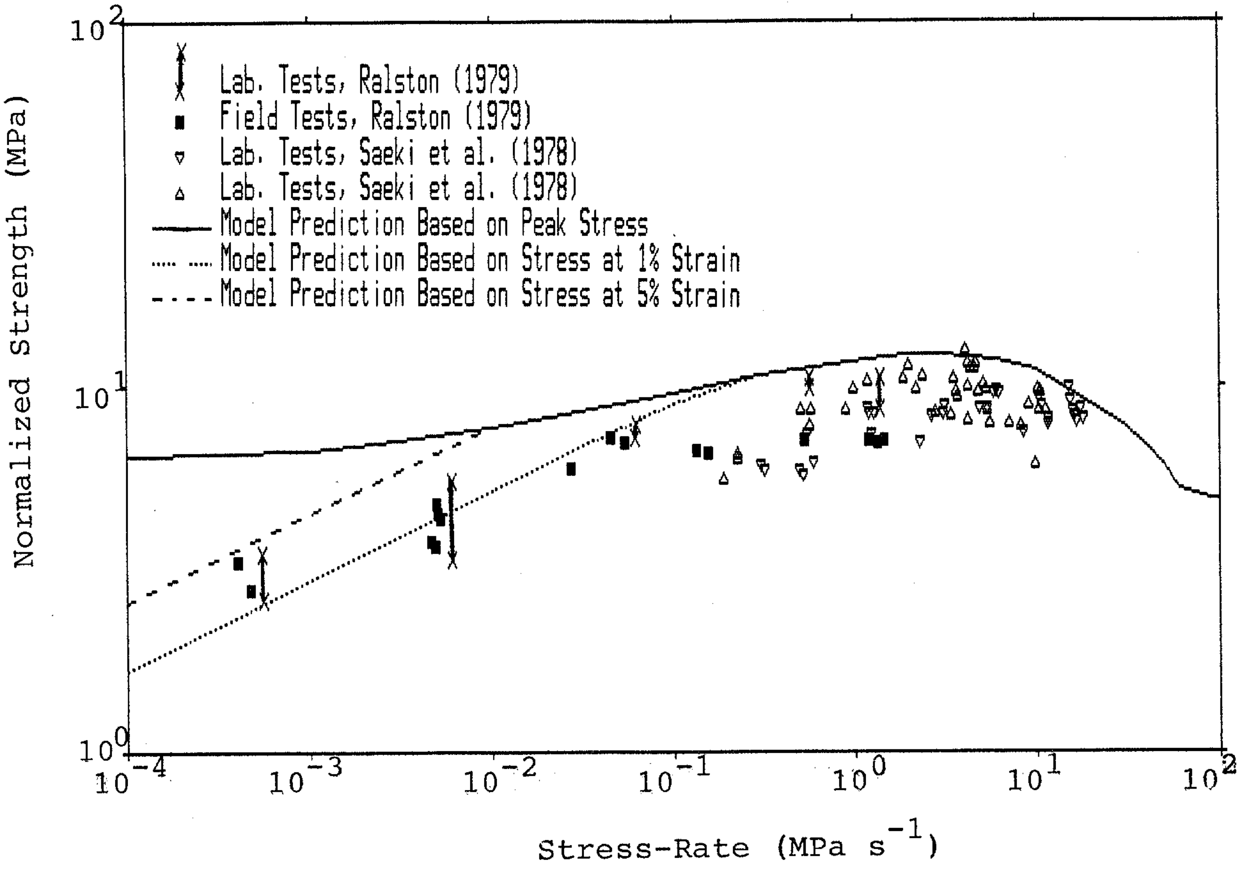

Figure 2.16 Strength of Normalized Ice as a Function of Stress-Rate.

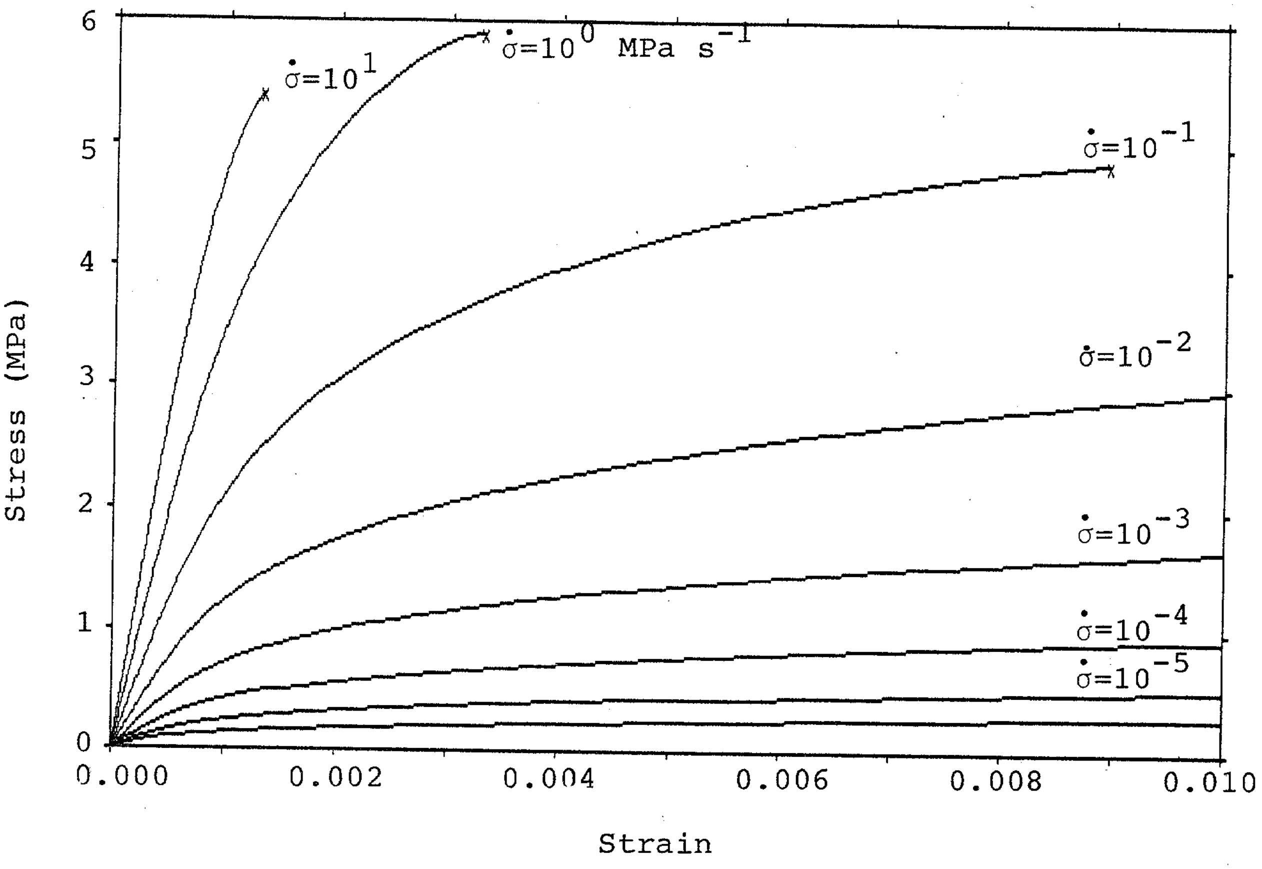

Figure 2.17a Stress-Strain Behaviour Under Constant Stress-Rate Loading Conditions.

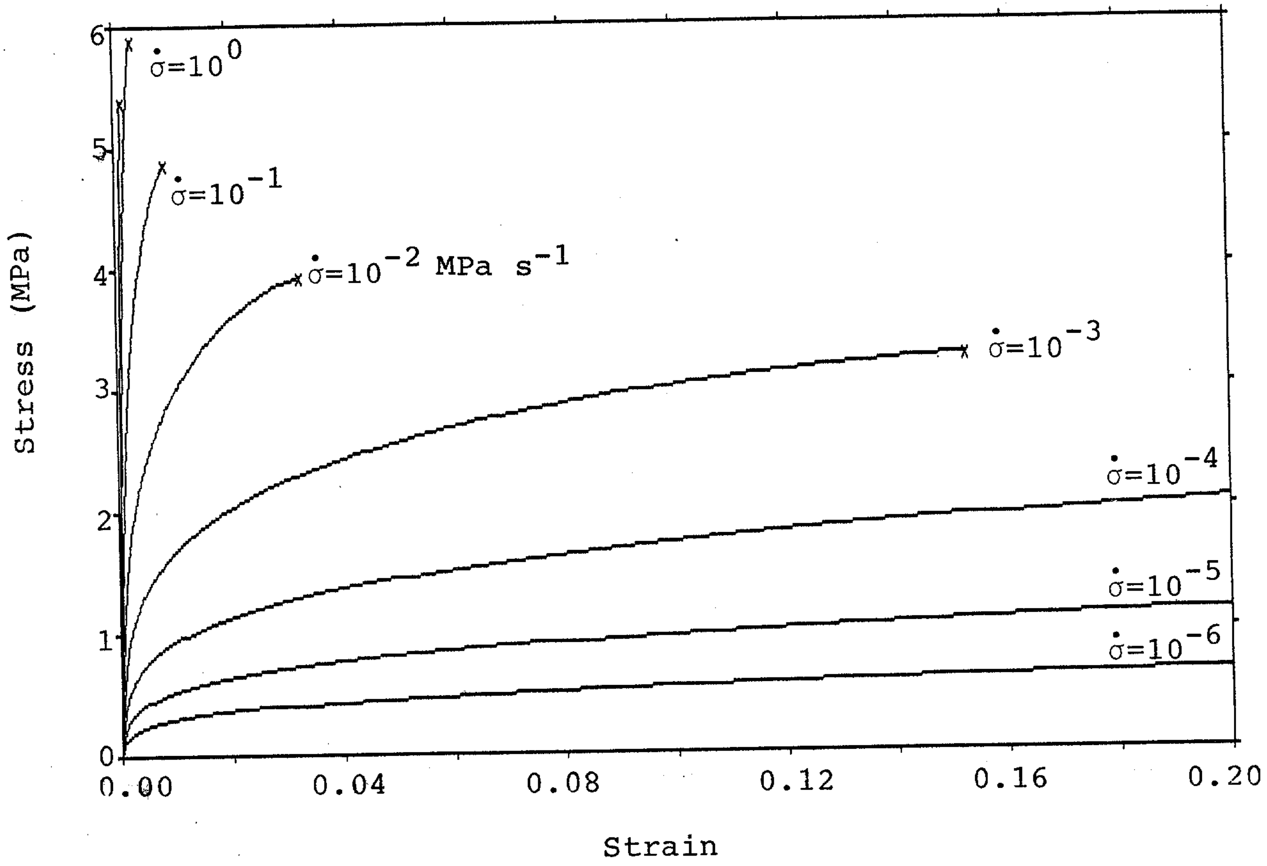

Figure 2.17b Stress-Strain Behaviour Under Constant Stress-Rate Loading Conditions.

fact the stress keeps increasing further. It is therefore possible that experimental observations are made prematurely and as such do not reflect the actual "strength". Wang (1982) assumed the limiting strain for constant stressrate tests to be 1%. If this is assumed, the dotted line in Fig. 2.16 captures the overall trend of the data very well even for low stressrates.

The stress-strain curves predicted by the semi-empirical model of Wang (1982) under constant stressrate conditions are shown in Fig. 2.18. Beyond a certain strain value the solution ceases to exist. The predictions were found to agree reasonably well with his earlier test results (Wang, 1979a). The curves predicted by the model proposed here and shown in Fig. 2.17 are in good agreement with Wang's curves.

Effective Elastic Modulus -- Data on the strainrate variation of the effective elastic modulus is plentiful (see Mellor, 1983). The experimental data of Traetteberg, Gold and Frederking (1975) on pure columnar-grained ice at -10°C is presented in Fig. 2.19. Predictions of the effective elastic modulus based on the proposed model is indicated by the solid line, which suggests an excellent match with the observed data.

Other Model Characteristics -- The ratio of residual stress to peak stress ("strength") is plotted versus strainrate in Fig. 2.20. There is an almost exponential decay

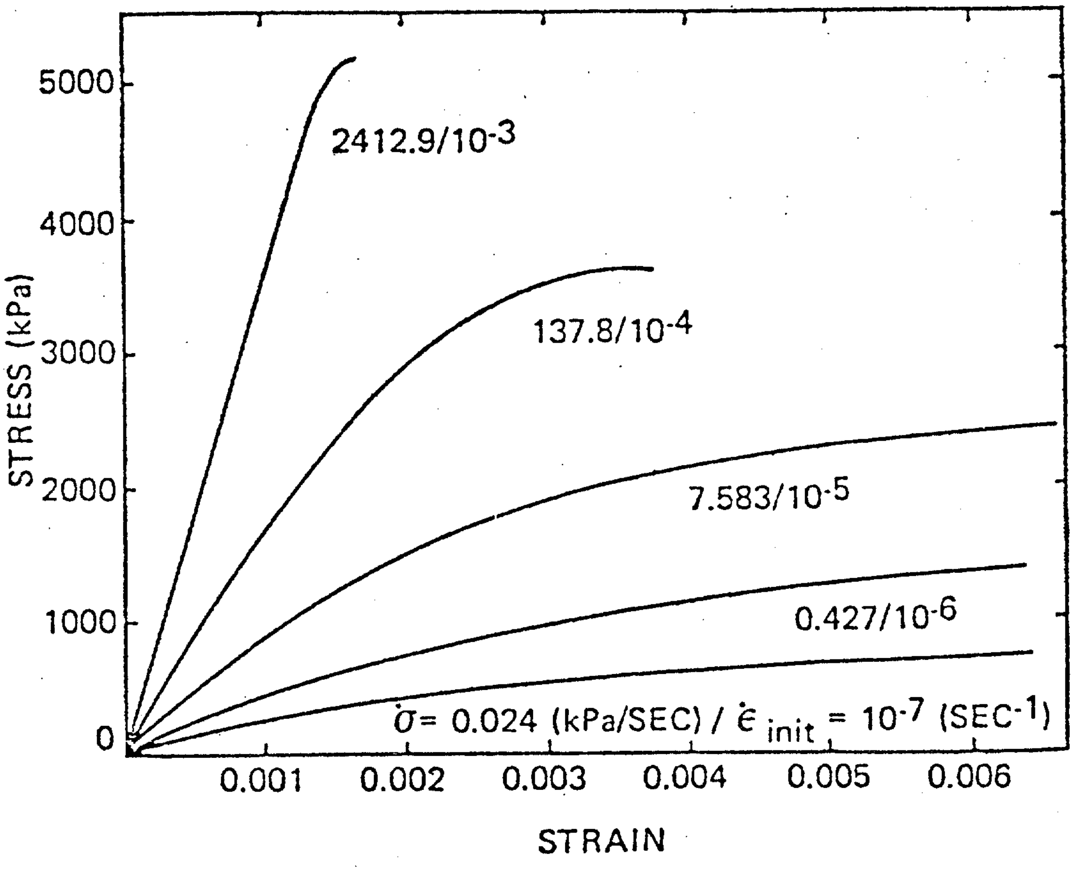

Figure 2.18 Calculated Stress-Strain Curves for Unoriented Columnar Sea Ice Under Constant Stress Rate Loading (Wang, 1982).

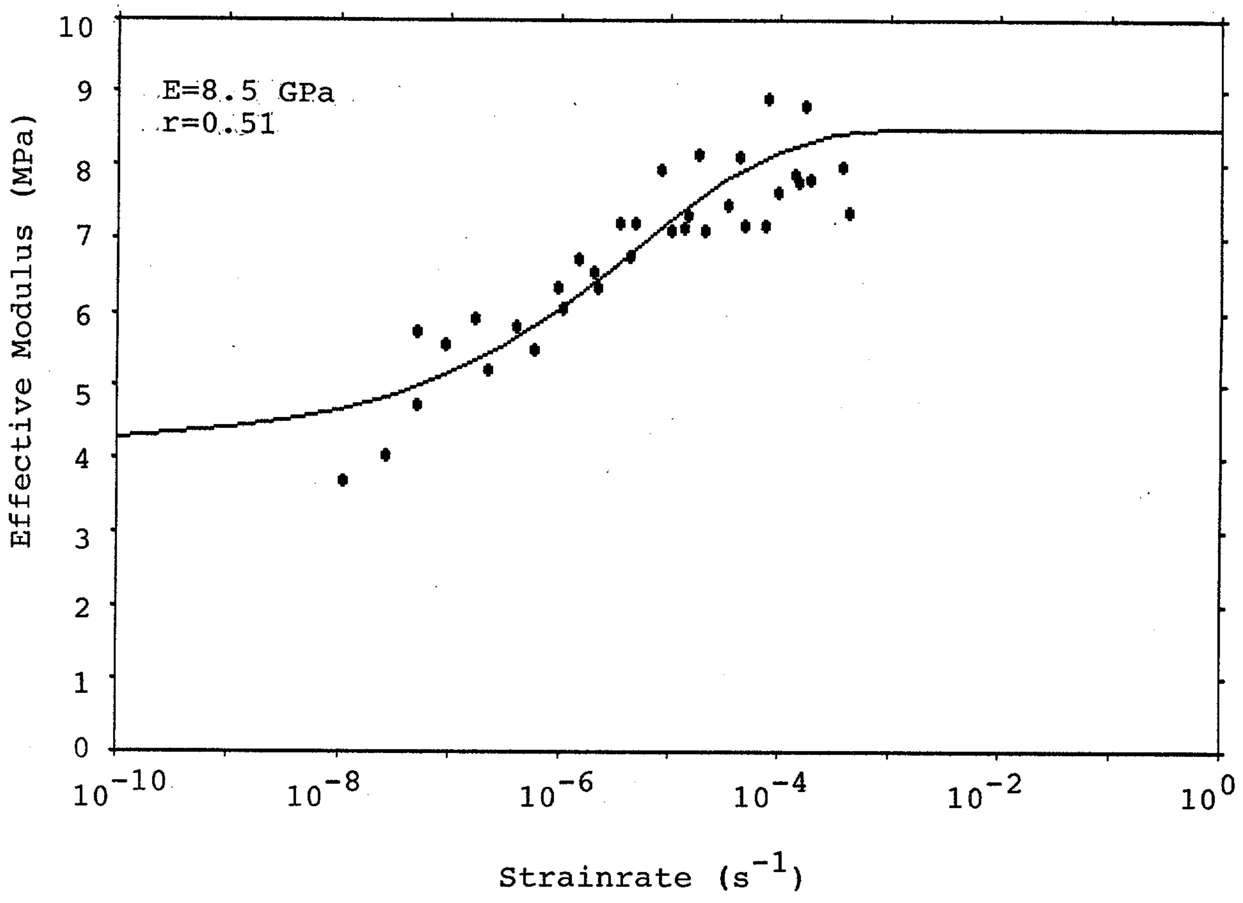

Figure 2.19 Effective Modulus versus Strainrate.
(Traetteberg, Gold and Frederking, 1975)

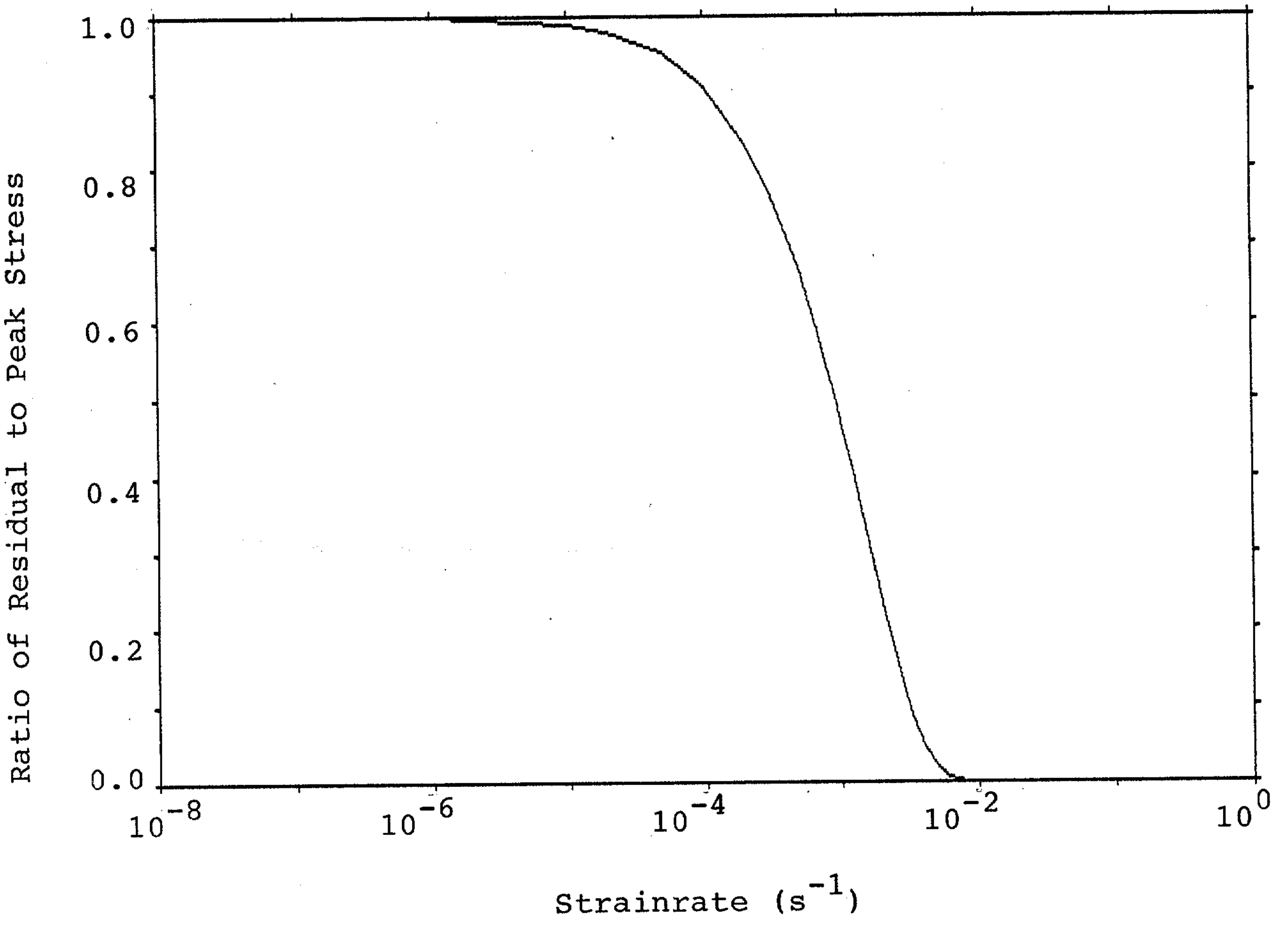

Figure 2.20 Ratio of Residual to Peak Stress as a Function of Strainrate.

of the ratio, and the value tends to zero as strainrate approaches 10^{-2} s^{-1}. For strainrates below about 10^{-6} s^{-1}, there is virtually no damage and the ratio tends to one.

The test in which a suddenly applied constant stress is followed by a condition in which the strain is kept constant often results in a stress reduction. This phenomenon is termed stress relaxation. Figure 2.21 shows the stress relaxation for the proposed model during a creep test conducted at 3 MPa. The amount of relaxation is dictated by the numerical value of the parameter r. If r=1 and the strainrate is zero, the effective modulus equals zero. Equation 2.10 predicts the stressrate to be zero and thus no stress relaxation is possible. A value of r less than one is necessary to model the stress relaxation phenomenon.

The simulation of unloading and reloading requires specification of how the unloading or reloading is to take place. In a constant strainrate test, unloading could imply a change in the sign of the constant strainrate or simply the setting of stress equal to zero. Reloading may be defined in similar terms. Figure 2.22 shows unloading and reloading based on controlling strainrate, while in Figs. 2.23 and 2.24, unloading is stress controlled while reloading is strainrate controlled. In both cases, the model follows the virgin loading curve once the effect of the unloading/reloading ends. Hysteresis loops are observed for low unloading rates

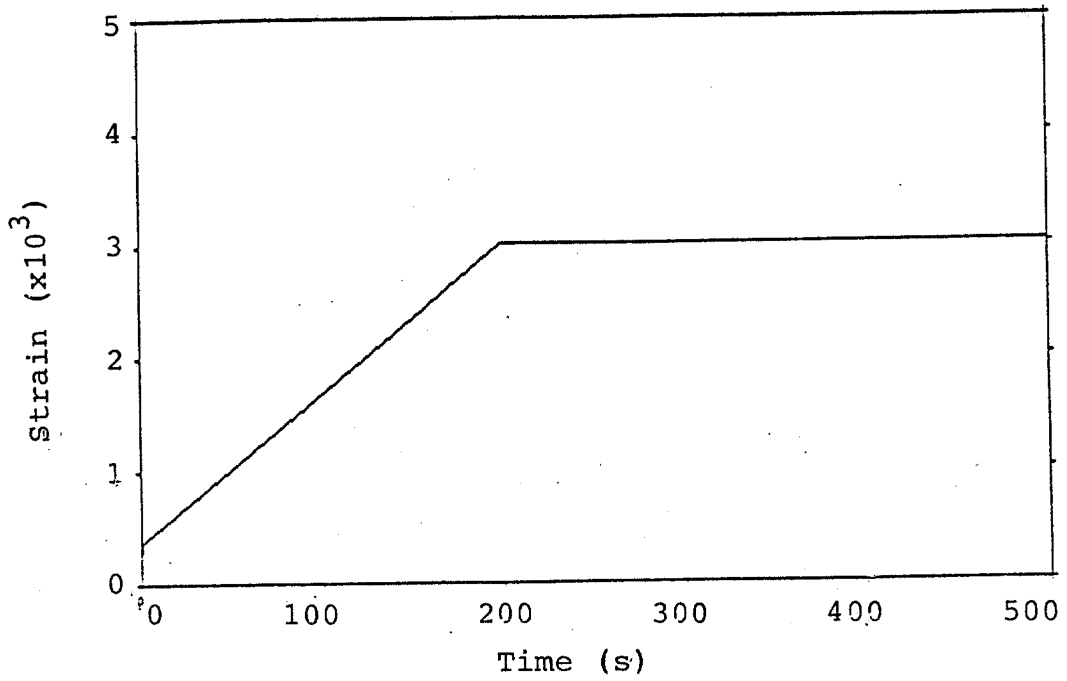

(a) Strain History

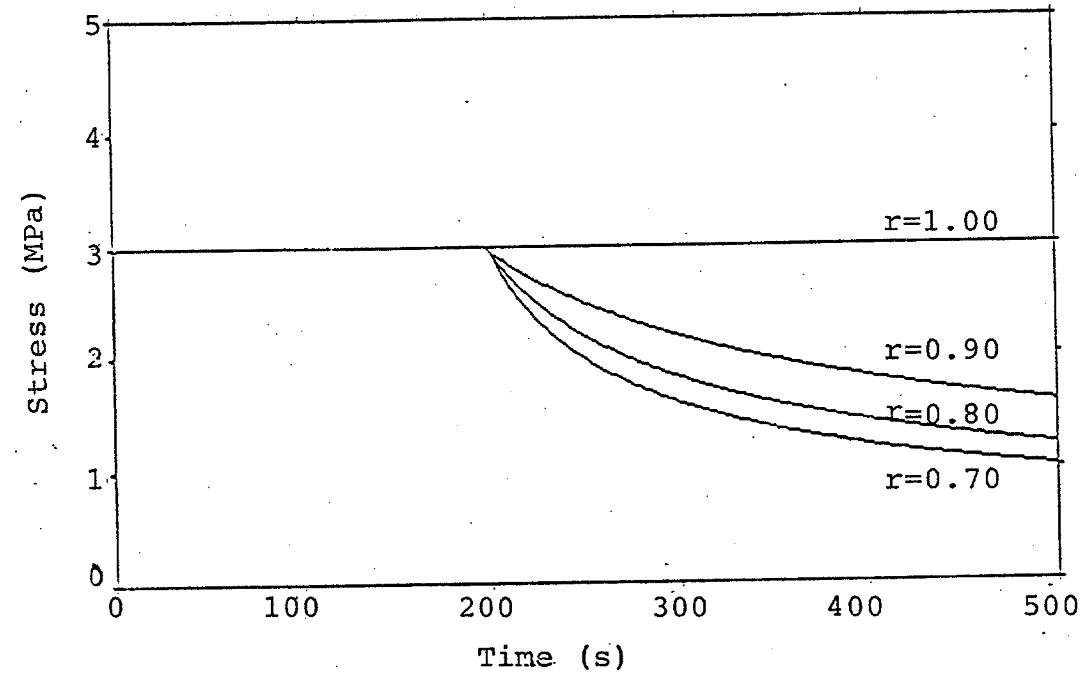

(b) Stress History

Figure 2.21 Stress Relaxation.

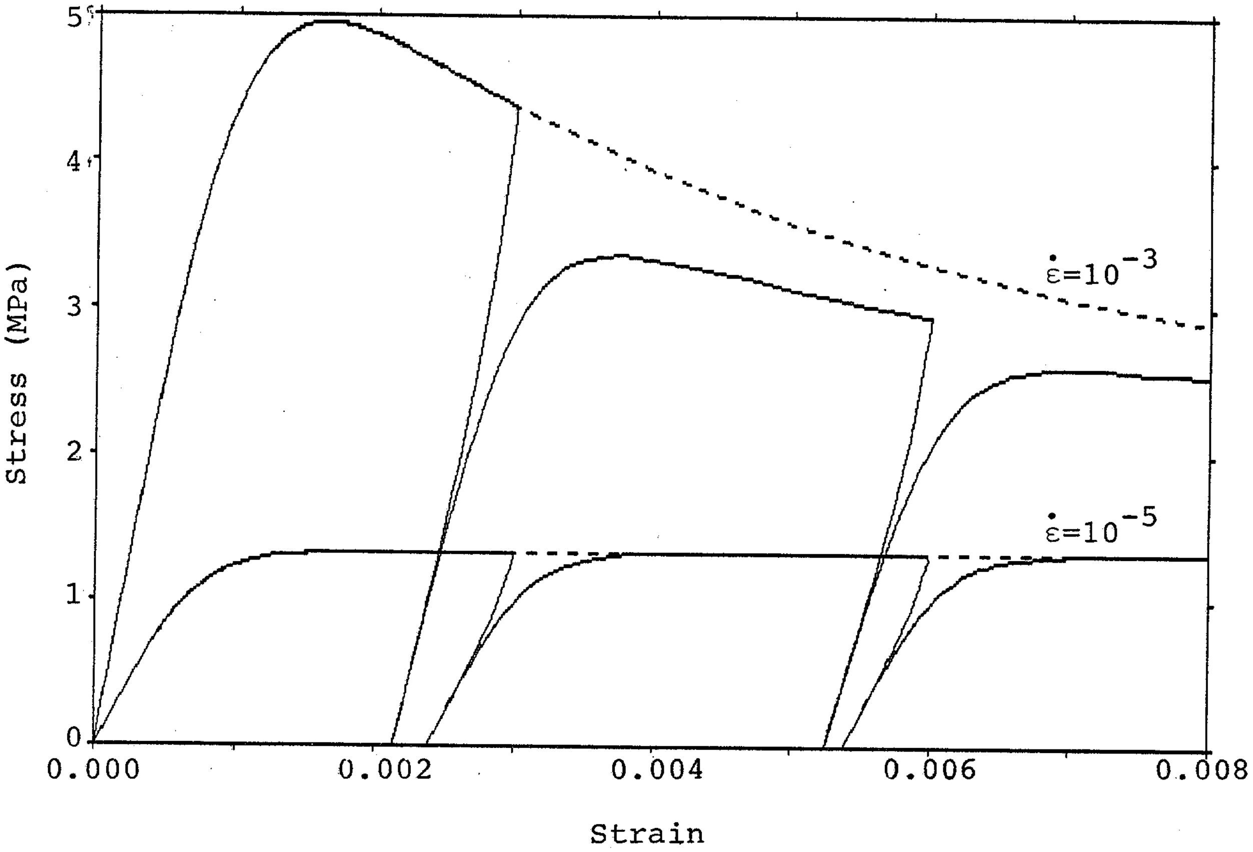

Figure 2.22 Unload and Reload at Constant Strainrates, (Dash Lines for No Unloading).

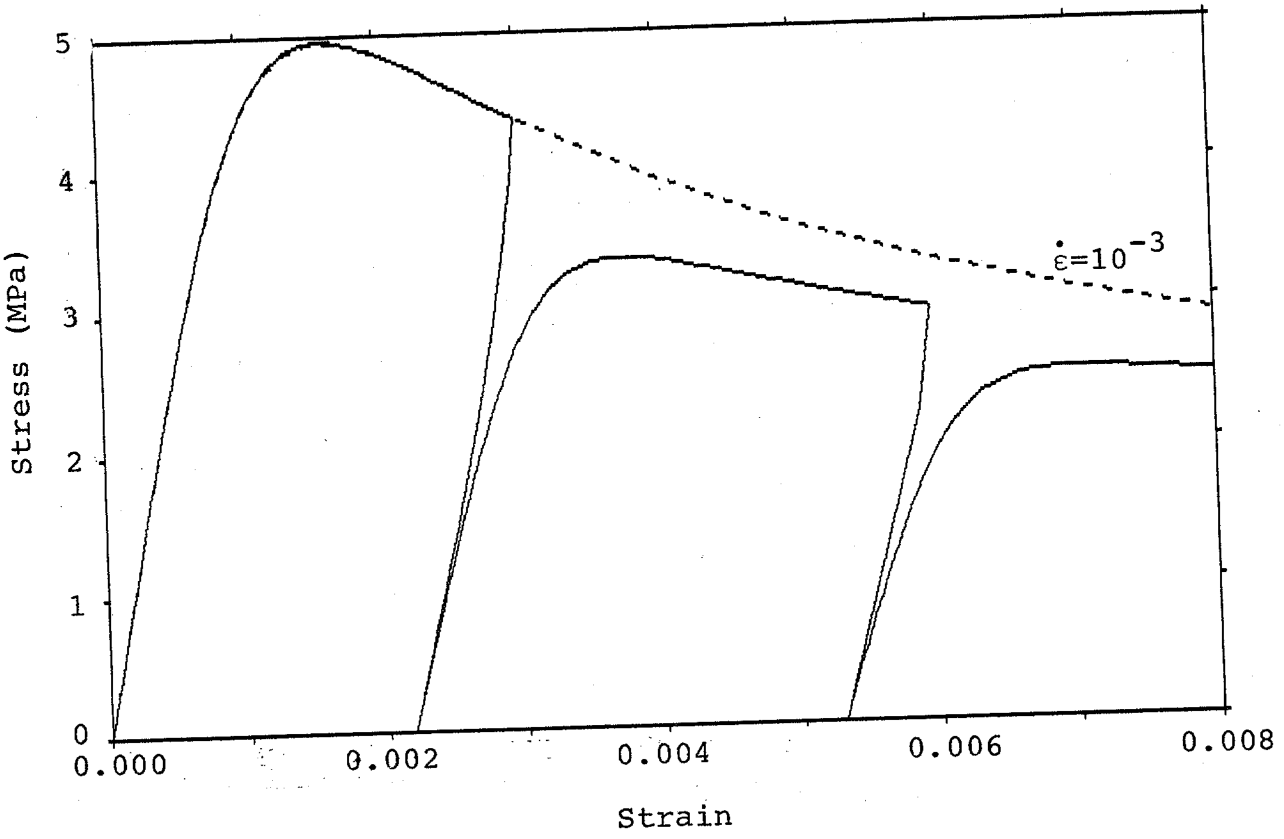

Figure 2.23 Unload at Constant Stress-Rate of -5.0 MPa s^{-1}, Reload at Constant Strainrate of 10^{-3} s^{-1}.

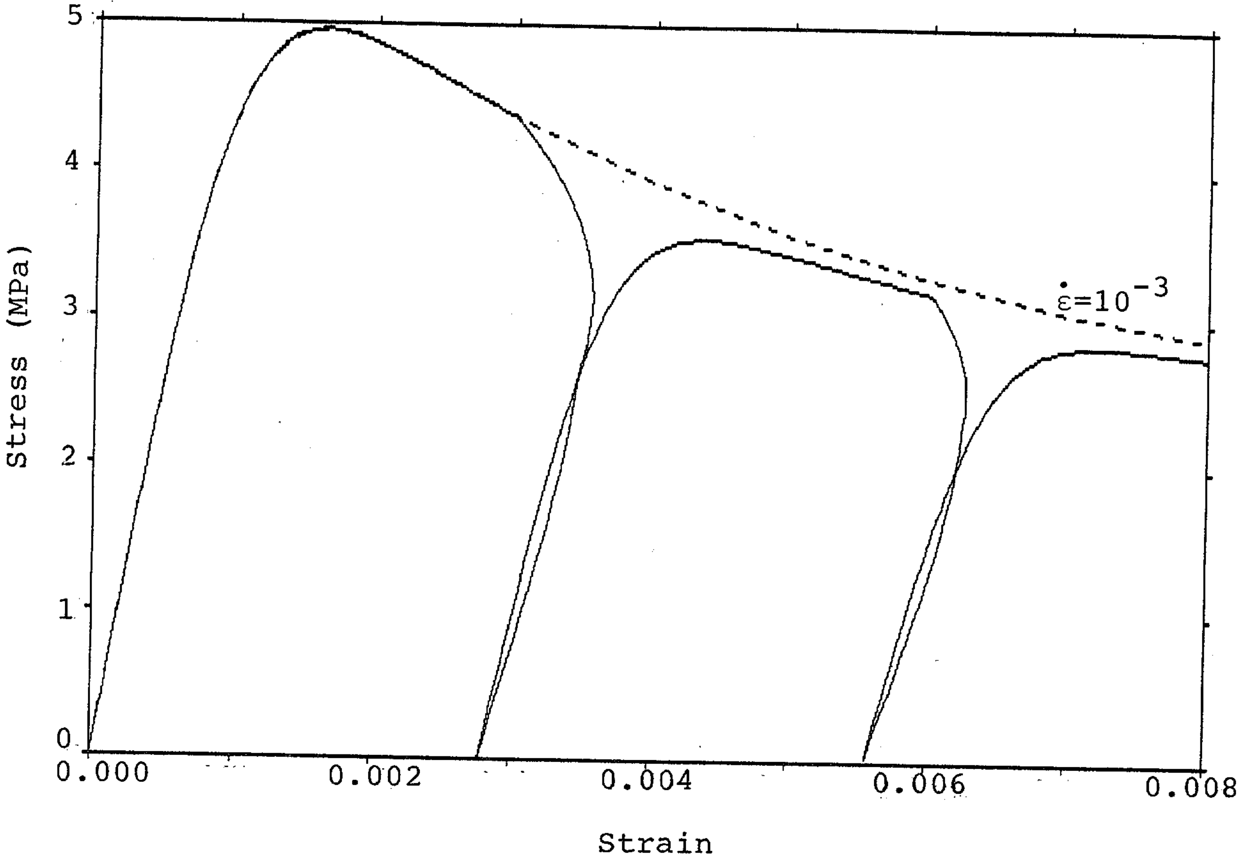

Figure 2.24 Unload at Constant Stress-Rate of -1.0 MPa s^{-1}, Reload at Constant Strainrate of 10^{-3} s^{-1}, (Dash Line for No Unloading).

(Fig. 2.24), but are hardly visible for fast unloading rates (Fig. 2.23). This is due to the lack of time for the material to creep at fast unloading rates. Figure 2.25 represents a sinusoidal variation of stress between zero and a prescribed maximum value. Experimental data of Mellor and Cole (1981) show hysteresis loops under similar test conditions. It must be noted that the model parameters used here are for sea ice and not pure ice used by Mellor and Cole. In any case, this issue requires further study.

2.5. MULTIAXIAL MODEL FORMULATION AND CALIBRATION

Sea ice is not an isotropic material. Field observations have shown that this type of ice, which is predominantly columnar, has two sources of anisotropy: (a) the c-axis is oriented perpendicular to the axis of crystal growth, and (b) the c-axes of different crystals may show preferred azimuthal orientation in the plane on which they lie. There is strong evidence suggesting that the preferred azimuthal orientation is correlated with the instantaneous current direction just underneath a growing ice sheet (Weeks and Gow, 1978, Langhorne, 1982, and Langhorne, 1983). While such alignments are common in landfast ice, observations suggest that strong alignments can develop in pack ice when there is little rotation of the floes relative to the current direction (Cherepanov, 1971, and Kovacs and Morey, 1980).

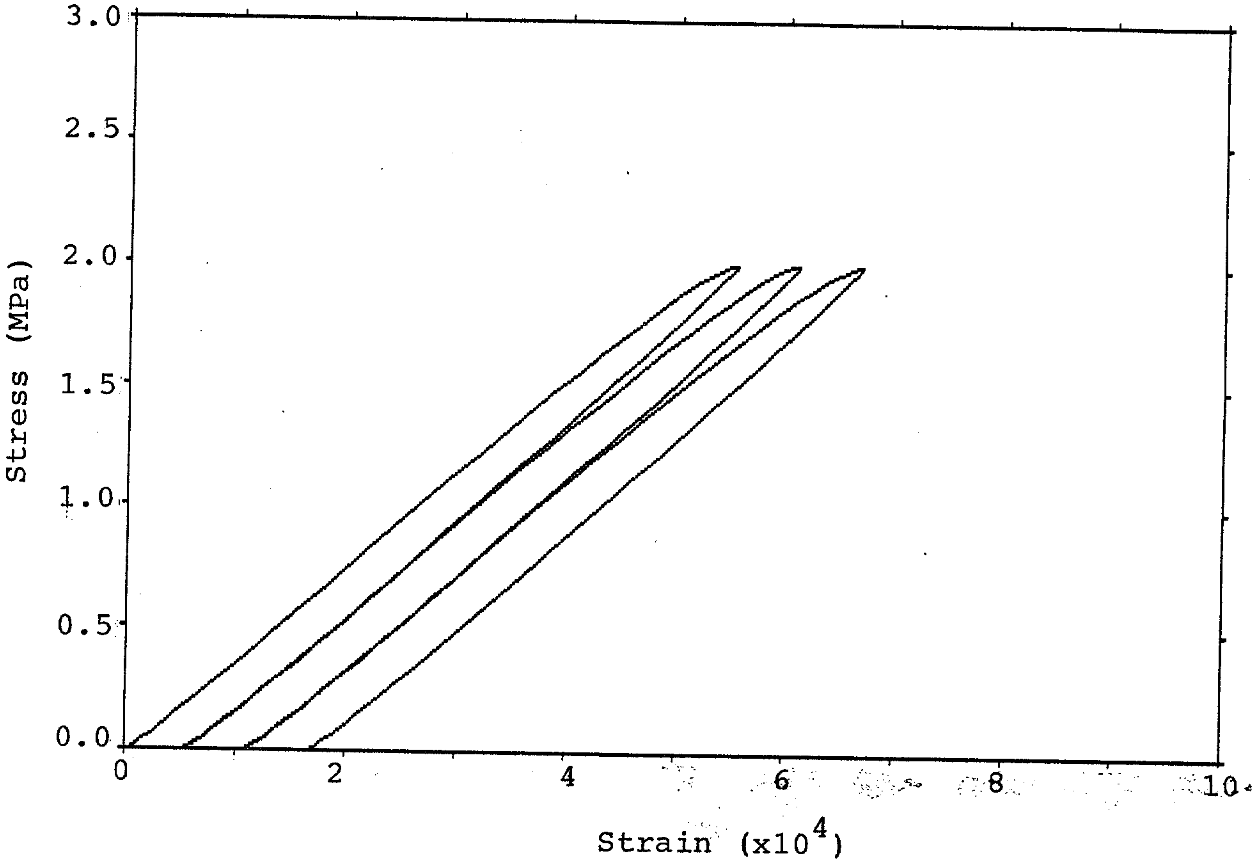

Figure 2.25 Cyclic Stress Load at 1 Hz.

The anisotropy of sea ice strongly influences the macromechanical behavior of first year sheet ice, while its influence on the behavior of multi-year floes, though less well studied, may be less. In first year sheet ice, the first source of anisotropy leads to a ratio of vertical to horizontal stress at constant strainrate varying from 2 to 5 (Butkovich, 1959, Peyton, 1966, Vaudrey, 1977, Sinha, 1983a, and Frederking, 1983), while the second source of anisotropy leads to stress ratios of 0.25-0.60 at a 45 degree azimuthal angle to the c-axis and 0.50-0.95 at a 90 degree angle (Wang, 1979b, Vittoratos, 1979, Richter-Menge, et al., 1985, Peyton, 1968).

Theoretical formulations which account for anisotropy in ice with a transversely isotropic model have been developed by Reinicke and Ralston (1977) and by Vivatrat and Chen (1985). The former model is based on plasticity theory and considers ice to be a pressure sensitive material as well. On the other hand, the latter is a pressure insensitive, elastic-power law creep formulation.

The development presented here is based on an orthotropic generalization of the uniaxial, rate-sensitive damage model. Only the continuum (i.e., flow) behavior of ice is sought to be modelled, not the fracture behavior. Microcracking leading to damage is also considered to represent continuum behavior. The fracture model for ice is described in the next chapter.

As a result of this separation, a pressure insensitive model which predicts similar behavior in compression and tension is studied in detail. Such a model appears to be reasonable for sea ice as justified by experimental data.

Theoretical Formulation -- The multiaxial generalization of Eq. 2.11 may be expressed in matrix notation as:

$$\underline{\dot{\varepsilon}} = \underline{C}\,\underline{\dot{\sigma}} + \underline{\dot{\varepsilon}}_{cr} \qquad (2.23)$$

where $\underline{C}$ is the linear elastic compliance matrix for an orthotropic material (see Appendix A), and the remaining vectors are in general of size (6x1) in engineering notation.

To derive the relationship between the creep strainrate and stress vectors, an effective stress measure generalized for orthotropic materials with identical behavior in compression and tension is first defined.

$$\sigma_e^2 = 3/\beta\ [\frac{a_1}{3}(\sigma_{xx}-\sigma_{yy})^2 + \frac{a_2}{3}(\sigma_{yy}-\sigma_{zz})^2 + \frac{a_3}{3}(\sigma_{zz}-\sigma_{xx})^2$$

$$+ 2a_4\,\sigma_{xy}^2 + 2a_5\,\sigma_{yz}^2 + 2a_6\,\sigma_{zx}^2] \qquad (2.24)$$

with $\beta = a_1 + a_2$. This may be expressed in compact form using matrix notation as:

$$\sigma_e^{\ 2} = 3/\beta\ \underline{\sigma}^T\,\underline{G}\,\underline{\sigma} \qquad (2.25)$$

where $\underline{G}$ is the matrix defined in Appendix A.

The creep strainrate vector can now be related to the stress vector by defining a scalar potential function ϕ which obeys the associated flow rule, i.e.,

$$\dot{\underline{\varepsilon}}_{cr} = \frac{\partial \phi}{\partial \underline{\sigma}} \tag{2.26}$$

with

$$\phi = \frac{\sigma_e \dot{\sigma}_e}{E_d} + a \frac{\sigma_e^{N+1}}{N+1} \tag{2.27}$$

where $a = (M/A_D)^N$. Combining Eqs. 2.25 to 2.27 yields the desired relationship:

$$\dot{\underline{\varepsilon}}_{cr} = \lambda \, \underline{S}^* \tag{2.28}$$

where

$$\lambda = 3/\beta \, \frac{1}{\sigma_e} \left[\frac{\dot{\sigma}_e}{E_d} + a\sigma_e^{N} \right] \tag{2.29}$$

and

$$\underline{S}^* = \underline{G} \, \underline{\sigma} \tag{2.30}$$

Note that $\underline{S}^*$ is not the conventional deviatoric stress vector. It may be thought of as a pseudo deviatoric stress vector for an anisotropic material.

The evaluation of a and E_d above requires knowledge of the effective creep strainrate $\dot{\varepsilon}_{e,cr}$ which can be expressed as:

$$\dot{\varepsilon}_{e,cr} = \beta/3 \; \dot{\underline{\varepsilon}}^T \, \underline{H} \, \dot{\underline{\varepsilon}} \tag{2.31}$$

where $\underline{H}$ is the matrix defined in Appendix A.

Given the stress vector, the pseudo deviatoric stresses may be obtained from Eq. 2.30. Then, applying Eqs. 2.25, 2.29

and 2.28 in succession leads to the creep strainrate vector. Note that if a_1 to a_6 equal one, these equations predict isotropic material behavior.

Estimation of Multiaxial Model Parameters -- Five uniaxial (compression) tests at constant strainrate are necessary to obtain the five orthotropic model parameters: a_2 to a_6. Note that (i) a_1 can be set equal to one without loss of generality, and (ii) there is experimental evidence which shows that the power-law exponent N can be considered independent of the direction of loading. For purposes of the current derivation, it is assumed that the c-axes of the sea ice crystals lie on the y-z plane and that they are aligned in the y-direction (Fig. 2.26). This implies that the x-axis represents the crystal growth direction.

Tests can be conducted in the three orthogonal directions y, x, and z respectively, and along the three 45° axes on the y-z, x-y, and z-x planes respectively. It is assumed that the uniaxial model discussed earlier refers to the y-direction. Then, let β_1 to β_5 represent the experimentally determined ratios of the maximum stresses for the latter five tests, respectively, to the maximum stress in the reference y-direction at the same strainrate. Assuming that the tests are performed at strainrates where damage (strain softening) is negligible, the orthotropic model parameters may be determined from the following equations (refer to Appendix B for derivation):

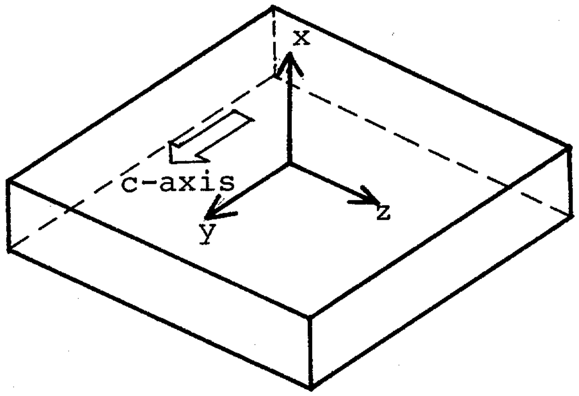

Figure 2.26 C-Axis Orientation.

$$a_2 = - \frac{\beta_1^n - \beta_2^n \, (1-\beta_1^n)}{\beta_1^n - \beta_2^n \, (1+\beta_1^n)} \tag{2.32}$$

$$a_3 = - \frac{\beta_1^n + \beta_2^n \, (1-\beta_1^n)}{\beta_1^n - \beta_2^n \, (1+\beta_1^n)} \tag{2.33}$$

$$a_4 = \frac{\beta}{6} \, [4\beta_4^{-n} - \beta_2{}^{-n}] \tag{2.34}$$

$$a_5 = \frac{\beta}{6} \, [4\beta_3^{-n} - \beta_1{}^{-n}] \tag{2.35}$$

$$a_6 = \frac{\beta}{6} \, [4\beta_5^{-n} - 1] \tag{2.36}$$

where $n=2N/(N+1)$. Typical ranges for the β_i's (identified in the previous subsection) are 2-5 for β_1, 0.50-0.95 for β_2, and 0.25-0.60 for β_3. Values for β_4 and β_5 are not generally available in the literature. Since these two parameters determine only the out-of-plane shear strains and stresses in sheet ice, they have no influence on plane strain and plane stress problems. However, the parameters will have to be obtained in the case of three-dimensional boundary value problems.

For a transversely isotropic material, i.e., isotropy in the y-z plane, $\beta_2=\beta_3=1$ and $\beta_4=\beta_5$. As a result, $a_1=a_3=1$, $a_4=a_6$, the parameters a_2 and a_5 are functions of only β_1, while a_4 depends on both β_1 and β_4. Only two uniaxial tests are required to obtain β_1 and β_4; one in the x-direction and one along the 45° axis on the x-y or z-x planes.

Frederking (1977) has conducted plane strain uniaxial compression tests on columnar-grained transversely isotropic freshwater ice. For his type A tests, strains in the z-direction are constrained to zero and stresses are applied in the y-direction. The ratio γ_z of the plane strain stress to the unconfined stress at the same strainrate is directly related to β_1 by the following equation (see Appendix C):

$$\gamma_z = [\frac{4\beta_1^{2n}}{4\beta_1^{n} - 1}]^{1/n} \tag{2.37}$$

The equation predicts γ_z to vary between 2.1 to 5.1 for experimentally observed values of β_1 ranging from 2 to 5, and N between 3 and 4. This is consistent with Frederking's experimental observations of γ_z which were close to 2 at high strainrates and to 5 at low strainrates. In the type B tests, strains in the x-direction are constrained to zero while stresses are again applied in the y-direction. In this case, the stress ratio γ_x is given by (see Appendix C):

$$\gamma_x = [1 + \frac{1}{4\beta_1^{n} - 1}]^{1/n} \tag{2.38}$$

Since β_1 is generally greater than one, γ_x will be less than approximately 1.2 for N between 3 and 4. For typical values of β_1, the predicted values of γ_x range from 1.01 to 1.06. This is consistent with Frederking's experiments which showed negligible influence of x-direction confinement on stresses.

Triaxial tests of first-year sea ice have been conducted by Richter-Menge, Cox et al. (1985) on samples obtained from horizontal cores in the plane of the ice sheet at angles of 0°, 90°, and 45° to the preferred c-axis orientation. According to the orthotropic material model, the ratio γ_t of the maximum axial stress with a confining pressure equal to τ times the axial stress to the maximum stress in the unconfined state at the same strainrate should be given by (refer to Appendix C):

$$\gamma_t = \frac{1}{1-\tau} \tag{2.39}$$

The shear stress (i.e., axial stress minus radial stress) normalized by the unconfined stress is independent of τ or confining pressure for the model and equal to one. Experimental data for this quantity is plotted versus confining pressure in Fig. 2.27, which shows that the sea ice data is only moderately pressure sensitive. Thus the use of a pressure insensitive model appears to be justified for sea ice. The figure also includes data obtained by Hausler (1981) on columnar-grained saline ice at a strainrate of $2\text{x}10^{-4}\ s^{-1}$ using a so-called "true" triaxial testing machine.

No general conclusions can be drawn as yet concerning the pressure insensitivity of sea ice since the results of Panov and Fokeev (1977) for natural and artifical sea ice seem to

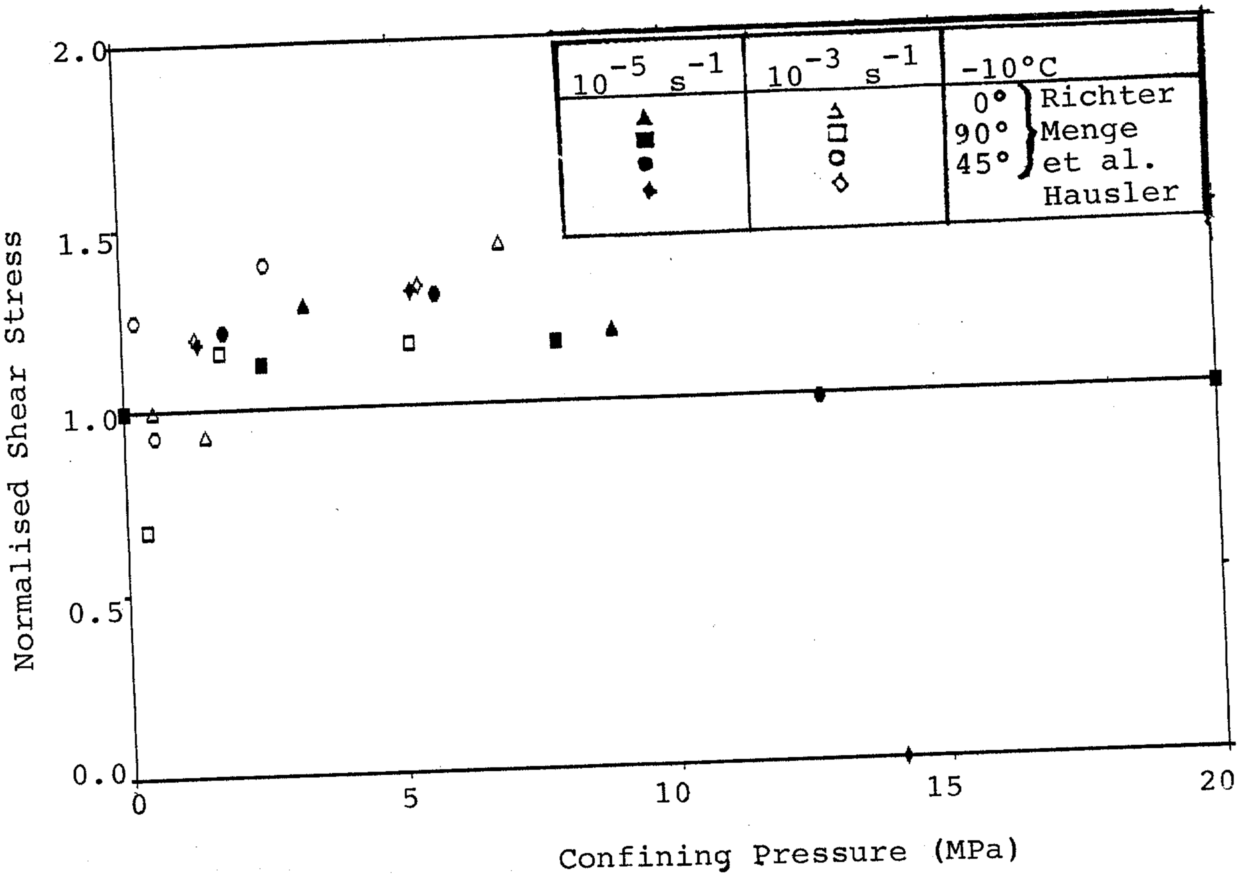

Figure 2.27 Normalised Shear Stress versus Confining Pressure.

indicate an appreciable increase in shear stress with confining pressure. However their tests were carried to the "breaking point" of ice, and as such the data represents the fracture surface and not the flow behavior of ice. On the other hand, the triaxial behavior of pure (non-saline) polycrystalline ice has been studied by Jones (1978, 1982) and Durham et al. (1982). The tests by Jones performed at strainrates of 10^{-6} to 5×10^{-3} s^{-1} indicate up to a factor of two increase in shear stress due to confining pressure. Durham et al.'s tests were conducted at temperatures of -78°C to -196°C where ice is expected to behave more as a brittle material and to very high pressures (up to 350 MPa). Very high yield stresses were recorded, and phase transitions to higher density polymorphs were reached. Both these sets of data for pure ice have limited applicability for calibration of sea ice models since no equivalence in the triaxial behavior of pure and sea (saline) ice has been established. It must be noted that the plasticity based pressure sensitive parabolic yield function of Reinicke and Ralston (1977) has been justified with the help of Frederking's (1977) data (which has been shown in this chapter to follow a pressure insensitive model very well) and that the three parameter extension of their yield function by Reinicke and Remer (1978) has been justified on the basis of Jones's triaxial data for pure polycrystalline ice.

2.6. SUMMARY

This chapter has presented a rate-sensitive damage model for describing the continuum behavior of sea ice under variable loading conditions. The model, based on a nonlinear generalization of the Maxwell differential formulation, is characterized by its ability to (a) decompose the various recoverable and irrecoverable components of strain, (b) represent continuously damaging or strain-softening material behavior in the ductile to brittle transition region, (c) capture the rate-dependent behavior of sea ice with rate-independent model parameters, and (d) describe materially anisotropic mechanical behavior. Furthermore, the model shows strong dependency of the creep and constant strainrate behavior. Calibration of the model is achieved with several independent sets of data, particularly those for first-year sea ice. The following specific conclusions can be drawn:

1. The uniaxial model developed here is described by 8 parameters. For comparable models, i.e., those of Sinha and Michel, the number of parameters is 7 and 9 respectively. It must be recognized that Sinha's model does not capture material damage with strain-softening, while calibration of Michel's model with experimental data has been very limited.

2. All parameters of the proposed model, i.e., 8 for the uniaxial model and 5 for the orthotropic generalization, can be determined from conventional tests conducted on ice. The

experimental data base is generally adequate to determine the model parameters. In particular, normalization of the uniaxial strength data for salinity and temperature is a useful way of including test results for pure polycrystalline ice in model calibration.

3. Material damage that can be described by the continuum model proposed here is significant in the strainrate range of $2x10^{-4}$ s^{-1} to 10^{-2} s^{-1}. At higher strainrates the presence of macrocracks precludes a solely continuum description of ice behavior.

4. According to the proposed model, an ideal creep test does not lead to primary creep strains. However if the finite rise time required to reach the nominal stress in a creep test is taken into account, primary creep strains are simulated by the model. Experimental evidence appears to support this conclusion.

5. The pressure-insensitive orthotropic model proposed here predicts very well the plane strain uniaxial compression tests conducted by Frederking. Further, experimental data of Richter-Menge et al. on first-year sea ice and that of Hausler on saline ice indicate that sea ice is only moderately pressure sensitive in comparison with pure ploycrystalline ice which is highly pressure-sensitive.

Additional research is needed to resolve several questions, including (a) the presence or lack thereof of primary creep strains in ideal creep tests, (b) the possible pressure sensitivity of the damage parameter, (c) the adequacy of the incremental damage accumulation model based on Miner's rule particularly for variable loading histories, (d) the generation of hysteresis loops during unloading/reloading and cyclic loading, (e) the value of peak stress at failure in stress-strain curves obtained from tests conducted at low stressrates (i.e., lower than 0.1 MPa s^{-1}), (f) the extent of stress relaxation in sea ice, and (g) the equivalence, if any, in the triaxial behavior of pure and sea ice. Both experimental and theoretical research is very much needed to better characterize the multiaxial behavior of sea ice particularly under cyclic loading.

CHAPTER THREE

YIELDING AND FRACTURE MODELING OF SEA ICE BEHAVIOR

3.1 INTRODUCTION

Field observations of sea ice indentation on offshore structures in the Arctic show that fracture processes are a major factor in ice-structure interaction.

In most applications ice behaves as a material exhibiting both continuum deformation and cracking activity. Microcracking activity can be effectively idealized as continuum behavior and represented by models describing multiaxial flow by creep with appropriate modifications to account for damage due to microcracking. This damage leads to strain-softening in constant strainrate tests in compression and to tertiary creep strains in compressive creep tests. On the other hand, macrocracking activity leading to failure of the material at macroscale is a separate behavioral mechanism. A constitutive model that captures both the mechanisms of multiaxial flow by creep and ultimate failure by fracture or macrocracking is necessary to simulate the deformation process in ice. Previous modeling work directly relevant to the development of such a constitutive model is limited since most investigators have treated ice as either a plastic or a viscoelastic material under multiaxial states of stress.

These models do not distinguish the mechanisms of flow and fracture.

A rate-sensitive model in stress-strain domain for describing the macroscale yielding and fracture behavior of sea ice is dicussed in this chapter. The model, unified with a rate-sensitive damage model developed in the previous chapter for the continuum behavior of sea ice, is characterized by its ability to (a) predict first crack occurrence with a rate-dependent limiting tensile strain criterion, (b) represent fracture under multiaxial states of stress with a Drucker-Prager failure surface, and (c) distinguish the mechanisms of multiaxial flow by creep and ultimate failure by macrocracking leading to yielding or fracture. Calibration of the model is achieved with the limited existing experimental data base.

3.2 PREDICTION OF FIRST CRACK OCCURRENCE

The occurrence of first cracks in ice under compressive creep conditions in the laboratory has been studied by Gold (1972). Based on the assumption that grain boundary shear or sliding can be associated with a delayed elastic effect, Sinha (1982) postulated that delayed elasticity can be linked to crack nucleation. With the help of his mathematical model for delayed elasticity and the experimental data of Gold, he showed that for S-2 ice of grain size 4.5 mm cracks begin to form if the delayed elastic strain exceeds 1.04×10^{-4}. The time to formation of first crack based on Gold's laboratory experiments and Sinha's delayed elastic strain criterion is plotted in Fig. 3.1.

A suddenly applied constant load case, i.e., creep, is not representative of loading conditions on offshore structures. A constant strainrate or stress-rate condition may be more realistic. Sanderson and Child (1984) consider the prediction of first crack occurrence under constant stressrate loading conditions using the principle of superposition, which Sinha (1983b) has shown to be valid for "icelike" materials under monotonically increasing stress, and the delayed elastic strain criterion. They predict that first cracks in pure S-2 ice at typical stress-rates of 0.010-0.035 kPa s^{-1} should occur at a stress of 0.6-0.7 MPa and at extreme stress-rates of 1-5 kPa s^{-1}, may occur at 1.3-1.8 MPa (Figs. 3.2 and 3.3). For sea ice, the stress levels are corrected by altering the net section stress due to brine volume based on the theory of Frankenstein and Garner (1967). The corresponding stresses are 0.4 MPa and 0.8-1.1 MPa (Fig. 3.4).

In this chapter, a rate-dependent limiting tensile strain criterion is developed to predict first crack occurrence in ice. This development recognizes that fracture in ice manifests itself in terms of tensile cracking and crushing in compression. Experimental evidence shows that ice is weaker in tension than in compression and further that fracture may

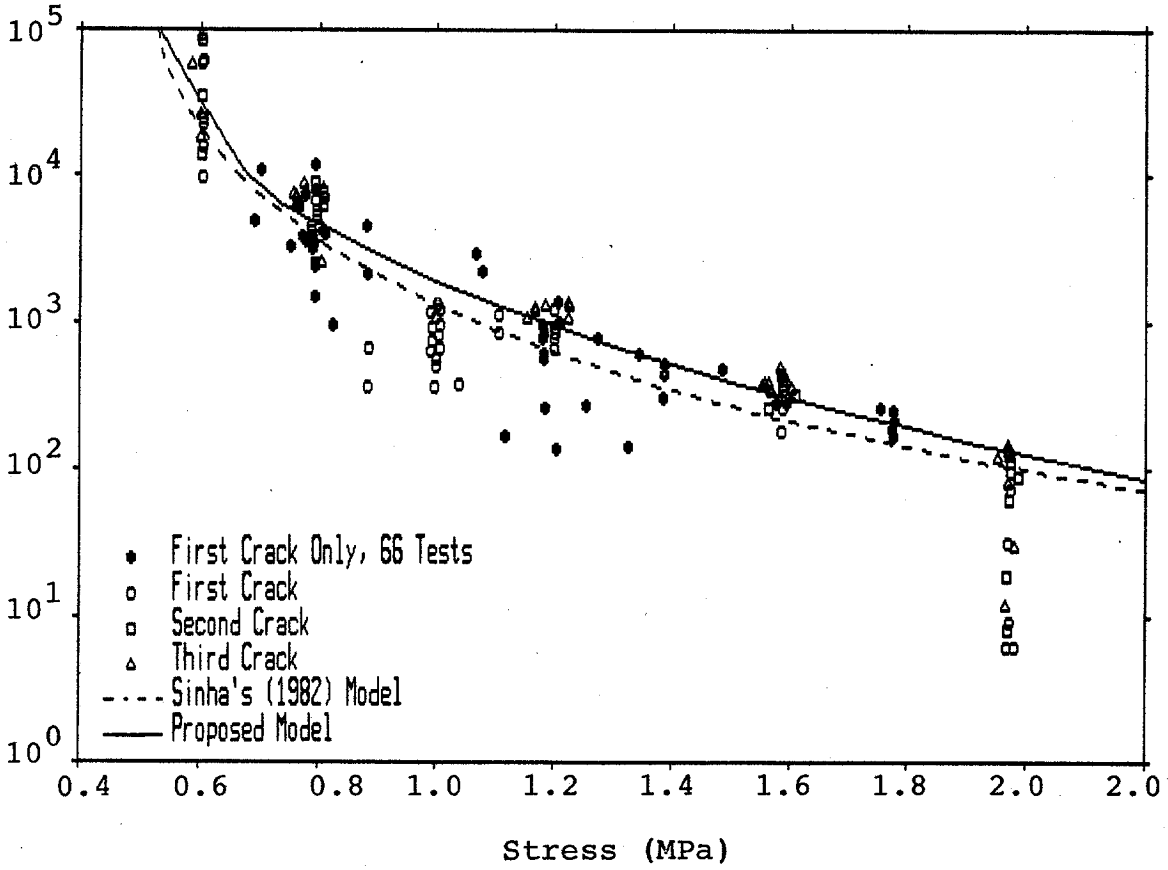

Figure 3.1 Formation of First Cracks During Uniaxial Compressive Creep Tests.

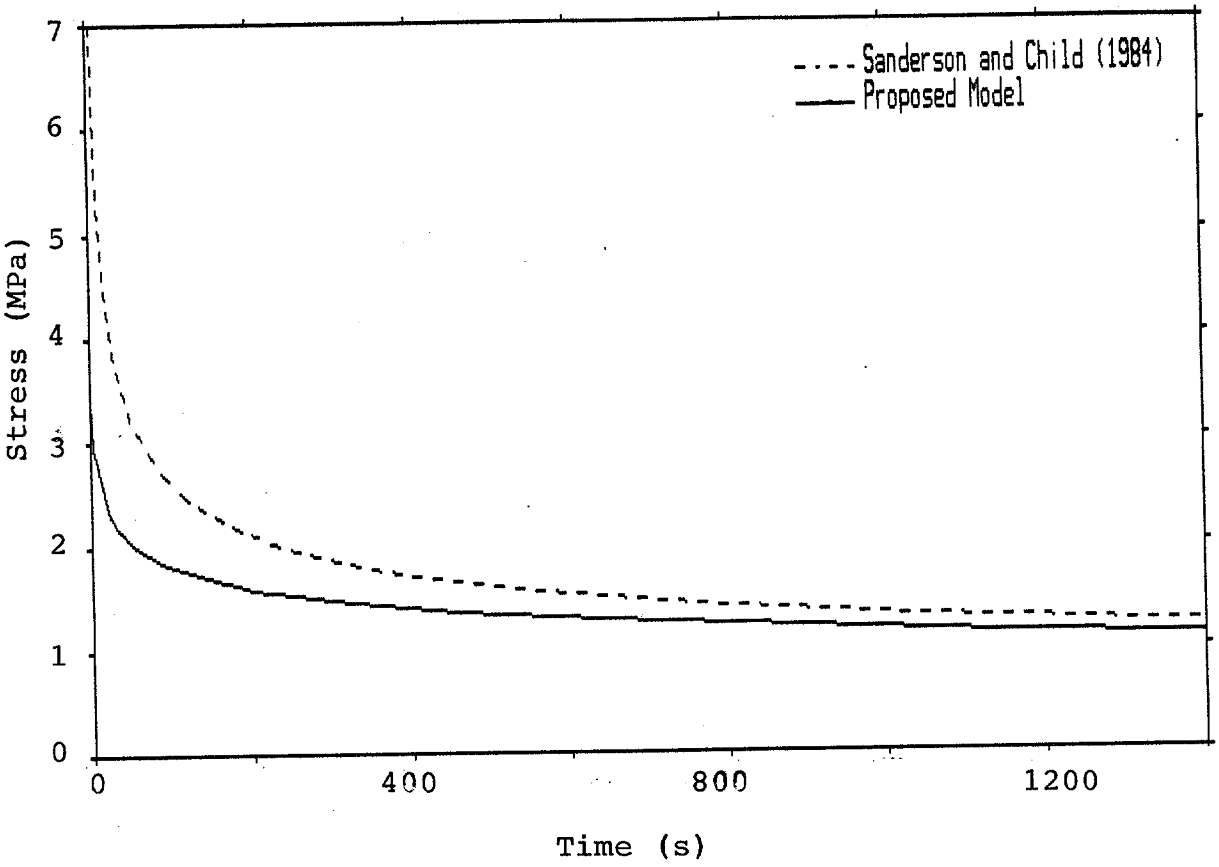

Figure 3.2 Formation of First Cracks Under Constant Stress-Rate Tests.

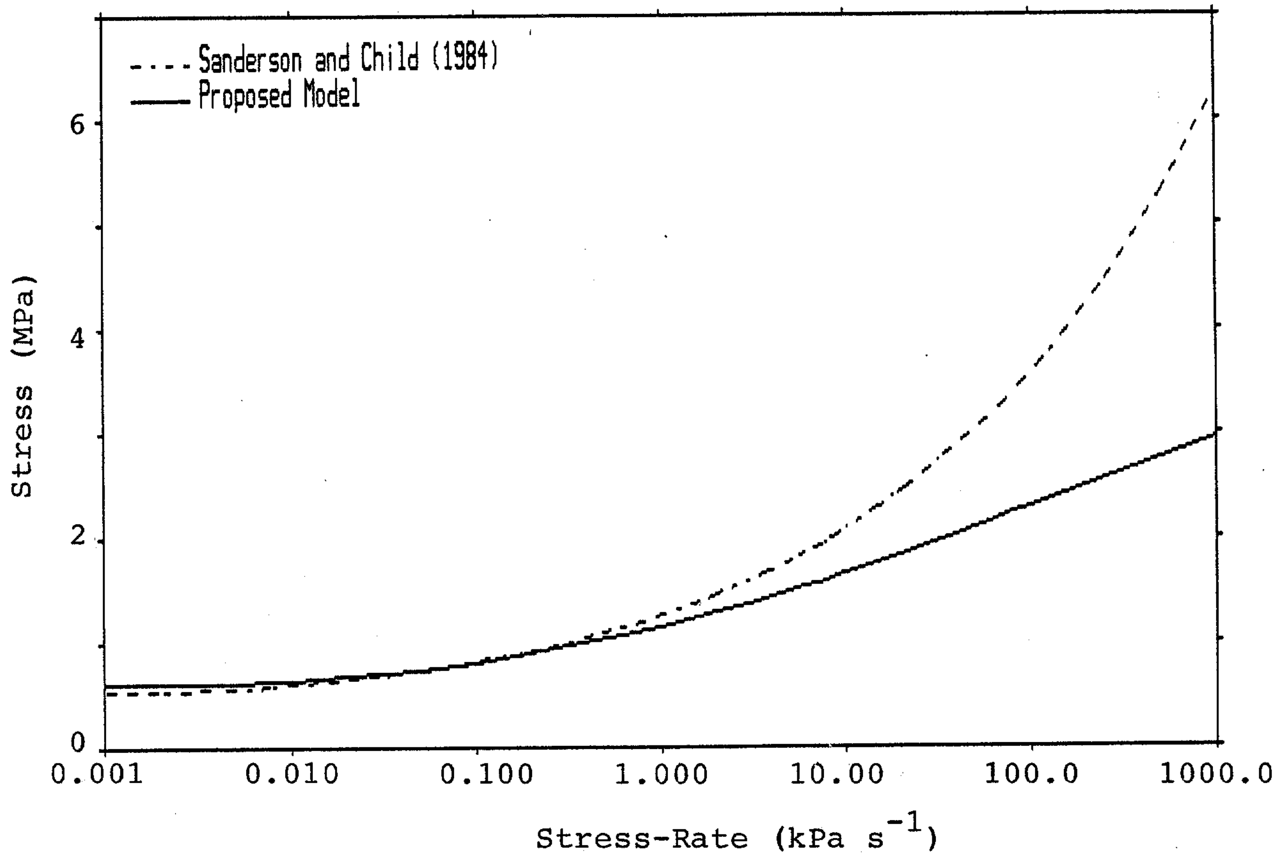

Figure 3.3 Stress at which First Cracks Appear for Pure Ice Under Constant Stress-Rate Tests.

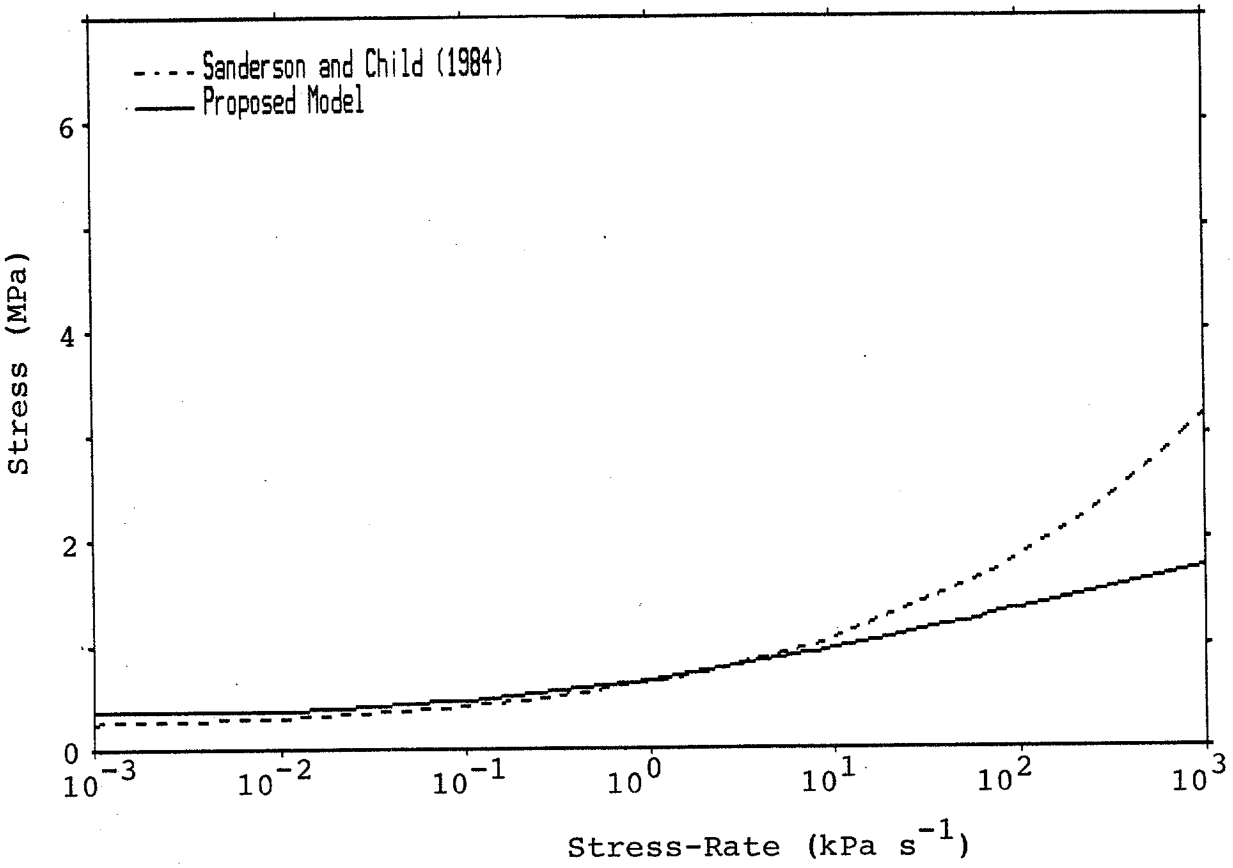

Figure 3.4 Stress at which First Cracks Appear for Sea Ice Under Constant Stress-Rate Tests.

occur in tension even though in compression the material behaves as a continuum.

Schulson (1979, 1984a, 1984c) and Currier and Schulson (1982) have studied the brittle to ductile transition in polycrystalline ice under tension. Schulson proposes that the tensile behavior of ice can be considered in terms of a stress for crack nucleation and a stress for crack propagation. Based on experimental data obtained by Hawkes and Mellor (1972) and by him, he concludes that the tensile strength of coarsely grained aggregates (greater than 1.5 mm) is controlled by crack nucleation while that of more finely grained material appears to be controlled by crack propagation. In the former cases, which is more appropiate for columnar sea ice, the tensile strength actually represents fracture.

Schulson (1984b, personal communication) has more recently been investigating the brittle to ductile transition in polycrystalline ice under compression. His theory for tensile behavior has been extended to account for the rate-dependent behavior of the compressive crack nucleation strength. Further his model tends to indicate that the ratio of crack propagation strengths in compression and tension to be nearly 8, the number for Griffith materials.

The strength versus strainrate data of Ashby and Cooksley-Hallam for pure ice contained in Palmer et al. (1982)

is shown in Fig. 3.5. This figure shows that the ratio of compressive to tensile strength is about 3 when crack nucleation governs both failures, and that fracture in tension occurs at much smaller strainrates than that in compression. This data, which appears to be more appropriate for typically encountered sea ice, has been used in the model development here.

The stress-strain-strainrate behavior in uniaxial tension prior to fracture is considered to be identical to that under uniaxial compression. Hawkes and Mellor (1972) justify this assumption for creep data. For strainrates less than $5\text{x}10^{-8}\ \text{s}^{-1}$ (i.e., tension 'strength' of 0.48 MPa for pure ice and 0.28 MPa for sea ice), ice does not fracture in tension. For high strainrates, tensile cracking occurs at a constant stress, σ_{tm}, of 2.0 MPa. For strainrates greater than $5\text{x}10^{-8}\ \text{s}^{-1}$, the tensile fracture strength of ice is modelled as:

$$\frac{1}{\sigma_{tf}} = \frac{1}{\sigma_{tm}} + \frac{1}{B\ \dot{\varepsilon}^{\frac{1}{N}}} \qquad (3.1)$$

where $B=176$ MPa $s^{1/N}$ and is obtained from Eq. 3.1 with the known value of the tensile fracture stress at the ductile to brittle transition strainrate. The resulting model shown in Fig. 3.6 very closely resembles Fig. 3.5. The stress-strain behavior predicted by the model is shown in Fig. 3.7 and the

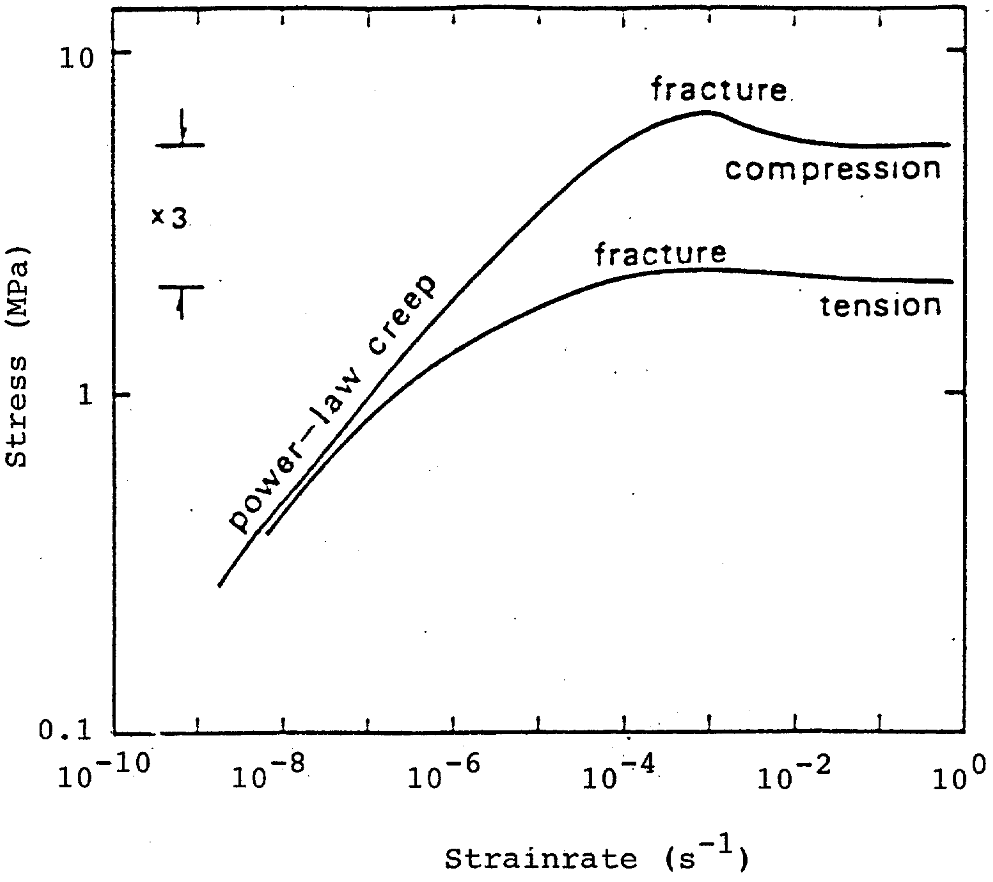

Figure 3.5 Strength of Pure Ice In Uniaxial Compression and Tension at -10°C (Palmer et al., 1982)

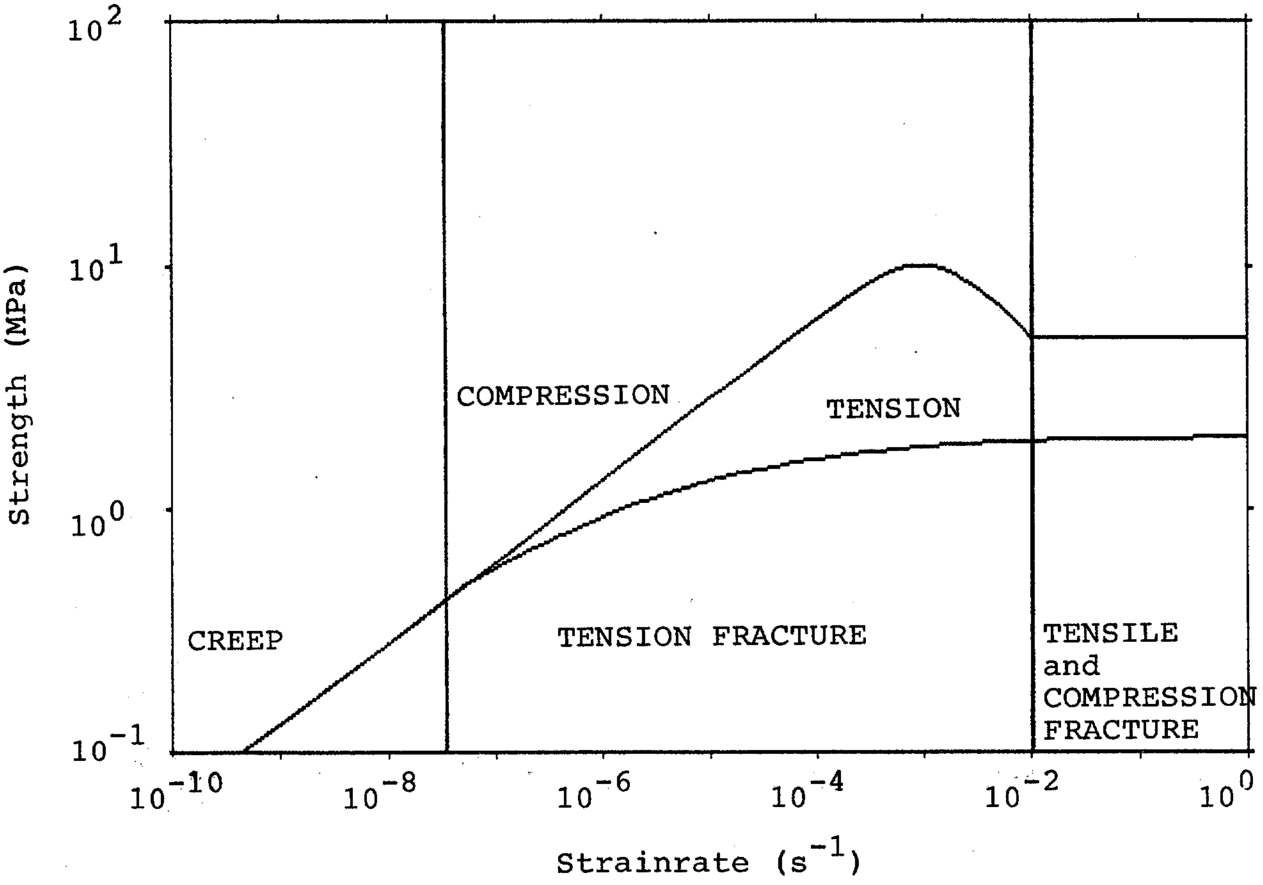

Figure 3.6 Strength of Columnar Ice.

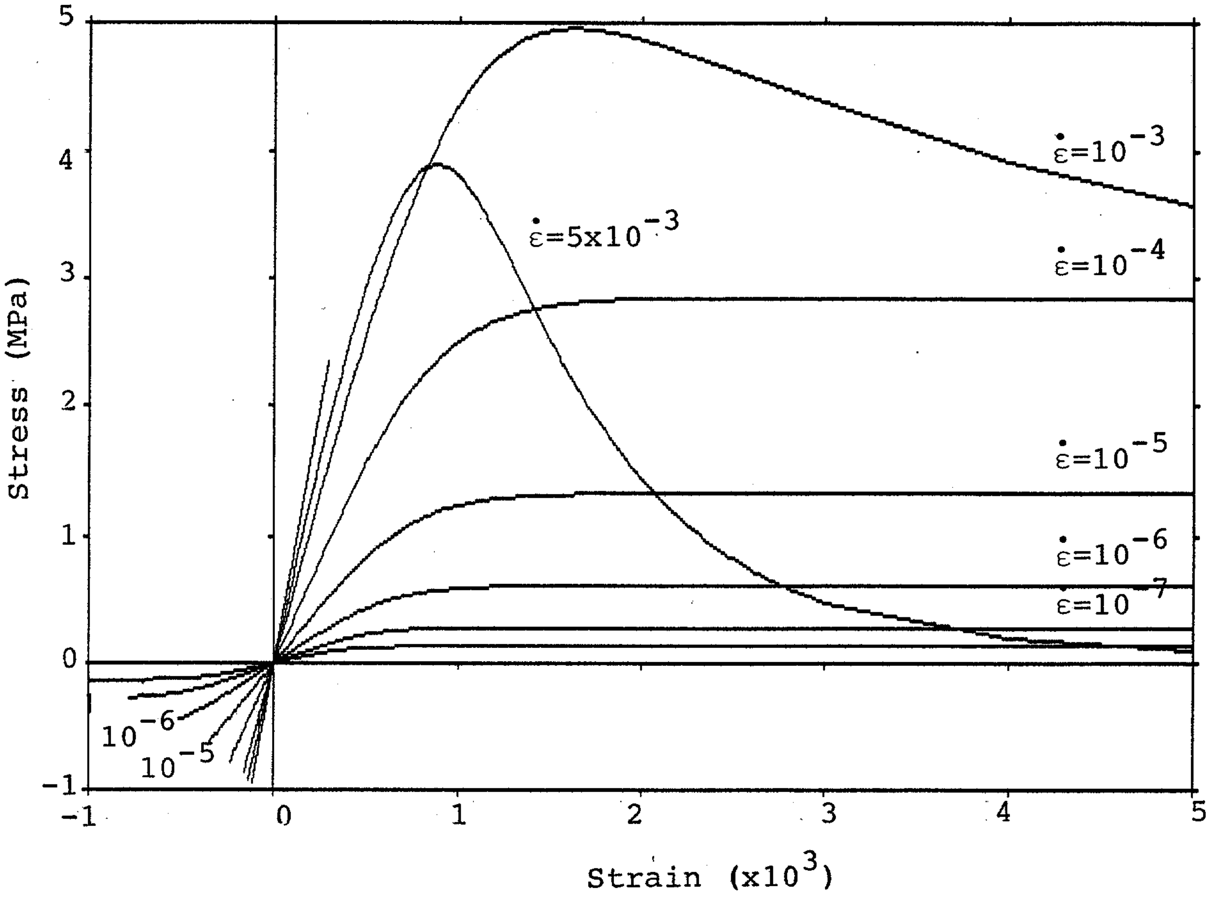

Figure 3.7 Stress-Strain Plots Under Constant Strainrate for Proposed Model with Fracture.

tensile fracture strain is plotted as a function of strainrate in Fig. 3.8.

The prediction of first crack occurrence under uniaxial compressive creep loading is based on the hypothesis that the crack nucleates due to the lateral tensile strain resulting from the Poisson effect of elasticity and the incompressibility condition of flow, i.e.,

$$\varepsilon_t = \nu\, \varepsilon_e + (\varepsilon_c - \varepsilon_e)/2 \qquad (3.2)$$

and

$$\dot{\varepsilon}_t = \dot{\varepsilon}_c/2 \qquad (3.3)$$

where ν is the Poisson ratio, the subscripts, t and c, refer respectively to the total tensile and compressive strain and strainrates, and e refers to the instantaneous elastic strain in compression. The first crack is postulated to occur when the lateral tensile strain equals the strain for tensile fracture at the instantaneous strainrate as given in Fig. 3.8. This is the rate-dependent limiting tensile strain criterion for first crack occurrence or nucleation.

Figure 3.1 contains the prediction of first cracks for creep tests using the model postulated here. Comparison with the experimental data of Gold shows that the proposed criterion captures the overall trend of the data very well. In particular, the time to first crack asymptotically approaches infinity as the compressive stress reduces to

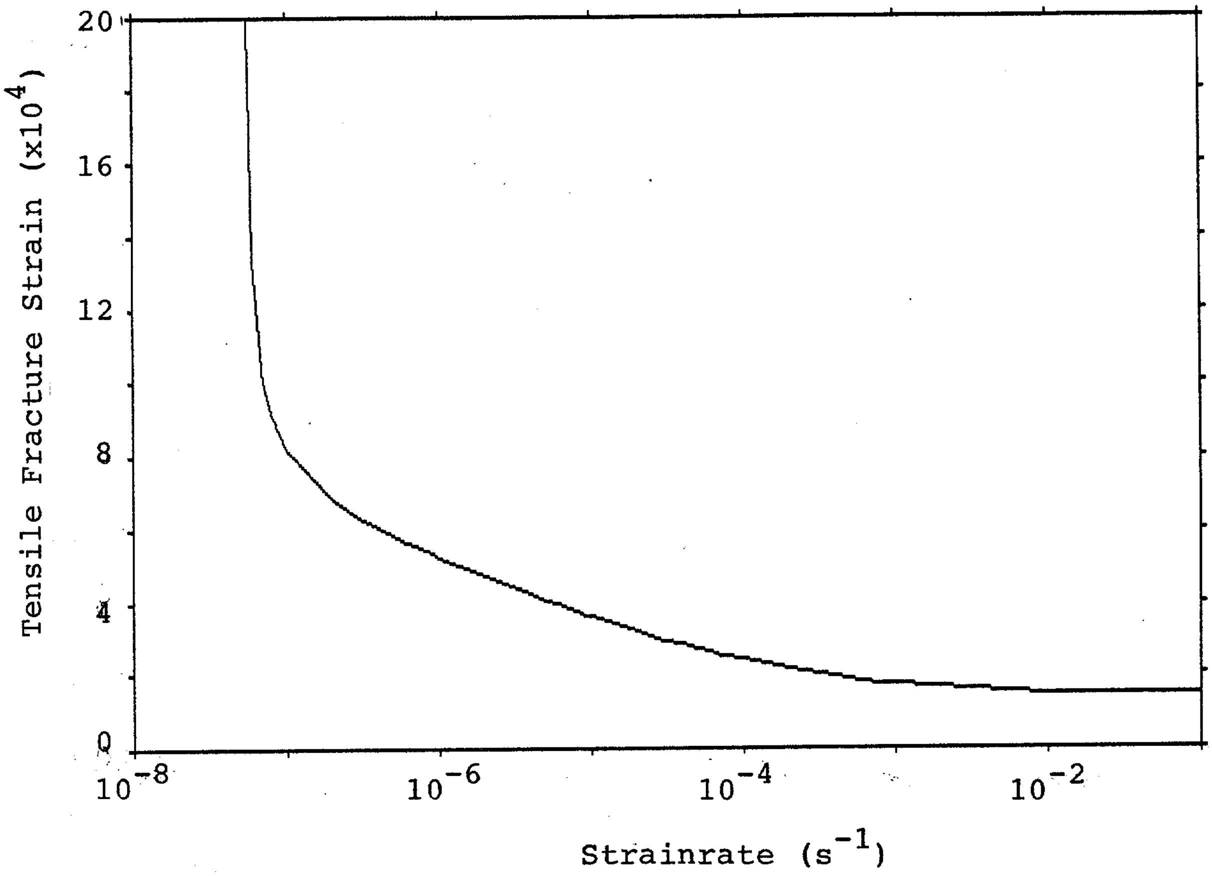

Figure 3.8 Tensile Fracture Strain Under Different Strainrate Loading Conditions (Sea Ice).

0.48 MPa. The choice of stress-strainrate at which ice transits from ductile to fracture behavior in tension , i.e., 0.48 MPa and $5x10^{-8}$ s^{-1}, determines this asymptote. Data scatter may be due to several reasons, including model uncertainty. However, two sources stand out. One, the finite rise time of about two seconds required for the applied load to reach the constant stress state for creep, and two, uncertainties associated with the identification/definition of "first" crack. The limiting tensile strain criterion compares well with the delayed elastic strain criterion of Sinha for the range of stresses considered in the figure. However, at higher stresses the two criteria are in significant disagreement (Fig. 3.9). At the compressive fracture stress of 5.0 MPa, the proposed model predicts almost zero time to first crack since no creep can occur under this load.

Figure 3.2 contains the prediction of first cracks under constant stress-rate conditions. The agreement between Sanderson and Child's analysis based on the delayed elastic strain criterion and the present criterion is very good in general. However, the model predictions differ considerably at high stressrates. At infinite stress-rate, the stress at first crack is limited by the compressive fracture stress of 5.0 MPa. This is predicted by the postulated fracture criterion. Figures 3.3 and 3.4 show that for typical stress-rates the stress at first crack is virtually unchanged

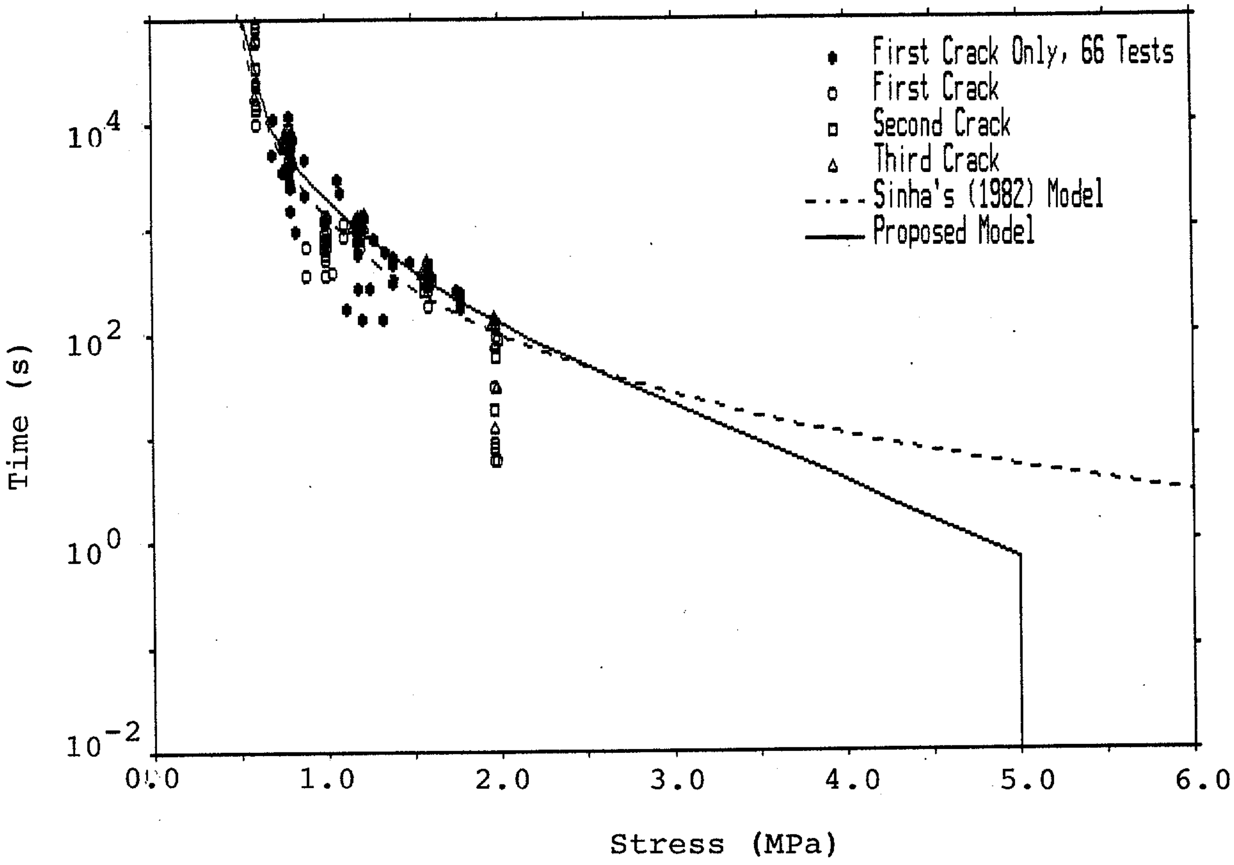

Figure 3.9 Formation of First Cracks During Uniaxial Compressive Creep Tests.

for pure ice, 0.64-0.71 MPa, and somewhat higher for sea ice, 0.37-0.41 MPa. For extreme stress-rates, the stress is lower for pure ice but virtually unchanged for sea ice, i.e., 1.1-1.5 MPa and 0.6-0.9 MPa, respectively. The findings for pure and sea ice differ since the brine volume correction of strength for sea ice affects the tensile fracture strain in a complex manner. Strictly, the model parameters used in this work are appropriate only for sea ice even though stresses have been normalized for brine volume, since the effect of brine on the strains is not taken into account. For example, the strain at peak stress for constant strainrate tests of pure ice is about 1% while that for sea ice is about 0.1%.

3.3 MULTIAXIAL MODEL FORMULATION

In uniaxial tension, the stress to nucleate a crack, i.e., the yield stress, is the fracture stress, and its variation with strainrate has been mathematically modelled in Eq. 3.1. In uniaxial compression, ice behaves as a continuum up to a strainrate of 10^{-2} s^{-1}. However, cracks do form as a result of lateral tensile strains. The compressive stress at which the first crack nucleates is defined to be the "yield" stress in compression σ_{cn}. Once this stress is reached, the material continues to sustain compressive load but loses its ability to carry tensile loads in the transverse direction if applied. This is a realistic assumption and is often used in modeling concrete behavior (ASCE, 1982). Thus, the compressive "yield" stress at which the first crack nucleates defines a second point on the "yield" or "fracture" surface. For strainrates greater than 10^{-2} s^{-1} in compression, ice fractures at a normalized stress, σ_{cm}, of 5 MPa. Figure 3.10 shows both the tensile fracture strength and the compressive "yield" strength as a function of strainrate. The latter may be expressed mathematically as:

$$\frac{1}{\sigma_{cn}^{2}} = \frac{1}{\sigma_{cm}^{2}} + \frac{1}{\left(\frac{A}{M}\,\dot{\varepsilon}^{\frac{1}{N}}\right)^{2}} \qquad (3.4)$$

where all the parameters have been previously defined.

A rate-sensitive and isotropic Drucker-Prager failure surface is used to describe the yield/fracture behavior of ice. The failure surface f may be expressed as:

$$f(\underline{\sigma}) = p\, I_1 + \sqrt{J_2} - k \qquad (3.5)$$

where p and k are constants, and I_1, is the first invariant of stress given by:

$$I_1 = \sigma_{xx} + \sigma_{yy} + \sigma_{zz} \qquad (3.6)$$

and J_2 is the second invariant of the deviatoric stress given by:

$$J_2=[(\sigma_{xx}-\sigma_{yy})^2+(\sigma_{yy}-\sigma_{zz})^2+(\sigma_{zz}-\sigma_{xx})^2]/6+\sigma_{xy}^2+\sigma_{yz}^2+\sigma_{zx}^2 \qquad (3.7)$$

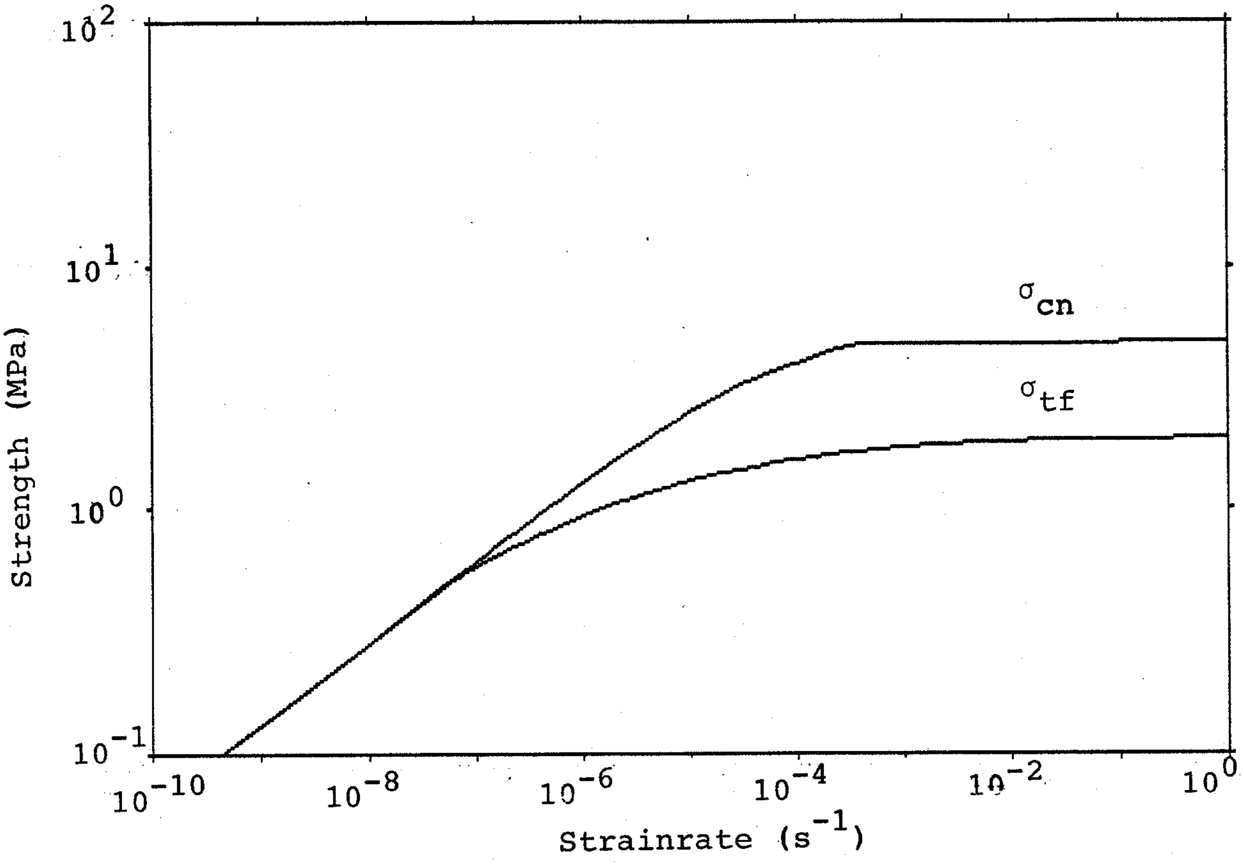

Figure 3.10 Tensile Fracture Strength and Compressive Strength for Crack Nucleation.

The constants p and k for the Drucker-Prager model at a given effective strainrate can be derived from two uniaxial tests at the same constant strainrate value, one in tension and the other in compression. The resulting equations are:

$$p = \frac{1}{\sqrt{3}} \; \frac{\left(\frac{\sigma_{cn}}{\sigma_{tf}}\right) + 1}{\left(\frac{\sigma_{cn}}{\sigma_{tf}}\right) - 1} \tag{3.7}$$

and

$$k = \sigma_{cn} \, (p - 1/\sqrt{3}) \quad \text{or} \quad \sigma_{tf} \, (p + 1/\sqrt{3}) \tag{3.8}$$

Both p and k are functions of strainrate as shown in Fig. 3.11. Notice that for strainrate less than the ductile to brittle transition strainrate in tension, p equals zero and k is proportional to the effective stress for the continuum flow. The Drucker-Prager surface reduces to the von Mises flow surface in this case. Experimental data to develop an anisotropic model for the failure surface is not available at this time.

Figure 3.12 shows the progressive creep flow surfaces under plane stress conditions at a specified effective strainrate below the transition strainrate in tension. The limiting flow surface corresponds to the maximum stresses that can be reached under the given loading rate. At very high strainrates, i.e., above 10^{-2} s^{-1}, no flow can occur.

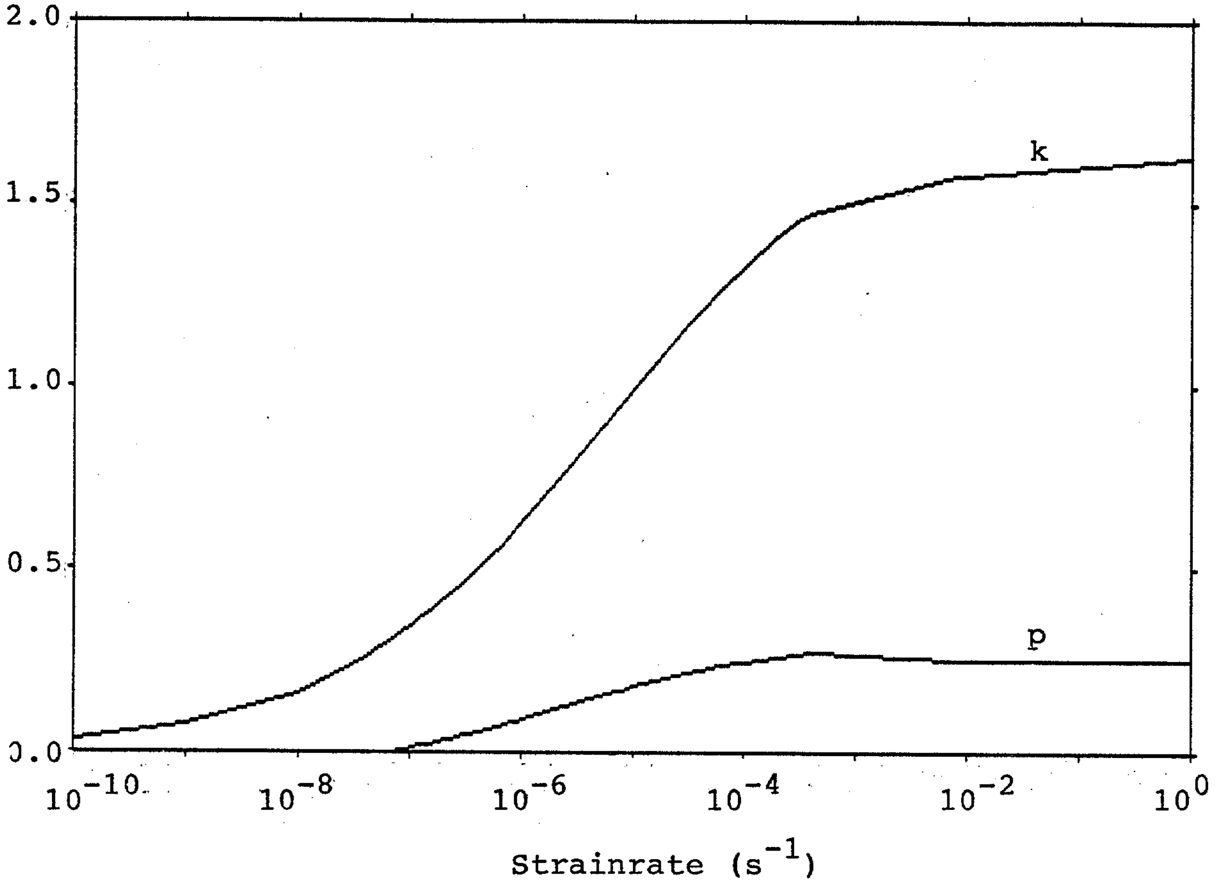

Figure 3.11 Variation of p and k with Strainrates.

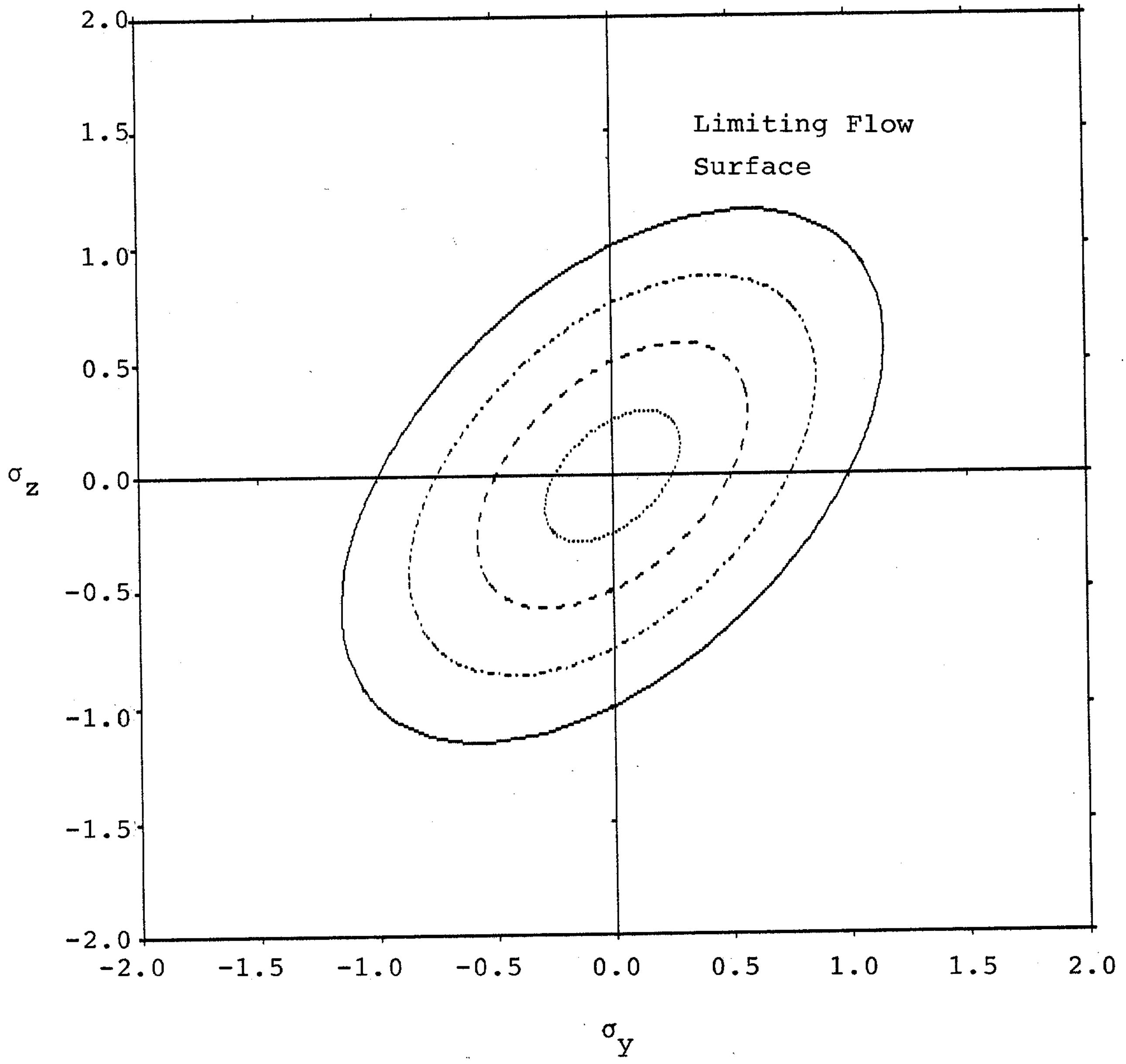

Figure 3.12 Limiting Flow Surface Under Plane Stress Condition at Low Strainrate.

Instantaneous elastic deformation is followed by fracture under all states of stress and Fig. 3.13 shows the Drucker-Prager failure surface corresponding to this condition. At intermediate strainrates, the limiting flow surface and the yield/fracture surface overlap as shown in Fig. 3.14. In any of the quadrants where a tensile state of stress exists, if the fracture surface is inside the limiting flow surface then it defines the maximum attainable stress. The tensile fracture is assumed to occur in the direction of the (largest) tensile stress. When the state of stress is completely compressive, the limiting flow surface is attainable. However, if the "yield" surface is crossed, a crack is assumed to nucleate in the direction of the smallest compressive stress and no tensile stress can be sustained by the material in that direction if applied at a later time.

The tensile strength of bubbly polycrystalline ice under triaxial stresses has been investigated by Haynes (1973). The mean values of his tensile strength, obtained at an average strainrate of approximately 10^{-5} s^{-1}, as well as many classical failure envelopes for brittle materials are shown in Fig. 3.15. None of the theories seem to explain the data very well. At the same strainrate, the model developed here indicates a ratio of σ_{cn} to σ_{tf} equal to approximately 1.7. This appears to provide the best prediction of the measured data.

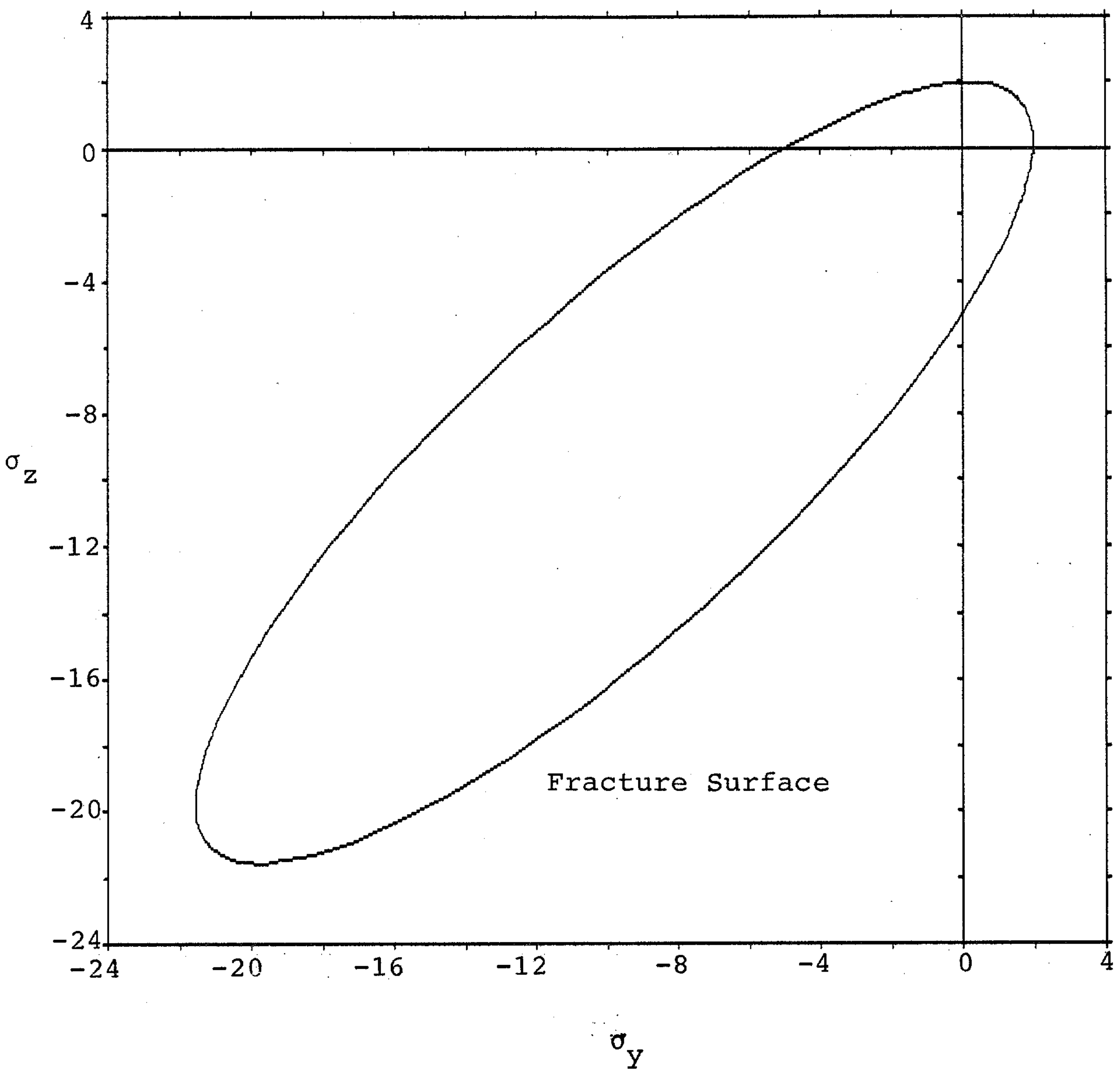

Figure 3.13 Fracture Surface Under Plane Stress Condition at High Strainrate.

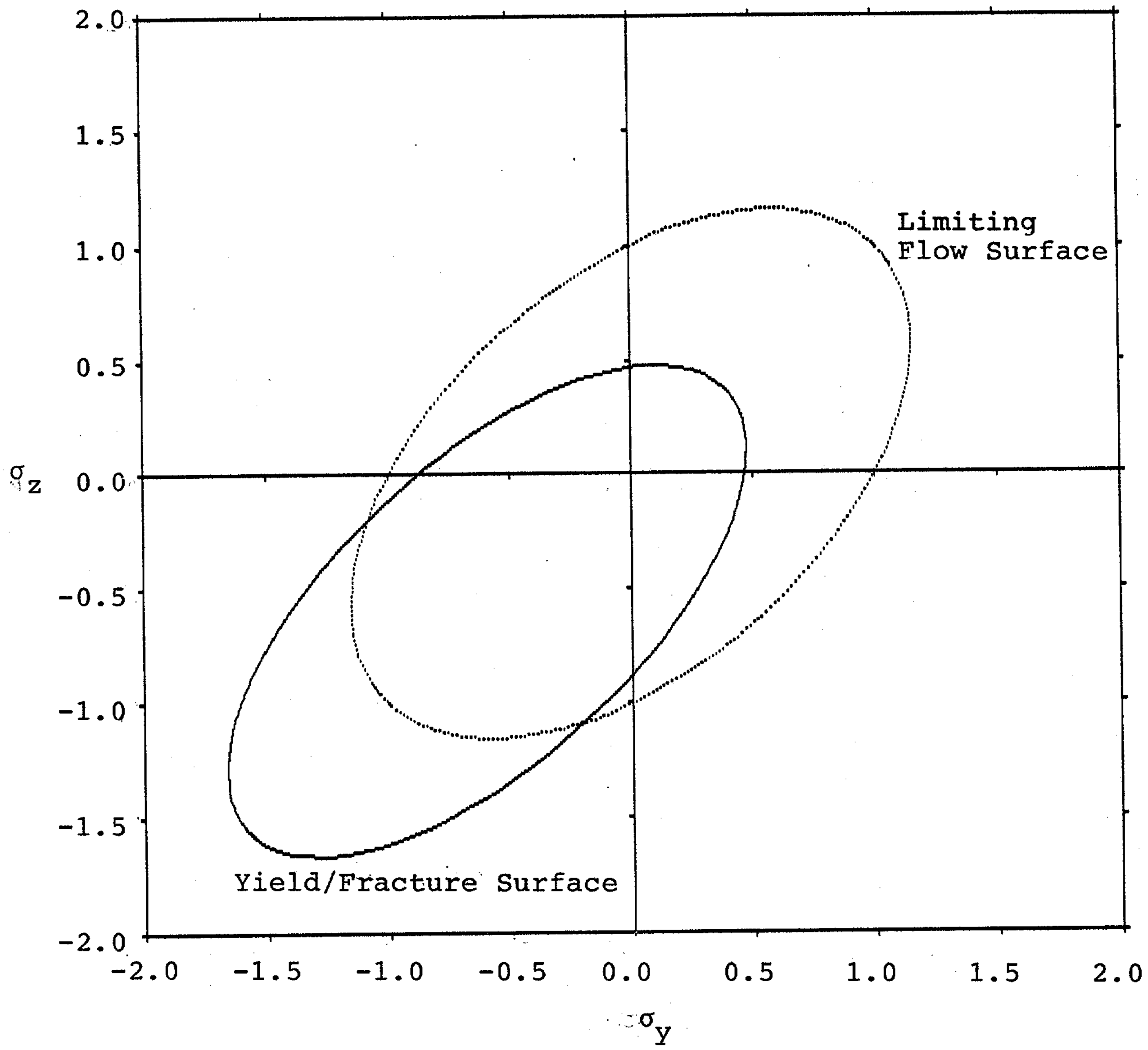

Figure 3.14 Interaction of the Fracture Surface with the Limiting Flow Surface Under Plane Stress Condition, Normalized by the Peak Compressive Stress.

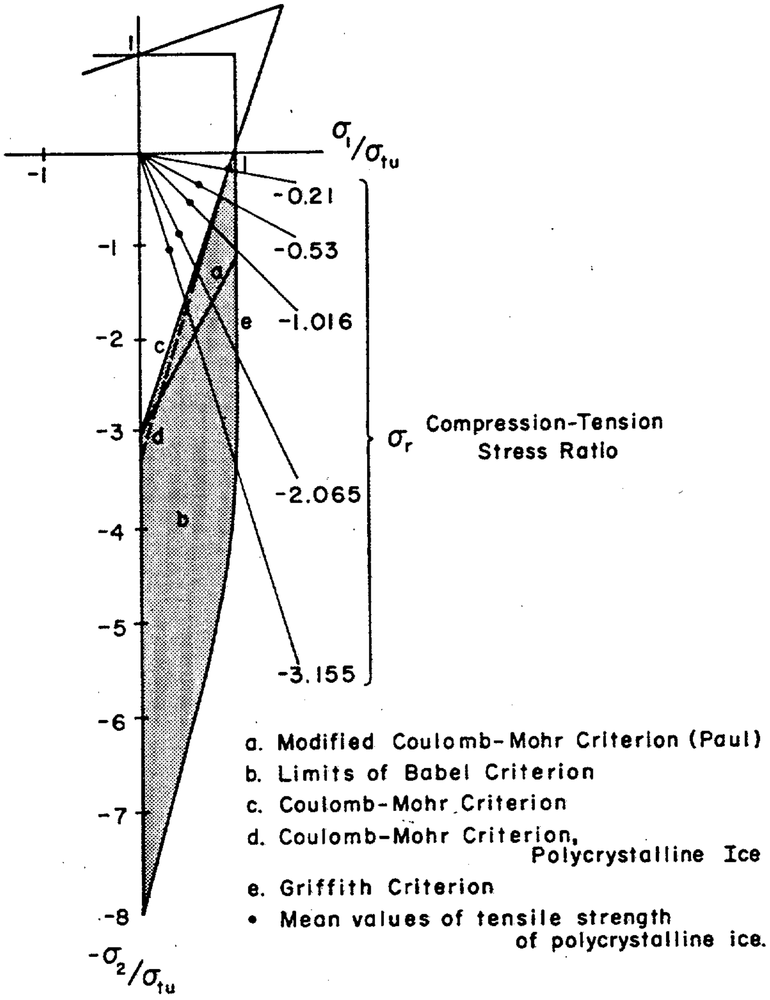

Figure 3.15 Biaxial Failure Envelopes for Brittle Materials (Haynes, 1973).

3.4 SUMMARY

A rate-sensitive model in stress-strain domain for describing the macroscale yielding and fracture behavior of sea ice is dicussed in this chapter. The model, unified with a rate-sensitive damage model developed in the previous chapter for the continuum behavior of sea ice, is characterized by its ability to (a) predict first crack occurrence with a rate-dependent limiting tensile strain criterion, (b) represent fracture under multiaxial states of stress with a Drucker-Prager failure surface, and (c) distinguish the mechanisms of multiaxial flow by creep and ultimate failure by macrocracking leading to yielding or fracture. Calibration of the model is achieved with the limited existing experimental data base. The following specific conclusions can be drawn:

1. The prediction of first crack nucleation under uniaxial compressive creep conditions using a rate-dependent limiting tensile strain criterion for the lateral tensile strains arising from Poisson's effect and incompressibility of flow compares very well with the experimental data of Gold.

2. The time to first crack occurrence tends to approach zero as the uniaxial compressive stress approaches a value corresponding to fracture, i.e., 5.0 MPa. At these higher stresses, the delayed elastic strain criterion of Sinha continues to predict longer first crack nucleation times.

3. The prediction of first crack occurrence under constant stress-rate conditions using the rate-dependent

limiting tensile strain criterion agrees very well at low to intermediate stressrates with the analysis of Sanderson and Child based on the delayed elastic strain criterion. At high stressrates, the proposed model predicts a significantly lower stress for nucleation of the crack.

4. A rate-sensitive and isotropic Drucker-Prager failure surface is used to describe yield of ice under compressive states of stress and fracture of ice whenever a tensile stress is present. The constants of the model are derived from two uniaxial tests, one in tension and the other in compression. In the latter case, the compressive stress at which the first crack nucleates using the rate-dependent limiting tensile strain criterion defines the "yield" point.

5. The ratio of the yield stress in uniaxial compression to the fracture stress in uniaxial tension obtained from the Drucker-Prager formulation appears to provide the best match to data from the tensile triaxial tests of Haynes.

Additional research is needed to address the following concerns: (a) the influence of temperature on the fracture strength in tension and compression and the strain and strainrate at which it occurs, (b) experimental data under biaxial and triaxial loading conditions to better define the failure surface defining yield in compression and fracture in tension, and its use in the development of an orthotropic failure surface, and (c) the equivalence, if any, in the strains and triaxial behavior of pure polycrystalline ice and sea ice.

CHAPTER FOUR

APPROXIMATE ANALYTICAL SOLUTION FOR INDENTATION

4.1 INTRODUCTION

Two levels of ice loading are typically considered in the design of drilling and production platforms for the Arctic. Global ice pressures govern the overall structural geometry and dimensions as well as the foundation design, while local pressures are likely to dictate wall thicknesses and local framing, and may well govern structural cost. Most of the emphasis on ice force research has been on predicting global forces. Only during recent years, as the focus changed from overall feasibility to preliminary and detailed design, has the importance of local pressures emerged. Peak local pressures as high as three times the average global pressure have been suggested. It is widely recognized that uncertainties exist in ice load prediction models in use today and that in some cases design loads may be overestimated by an order of magnitude.

Uncertainties in existing ice load models arise primarily from five sources: (i) incomplete modeling of the mechanical behavior of sea ice, including temperature and fracture effects, (ii) empiricism in existing theoretical models resulting from the use of approximate analysis methods,

(iii) inadequate modeling of the contact forces at the ice-structure interface, (iv) neglecting the effect of scale/size on material strength, and (v) not accounting for the finiteness of environmental and other forces driving the ice features. Both approximate analytical methods and more rigorous numerical models based on the finite and boundary element methods of analysis can be used to study ice-structure interaction at full scale with realistic models for material and interface behavior.

The interaction of an ice sheet with a vertically faced (and usually rigid) indenter is an important loading condition for cylindrical structures and for conical structures with grounded rubble pile or accreted ice foot. In general, this indentation phenomenon is characterized by the simultaneous occurrence of viscous (rate-dependent) and fracture behavior. In particular, it is assumed that the structure is frozen into an ice sheet when environmental forces start driving the sheet. Stresses keep building up in the ice till such time a macrocrack forms to relieve the built-up stresses. The ice pressure on the indenter will be greatest just prior to macrocrack formation or "break-out", and it is the prediction of this pressure that is studied here. The modeling assumes that prior to break-out ice deforms primarily in the creeping mode.

A study of ice indentation in the creeping mode is important for two reasons: (a) creep is the predominant mode of deformation for artificial islands in the Arctic nearshore region during "breakout" and/or steady indentation conditions occurring in the winter, and (b) stresses, strains, and strainrates within the continuum resulting from creep are necessary to predict the initiation and possibly even the propagation of cracks when viscous effects influence fracture.

Approximate methods of analysis are employed first to address the problem before taking recourse to a more complete analysis based on the finite and/or boundary element methods because: (1) approximate methods of analysis are several times quicker to implement and more economical; and (2) approximate methods of analysis provide valuable physical insights to the indentation problem that will help to focus further research efforts.

Several theoretical models based on approximate methods of analysis that idealize the ice sheet as an isotropic continuum have been proposed for predicting global ice forces. These include: (1) the upper and lower bound, plasticity type solutions of Michel and Toussaint (1977), who assumed a von Mises material for ice, and Croasdale et al. (1977), who assumed a Tresca material for ice, (2) the reference stress, power-law creep solution of Ponter et al. (1983), and (3) the upper bound, power-law creep solutions of Bruen and Vivatrat (1984) and Vivatrat et al. (1984). The plasticity type models require empirical definition of an average strain rate measure to account for the viscous behavior of ice. The reference stress approach accounts for the effect of variability in material constants in an approximate sense, and the upper bound, power-law creep solutions require accurate specification of ice sheet kinematics. No equivalent theoretical models exist for the case where either pure (linear elastic) fracture or combined viscous and fracture effects dominate. Theoretical predictions of interface pressures are not generally available.

Two theoretical models have been developed for predicting indentation pressures assuming the ice sheet to be transversely isotropic. They are: (1) the upper and lower bound, plasticity solution of Ralston (1978), and (2) the upper bound, power-law creep solution of Vivatrat and Chen (1985). The former model is pressure-sensitive while the latter is pressure-insensitive. The former model has been incorporated in the API Bulletin 2N guidelines (1982).

This chapter discusses two approximate methods of analysis, the upper bound and strain path methods, to study the problem of sea ice indentation in the creeping mode of deformation, accounting for the spatial variation of strain-rates. The upper bound method traces its origin to research in plasticity theory where it has been extensively used, while the strain path method evolved in the geotechnical engineering field as an alternative to the stress path method of analysis. The key difference in the two analyses is that point stresses within the continuum can be obtained with the strain path method. As a result, local stresses at the ice-structure interface can be estimated, unlike the upper bound method which only yields an estimate of the global ice pressure. Although the accuracy with which local stresses can be estimated by the strain path method is debatable, the method tends to provide reasonable order of magnitude estimates. However, both methods rely on an adequate specification of the velocity field in the ice sheet. In the present work, this is obtained through a combination of theoretical modeling based on fluid mechanics and field ice movement survey data from an artificial island in the Beaufort Sea. In particular, two theoretical kinematic models are considered: one resulting from the superposition of a point source and uniform flow (Kinematic Model A) that has been studied previously (Bruen and Vivatrat, 1984, and Vivatrat et al., 1984); and the other from the superposition of a doublet and uniform flow (Kinematic Model B).

An important aspect of the analytical work is the specification of the mechanical properties of ice. In order to provide continuity with previous work on the topic, the commonly postulated isotropic, incompressible three-dimensional extension of the uniaxial power-law creep model is studied. The predicted global ice pressures are compared with those from models developed previously by other investigators, e.g., API Bul. 2N, Ponter et al., and Bruen & Vivatrat. The anisotropic power-law model presented in Chapter 2 is used to estimate the global forces based on the upper bound method.

4.2 BOUND METHOD VERSUS STRAIN PATH METHOD

In the solution of continuum mechanics problems, two methods of converging approximations are often applied. This involves relaxation of either the statical or the kinematic field equations and boundary conditions. In plastic limit analysis, these dual procedures are complementary in that they lead to arbitrarily close bounds from above and below to the same scalar quantity. For example, by relaxing the kinematic conditions but imposing an equilibrated field of stress, a lower bound on the applied load can be obtained. An upper bound (conservative) solution to a continuum mechanics problem may be derived by relaxing the statical conditions and boundary conditions, and using velocity fields that satisfy the kinematic constraints for the problem. These approximate analysis techniques are widely used in metal forming processes. Since the upper bound method provides conservative loading estimates, its derivation is pursued in what follows.

By applying the principle of virtual work to a continuum with no body forces and any kinematically admissible displacement increment field, it is possible to obtain:

$$\int_S T_i du_i^* \, dS = \int_V \sigma_{ij} \, d\varepsilon_{ij}^* \, dV \qquad (4.1)$$

where T_i are the tractions on the surface S, and σ_{ij} are the stresses in the volume space V. du_i^* are the virtual displacements on the surface and $d\varepsilon_{ij}$ are the compatible virtual strains in the volume. From Drucker's convexity criterion for the failure surface it follows that:

$$\int_V (\sigma_{ij}^\circ - \sigma_{ij}) \, d\varepsilon_{ij}^\circ \, dV \geq 0 \qquad (4.2)$$

where σ_{ij}° and $d\varepsilon_{ij}^\circ$ represent a consistent state different from that of σ_{ij} and $d\varepsilon_{ij}$, which in turn are also consistent. Assuming that the superscript $\circ$ and $*$ represent the same state, Eqs. 4.1 and 4.2 reduce to:

$$\int_V \sigma_{ij}^* \, d\varepsilon_{ij}^* \, dV \geq \int_S T_i du_i^* \, dS \qquad (4.3)$$

The surface integral consists of two parts; one in which the tractions are specified (S_T) and the other in which displacements are specified (S_u). Since the kinematic constraints are satisfied, $du_i^* = du_i$ on the surface where displacements are prescribed. Thus,

$$\int_V \sigma_{ij}^* \, d\varepsilon_{ij}^* \, dV \geq \int_{S_T} T_i du_i^* \, dS + \int_{S_u} T_i du_i \, dS \qquad (4.4)$$

Bruen and Vivatrat (1984) and Vivatrat et al. (1984) have used the upper bound method for steady creep of ice to obtain the average global pressure on an indenter. In their analysis, Eq. 4.4 has been expressed in terms of strain-rates $\dot{\varepsilon}_{ij}$ and velocities U_i instead of strain and displacement increments, i.e.,

$$\int_V \sigma^*_{ij} \; \dot{\varepsilon}^*_{ij} \, dV \geq \int_{S_T} T_i U^*_i \, dS + \int_{S_U} T_i U_i \, dS \tag{4.5}$$

In many practical problems, the material is considered to be incompressible and the constitutive laws relate the strains or strain-rates to the deviatoric stresses S_{ij}. Then Eq. 4.5 reduces to:

$$\int_V S^*_{ij} \; \dot{\varepsilon}^*_{ij} \, dV \geq \int_{S_T} T_i U^*_i \, dS + \int_{S_U} T_i U_i \, dS \tag{4.6}$$

where S^*_{ij}, $\dot{\varepsilon}^*_{ij}$ and U^*_i are the deviatoric stresses, strain-rates and velocities obtained from an assumed kinematically admissible velocity field. T_i and U_i are the actual surface tractions and velocities. Upper bound estimates of indentation pressure can be obtained by specializing Eq. 4.5 for the problem under consideration. A similar expression can be obtained for Eq. 4.4.

The upper bound method described here does not make use of the equilibrium equations for the continuum. As such, point stresses in the continuum are unknown. In order to obtain this information, Hill (1963) has suggested an approximate method by which octahedral (hydrostatic) stresses can be derived from deviatoric stress gradients using the equilibrium equation. The sum of the octahedral and deviatoric stresses yields the stress field. This idea was developed and first applied to deep penetration problems in soil mechanics by Baligh (1975, 1984) for estimating the far-field stresses. These problems are essentially strain controlled, i.e., the strains and deformations are to a large extent independent of the constitutive relations.

The upper bound method with its extension for evaluating the stress field has become known in geotechnical engineering as the strain path method of analysis. This is in contrast to the stress path method which assumes that the statical conditions of a problem are essentially known and independent of the constitutive relations. In structural engineering, this would involve approximating an indeterminate problem as statically determinate. The strain path method may be considered as approximating an indeterminate problem as kinematically determinate.

In applying the strain path method to the ice indentation problem, the major assumption is that the strain and strain-rate field for the ice sheet can be obtained from the kinematic conditions with no reference to constitutive relations or equilibrium equations. This is an approximation and hence the derived stress field will also be approximate in general. However, the method is computationally very attractive when compared with a detailed finite element analysis. In addition, the method provides valuable insights to the indentation problem (as will become clear in later sections) which is difficult to obtain from a purely numerical approach.

The basic steps for evaluating stresses within the ice sheet using the strain path method are summarized below:

(a) Determine the velocity field through a combination of analytical modeling and field ice movement surveys. The velocity field describes the movement of ice particles around the structure and should satisfy the conservation of mass (or volume) conditions and the kinematic boundary conditions.

(b) Compute the strain-rate field by differentiating the velocities with respect to the spatial coordinates.

(c) Evaluate the deviatoric stress field using the constitutive equations.

(d) Obtain octahedral stresses by spatially integrating the equilibrium equations (the octahedral stresses will in general be path dependent).

(e) Estimate the total stresses by summing the deviatoric and octahedral stresses.

Then, the local stresses at the ice-structure interface can be obtained from the total stress field, while global pressures may be estimated with the bound method and/or by integration of the local stress field. The degree of approximation in the estimated stress field can be assessed by comparing the octahedral stresses obtained by integration along different (i.e., orthogonal) paths and by noting the error in satisfying the statical boundary conditions. Another way of making the former comparison is to integrate along one path and to compare the magnitude of fictitous body forces required for equilibrium in the orthogonal direction with the stress gradients in that direction. Equations describing the steps in the strain path method are provided in the following section after discussing the kinematic modeling of the ice sheet.

4.3 KINEMATIC MODELING OF ICE SHEET

Both the upper bound and the strain path methods require accurate specification of the kinematic field. For the upper bound method, a kinematic field that is a good approximation to the actual conditions will give an upper bound that is closer to the actual value. For the strain path method, a good approximation will result in better estimates of the strain and strainrate fields which in turn will result in good estimate of the stress fields.

The fundamental assumption of the strain path method of analysis is that the kinematic conditions of a problem may be satisfied without knowledge of the constitutive and equilibrium relations for the continuum. If for such strain or strain-rate controlled problems an accurate velocity field can be postulated, then the strain and strain-rate field would follow directly from it. The velocity field can be derived from field surveys of sheet ice movement, or from theoretically postulated stream or potential functions.

In the study of deep penetration problems in soil mechanics, Baligh (1975) has used theoretical velocity fields resulting from the superposition of a series of point sources and sinks (negative sources) with varying strength and a uniform flow field. The derivations assume an ideal fluid (inviscid, incompressible), steady flow (convective changes in velocity can occur), irrotational motion (assures existence of a velocity potential) and two-dimensional flow (in conjunction with the incompressibility condition assures existence of a stream function). For a two-dimensional, incompressible and irrotational flow, the streamlines and potential lines are orthogonal to each other and can be used interchangeably to specify the flow kinematics.

Two theoretically postulated velocity fields are considered in this work: one resulting from the superposition of a single point source and uniform flow, and the other resulting from the superposition of a doublet and uniform flow. The former model has been studied extensively by Bruen and Vivatrat (1984) and Vivatrat et al. (1984). In what follows, the necessary mathematical equations describing the flow kinematics are developed for the two models. The models are then calibrated with data on sheet ice movement obtained from a field survey on an artifical island.

4.3.1 Theoretical Kinematic Models

Kinematic Model A -- Figure 4.1 shows the streamlines resulting from the superposition of a uniform flow with a point source. Point O in the figure refers to the origin of the source while point S is the stagnation point, representing a point of no motion. The streamline passing through the stagnation point defines the bluff-body, i.e., the region where the on-coming sheet of ice cannot enter as a result of interaction with the indenter or inert ice. The indenter radius can be taken as the distance from O to S, r_o.

The streamfunction, ψ, for the flow follows from the theory of fluid mechanics and is given by:

$$\psi = - U r \sin \theta - U r_o \theta \tag{4.7}$$

where U is the far field velocity associated with the uniform flow, and (r, θ) represent a polar coordinate system with origin at O. The angle θ is anticlockwise positive and is zero along the direction of the uniform flow. The locus of all points corresponding to a given streamfunction value, say $\psi = \psi_1$, describes a streamline. The tangent at any point on the streamline defines the direction of fluid velocity at the point. Thus, there can be no flow velocity perpendicular to a

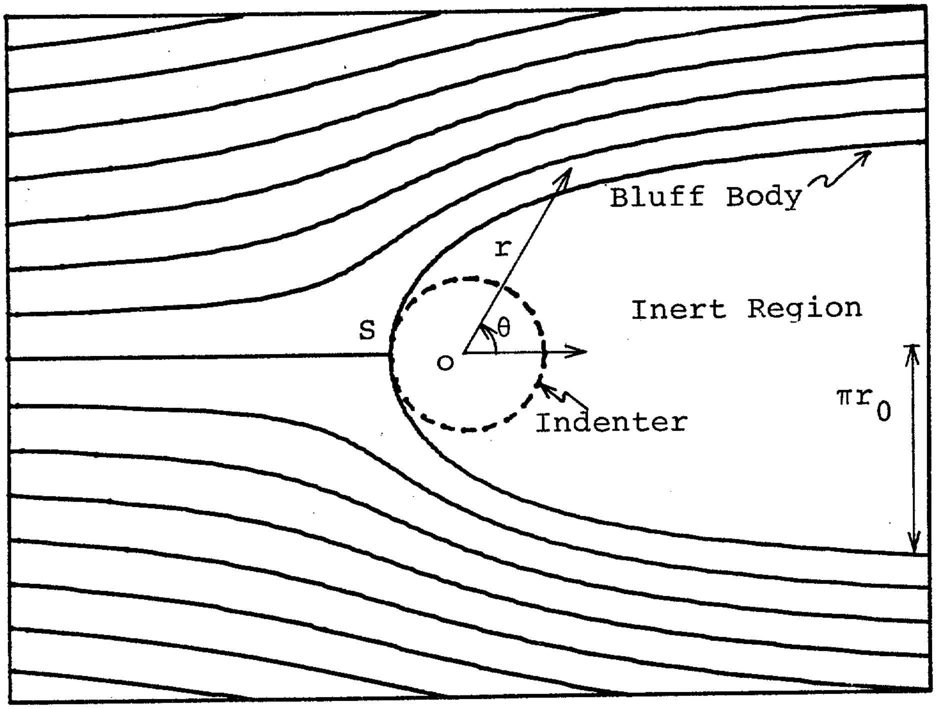
Bluff Body
r
θ
S
o
Inert Region
Indenter
πr_0

Figure 4.1 Streamlines for the Superposition of a Point Source with a Uniform Flow (Kinematic Model A).

streamline. Under steady flow conditions, the streamline also represents the path followed by any given particle as a function of time.

The velocity of flow can be obtained by considering two streamlines separated by an infinitesimal distance and recognizing that the difference in streamfunction values defines the flow rate. It follows that:

$$U_r = \frac{-1}{r} \frac{\partial \psi}{\partial \theta} = U \cos \theta + U \frac{r_o}{r} \quad (4.8)$$

$$U_\theta = \frac{\partial \psi}{\partial r} = - U \sin \theta \quad (4.9)$$

The bluff-body is described by the following equation:

$$r = r_o \frac{(\pi - \theta)}{\sin \theta} \quad (4.10)$$

with the half-width of the body at $r=\infty$ equal to πr_o. This model assumes that the normal velocity at the ice/bluff-body interface is zero while the tangential velocity is not zero in general. The maximum velocity occurs on the bluff-body at $\theta=63°$ and is equal to 1.26 U. The bluff-body can be viewed as consisting of a circular region of radius a representing the indenter and another region possibly containing inert (stationary) ice. Even if this is valid, the tangential contact between the moving ice sheet and the half-body could be either friction-free or possess finite frictional forces. This imposes a statical boundary condition with which the chosen velocity field may or may not be consistent.

Kinematic Model B -- Figure 4.2 shows the streamlines resulting from the superposition of a uniform flow with a doublet. The bluff-body in this case is a circle of radius, r_o. This represents flow past a cylindrical indenter with contact at all points on the circumference.

The streamfunction and flow velocity are given by the following equations:

$$\psi = - U r \sin \theta + U \frac{r_o^2}{r} \sin \theta \tag{4.11}$$

$$U_r = U \left[1 - \frac{r_o^2}{r^2}\right] \cos \theta \tag{4.12}$$

$$U_\theta = - U \left[1 + \frac{r_o^2}{r^2}\right] \sin \theta \tag{4.13}$$

On the bluff-body $r = r_o$ which represents the indenter, the radial velocity is zero while the tangential velocity is equal to $-2U \sin \theta$ with a maximum of $-2U$ at $\theta = \pi/2$. Once again, the statical boundary conditions in the tangential direction may or may not be satisfied by the chosen velocity field.

4.3.2 Calibration with Field Ice Movement Data

The theoretical velocity fields are calibrated with field ice movement data from an artifical island in the Beaufort Sea, obtained over a period of seven weeks during peak winter ice formation. The surveys were carried out over the 39 stations at least once per day, although during high movement

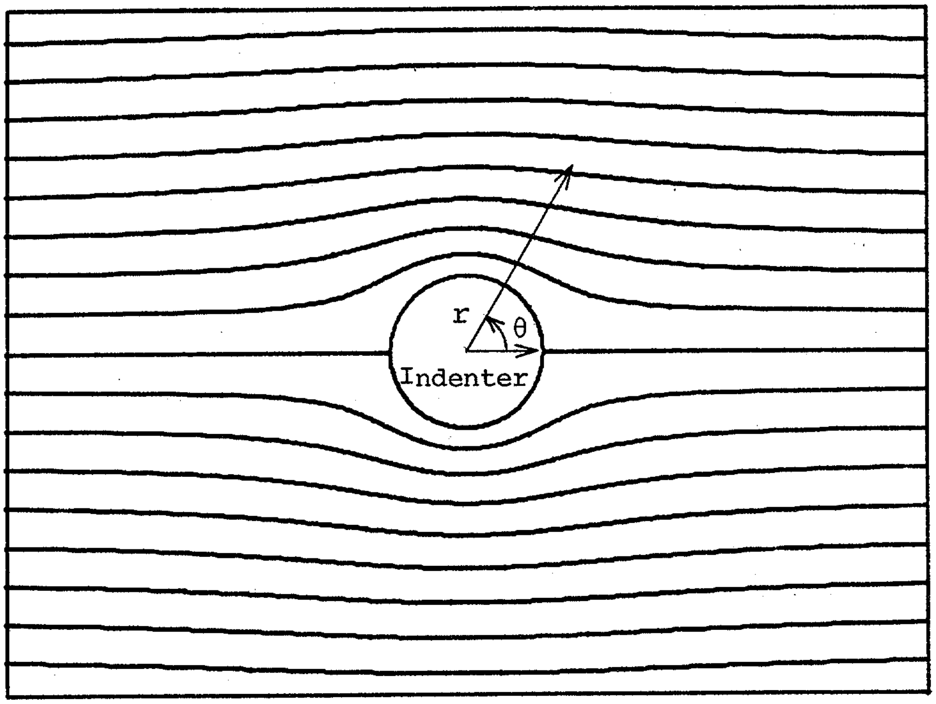
r
θ
Indenter

Figure 4.2 Streamlines for the Superposition of a Doublet with a Uniform Flow (Kinematic Model B).

events the surveys were made every 12 hours. Not all stations existed at the same time, and a few were removed and repositioned four days after the survey began.

Eight sets of data representing a range of movement magnitudes and different directions of ice sheet movement were studied here. A rubble pile with relatively no ice movement surrounded the island. In one of the cases, a major macrocrack was observed on the downstream side of sheet ice movement.

The data showed that ice movement downstream and directly at the back of the indenter was of the same order of magnitude as on the upstream side, and as such should be considered part of the ice sheet flow. Thus Kinematic Model A which considers no flow within the bluff-body is not representative of field conditions. Also, it cannot explain the observed downstream macrocracking. On the other hand, Kinematic Model B predicts movements of similar magnitude on the upstream and downstream side, and can explain the macrocracking if tensile stresses develop on the downstream side. The macrocracking issue for this model is further explored in the next section. In what follows, the accuracy with which the kinematic models approximate the field data is discussed. For Kinematic Model A, measured movement at points within the bluff-body are in error by 100 percent.

The calibration is based on the following three criteria:

(a) streamfunction values for a particle at the start and end of the observation period should be equal under steady flow conditions; (b) the average movement rate measured should be approximately equal to the average of the predicted velocities over the observation period; and (c) the measured direction of movement must equal the predicted bearing. The comparison in (a) can be carried out by using a normalized variable ψ/U in Eqs. 4.7 and 4.11. For (b) it is necessary to estimate the far-field velocity U to make the theoretical prediction. In this work, the average movement rate at the farthest upstream station is taken to be U. The average of the tangent to the streamline at the beginning and end points gives the theoretical bearing in case (c). The relative error measures used in the three cases are: (a) ratio of streamfunction value at beginning of period to that at the end of the period; (b) ratio of average measured movement rate to average theoretically predicted velocity; and (c) difference in degrees of angle between measured bearing and average theoretical bearing. For no error, the error measures should equal one, one and zero, respectively.

Calibration with the data showed that both kinematic models can model the streamfunction field very accurately over their domains of applicability. For Model A the errors vary from less than one percent in general to as much as 25 percent, even when there is no macrocrack formation. For

Model B, the errors are generally less than one percent in all cases except the case with macrocrack formation.

The errors in velocity predictions are much higher for both models. Some stations near the rubble pile surrounding the structure are significantly in error due to an inadequate modeling of the structural geometry, e.g., choice of diameter D. In the cases affected by macrocracking: (a) separate and large regions of the continuum are adequately modeled by both theoretical velocity fields, (b) Model B is in general better than Model A. Typical errors in the velocity are on the order of five to ten percent if the above exceptions are taken into account.

The errors in bearing predictions are on the order of five to ten degrees for Kinematic Model B and larger for Model A. The discrepancies, where they are larger, can be explained with arguments similar to that for velocities.

In summary, the following comments can be made: (a) Kinematic Model A does not adequately model the field data considered here; (b) Kinematic Model B provides a good description of the measured flow field and can be used to explain the observed macrocracking if tensile stresses develop on the downstream side; (c) even after macrocracking, Model B accurately models the upstream flow field; (d) the transition from creeping behavior to macrocracking occurs for velocities less than 1 ft/hr (85×10^{-6} m s^{-1}); and (e) the theoretical model was able to aid detection of unusual events in the field data such as the macrocrack formation and sudden movement of the rubble pile at some of the stations.

In this study, attention is focussed on both the simple kinematic models since they provide valuable insights to the indentation problem. However, better models and data fitting techniques can be applied to the ice survey data to improve results. In particular: (i) the effective and arbitrary geometry of the structure/rubble pile configuration can be accounted for by combining several doublets and/or source/sink combinations; and (ii) the flow kinematics at the ice-structure interface may be better modeled by considering a viscous (Newtonian) fluid rather than the ideal fluid considered here. The latter change is more important for assessing local indentation pressures as opposed to average global pressures.

4.4 ICE PRESSURES FOR POWER-LAW CREEP

Both global and local pressures during sheet ice indentation are evaluated here for the two kinematic models using the strain path method of analysis. The isotropic, incompressible three-dimensional extension of the uniaxial power-law creep leads to the following constitutive model:

$$\underline{S} = \frac{2}{3} \left(\frac{1}{a} \right)^{\frac{1}{N}} \dot{\varepsilon}_e^{\frac{1}{N} - 1} \underline{\dot{\varepsilon}} \qquad (4.14)$$

where $\underline{S}$ and $\underline{\dot{\varepsilon}}$ are the deviatoric stress and strain-rate tensors, respectively; $\dot{\varepsilon}_e$ is the effective strain-rate defined as:

$$\dot{\varepsilon}_e = [\,\frac{2}{3}\,\underline{\dot{\varepsilon}}^T\,\underline{\dot{\varepsilon}}\,]^{1/2} \tag{4.15}$$

Both the constant a and N, the power-law exponent, may be obtained from uniaxial testing of ice as illustrated in Chapter 2. A value of N=1 corresponds to a viscoelastic material, while N=∞ represents a rigid plastic material. Typical values of N for sea ice range from 2.5 to 4. The three-dimensional model assumes that the material is incompressible and isotropic. Furthermore, Eq. 4.14 reduces to the uniaxial equation under appropriate conditions.

In order to apply Eq. 4.14 it is necessary first to obtain the strain-rate field from the kinematic models. This is based on the following equations:

$$\dot{\varepsilon}_{rr} = \frac{\partial U_r}{\partial r} \tag{4.16}$$

$$\dot{\varepsilon}_{\theta\theta} = \frac{1}{r}\,\frac{\partial U_\theta}{\partial \theta} + \frac{U_r}{r} \tag{4.17}$$

$$\dot{\varepsilon}_{r\theta} = \frac{\dot{\gamma}_{r\theta}}{2} = \frac{1}{2}\,[\frac{1}{r}\,\frac{\partial U_r}{\partial \theta} + \frac{\partial U_\theta}{\partial r} - \frac{U_\theta}{r}\,] \tag{4.18}$$

The octahedral stresses σ_{oct} can be obtained from the deviatoric stresses with the help of the equilibrium equations:

$$\sigma_{ij,i} + b_j = 0 \qquad (4.19)$$

where

$$\sigma_{ij} = S_{ij} + \sigma_{oct}\,\delta_{ij} \qquad (4.20)$$

with the body force b_j being zero for the problem being solved. Substituting Eq. 4.20 into Eq. 4.19 and expressing the result in polar coordinates:

$$\frac{\partial \sigma_{oct}}{\partial r} = -\frac{\partial S_{rr}}{\partial r} - \frac{1}{r}\,\frac{\partial S_{r\theta}}{\partial \theta} - \frac{S_{rr} - S_{\theta\theta}}{r} - b_r \qquad (4.21)$$

$$\frac{\partial \sigma_{oct}}{\partial \theta} = -\frac{\partial S_{\theta\theta}}{\partial \theta} - r\,\frac{\partial S_{r\theta}}{\partial r} - 2S_{r\theta} - rb_{\theta} \qquad (4.22)$$

Since the right hand side of Eqs. 4.21 and 4.22 are known, integration of either Eq. 4.21 with respect to r or Eq. 4.22 with respect to θ leads to the octahedral stress field. However, due to the approximate nature of the kinematic field, these two equations will yield different octahedral stress fields in general. Thus, the integration of Eqs. 4.21 and 4.22 is path dependent. The degree of error in the solution can be assessed by comparing the octahedral stresses obtained from integration along two orthogonal paths, or by integrating one of the equations and obtaining the fictitious body forces required to satisfy equilibrium in the other direction using the computed octahedral stresses.

The total stress field in the continuum may be obtained by summing the deviatoric and octahedral stress fields as in Eq. 4.20. The local stresses at the ice-structure interface can then be obtained by substituting the appropriate coordinates (r, θ) into the total stress equations. Global pressures are estimated with the bound method and by integration of the local stresses around the indenter.

The results presented in this chapter are based on the isotropic power-law creep model with the material constants for Eq. 4.14 given below:

$$a = 2.215 \times 10^{-6}\ (\mathrm{MPa})^{-3}\ \mathrm{s}^{-1} \qquad N = 3 \tag{4.23}$$

The global ice pressures predicted using the upper bound method for a transversely isotropic power-law creep model is given in detail in Appendix D.

Kinematic Model A -- For the streamfunction and velocity field defined by Eqs. 4.7 to 4.9, the strain-rate field is given by:

$$\dot{\varepsilon}_{rr} = - \frac{Ur_o}{r^2} \qquad \dot{\varepsilon}_{\theta\theta} = - \dot{\varepsilon}_{rr} \qquad \dot{\varepsilon}_{r\theta} = 0 \tag{4.24}$$

and the effective strain-rate is equal to:

$$\dot{\varepsilon}_e = \frac{2}{\sqrt{3}} \frac{Ur_o}{r^2} \tag{4.25}$$

The deviatoric stress field is defined with the following equations:

$$S_{rr} = -\frac{1}{\sqrt{3}} \left[\frac{2}{\sqrt{3}} \quad \frac{1}{a} \quad \frac{Ur_o}{r^2} \right]^{\frac{1}{N}} \tag{4.26}$$

$$S_{\theta\theta} = -S_{rr}$$

$$S_{r\theta} = 0$$

Integration of the equilibrium equations yields the following octahedral stress field:

$$\sigma_{oct} = (N-1)\, S_{rr} \tag{4.27}$$

Since the octahedral stress field, σ_{oct}, for this kinematic model is path independent, equilibrium is exactly satisfied in addition to the constitutive relations, kinematic field equations and kinematic boundary conditions. In spite of this, the statical traction boundary conditions at the ice/bluff-body interface will in general not be satisfied by the model.

The total stress field is given by:

$$\sigma_{rr} = N\, S_{rr}$$

$$\sigma_{\theta\theta} = (N-2) S_{rr} \tag{4.28}$$

$$\sigma_{r\theta} = 0$$

Four comments can be made:

(i) the maximum strain-rate occurs at the ice/bluff-body interface at $r=r_o$, and is equal to U/r_o or $2U/D$, if $D = 2r_o$ is the indenter diameter,

(ii) the stress field decays as $r^{-2/N}$, which for $N=3$ is $r^{-2/3}$,

(iii) the stress field is axisymmetric, i.e., independent of θ, and

(iv) the octahedral stress is zero for a linearly viscoelastic material ($N=1$).

The global pressure can be estimated by the upper bound method, assuming a frictionless ice/bluff-body interface. This is similar to the case studied by Bruen and Vivatrat (1984) and Eq. 4.6 reduces to:

$$PU \leq \int_V S^*_{ij} \dot{\varepsilon}^*_{ij} \, dV \qquad (4.29)$$

or

$$\frac{P}{Dt} \leq \frac{N}{\sqrt{3}} \int_0^{\pi} \left(\frac{\sin\theta}{\theta}\right)^{2/N} d\theta \left[\frac{2}{\sqrt{3}} \frac{1}{a} \frac{U}{r_o}\right]^{\frac{1}{N}} \qquad (4.30)$$

A second approach to estimating the global pressure involves integration of the local stresses given by Eq. 4.28 around the bluff-body, i.e.,

$$P = t \int (\sigma_{rr} \cos\theta \, r d\theta + \sigma_{\theta\theta} \sin\theta \, dr) \qquad (4.31)$$

Using the equation for the bluff-body, Eq. 4.10, Eq. 4.31 reduces to

$$P = \lim_{\theta \to 0} t \int_{\theta}^{2\pi-\theta} \left[(2-N)\, r_o + 2r \cos\theta\right] S_{rr} d\theta = 0 \qquad (4.32)$$

Thus the average global pressure is predicted to be zero, unlike the upper bound method. If the actual frictional forces predicted by the strain path method at the ice/bluff-body interface are included in the upper bound method, it can be easily shown that the upper bound method also predicts zero pressure. However, the bound theorems do not apply for the case of friction with relative motion. The implications of this finding are more fully discussed for Kinematic Model B.

The above simple example shows that: (i) the upper bound global pressure estimate is very sensitive to the frictional forces at the ice/bluff-body interface, and (ii) in order to correctly model the statical boundary conditions of the problem, a complete finite element analysis is necessary. The local stresses predicted by the strain path method may also be very approximate, although order of magnitude comparisons with the global pressures are in general likely to be reasonable. Local pressure evaluation is pursued only for Kinematic Model B as it better represents the field ice movement data.

Kinematic Model B -- The strain-rate field for the streamfunction and velocity defined by Eqs. 4.11 to 4.13 is given below:

$$\dot{\varepsilon}_{rr} = \frac{2Ur_o^2}{r^3} \cos\theta$$

$$\dot{\varepsilon}_{\theta\theta} = - \dot{\varepsilon}_{rr} \tag{4.33}$$

$$\dot{\varepsilon}_{r\theta} = \dot{\varepsilon}_{rr} \tan\theta$$

and the effective strain-rate is equal to:

$$\dot{\varepsilon}_e = \frac{4}{\sqrt{3}} \frac{Ur_o^2}{r^3} \tag{4.34}$$

The deviatoric stress field can be obtained by applying Eq. 4.14 to Eqs. 4.33:

$$\begin{aligned} S_{rr} &= \frac{1}{\sqrt{3}} \left[\frac{4}{\sqrt{3}} \frac{1}{a} \frac{Ur_o^2}{r^3} \right]^{\frac{1}{N}} \cos \theta \\ S_{\theta\theta} &= - S_{rr} \\ S_{r\theta} &= S_{rr} \tan \theta \end{aligned} \tag{4.35}$$

Substituting the above equations into Eq. 4.21 and integrating in the radial direction yields:

$$\sigma_{oct} = (N-1)\ S_{rr} \tag{4.36}$$

Using Eqs. 4.35 and 4.36, the fictitious body force necessary to satisfy equilibrium in the θ direction (Eq. 4.22) can be obtained:

$$b_\theta = \frac{(N-1)(N-3)}{Nr}\ S_{rr} \tan \theta \tag{4.37}$$

For this kinematic model, the octahedral stresses are path dependent, although for N=1 and N=3 the fictitious body force is zero and equilibrium is exactly satisfied in the continuum. However, the statical interface boundary conditions will in general not be satisfied.

The total stress field is given by:

$$\begin{aligned} \sigma_{rr} &= NS_{rr} \\ \sigma_{\theta\theta} &= (N-2)\ S_{rr} \\ \sigma_{r\theta} &= S_{rr} \tan \theta \end{aligned} \tag{4.38}$$

The following comments can now be made:

(i) the maximum strain-rate occurs at the ice-structure interface, $r=r_o$, and is equal to $2U/r_o$ or $4U/D$,

(ii) the stress field decays as $r^{-3/N}$ (not $r^{-2/N}$ as predicted by Kinematic Model A), which for N=3 is 1/r,

(iii) the stress field is not axisymmetric, and

(iv) the octahedral stress is zero for a linearly viscoelastic material.

According to Eq. 4.38 the radial stresses downstream of the indenter are tensile and equal in magnitude to the upstream compressive stresses, consistent with the material law. The tangential stresses behave similarly for typical values of N, although their magnitudes could be half or less than half of the radial stresses. These are principal stresses at $\theta=0$. As such, it is reasonable to expect a macrocrack formation on the downstream side of the indenter. This is indeed borne out by the field ice movement data.

The global pressure can be estimated using the bound method, assuming either a frictionless interface or an interface with the frictional stresses predicted by the strain path method. (The method does not strictly apply for the latter case.) In fact, the stresses predicted by the strain path method, at the interface are opposite in direction to what should be normally expected. This error in the stress field at the interface means that the results predicted with the frictional stresses included may be wrong. The respective mathematical expressions are derived from Eq. 4.6 for $D=2r_o$ and are as follows:

No friction

$$\frac{P}{Dt} \leq \frac{4\pi}{\sqrt{3}} \frac{N}{N+3} \left[\frac{4}{\sqrt{3}} \frac{1}{a} \frac{2U}{D} \right]^{\frac{1}{N}} \qquad (4.39)$$

With friction

$$\frac{P}{Dt} \leq \sqrt{3}\pi \frac{N-1}{N+3} \left[\frac{4}{\sqrt{3}} \frac{1}{a} \frac{2U}{D} \right]^{\frac{1}{N}} \qquad (4.40)$$

The ratio of Eq. 4.39 to Eq. 4.40 is equal to 4N/3(N-1), which varies between 1.8 and 2.2 for $2.5 \leq N \leq 4$. Intuitively, interface friction should increase indentation pressures. However, both kinematic models studied here predict a significant decrease in pressure. This is because they are derived from considerations for ideal, non-viscous fluids and as such do not correctly model interface conditions. Even if more exact velocity fields can be postulated theoretically, the available field data does not provide adequate resolution of the ice movements in the immediate vicinity of the structure to calibrate the kinematic models. This result once again demonstrates the importance and need for accurately modeling frictional effects at the ice-structure interface.

Although Eq. 4.39 is a conservative upper bound, the degree of conservatism may be unacceptably high.

Integration of the local stresses given in Eq. 4.38 around the bluff-body yields another estimate of global pressure accounting for the frictional stresses of the strain path method. This may be expressed as:

$$\frac{P}{Dt} = \frac{\pi}{2\sqrt{3}} (N-1) \left[\frac{4}{\sqrt{3}} \frac{1}{a} \frac{2U}{D} \right]^{\frac{1}{N}} \tag{4.41}$$

Both Eqs. 4.40 and 4.41 predict zero pressure for a linearly viscoelastic material with N=1. Furthermore, the ratio of the upper bound method to Eq. 4.41 is 6/(N+3), which varies between 0.86 and 1.09 for $2.5 \leq N \leq 4$. For N=3 the ratio is one since the strain path method has been shown to be exact in that case.

In order to develop a feel for the magnitudes of strain-rates, local stresses and global pressures under typical field conditions, a range of far-field velocities U and indenter diameters D is considered. The ice material properties are given in Eq. 4.23. Table 4.1 presents the maximum radial strain-rates which occur at the ice-structure interface. For the artificial island considered in the earlier section, the maximum strain-rate just prior to macrocracking is on the order of 10^{-6} sec^{-1} or less. For strain-rates less than 10^{-6}, experimental evidence shows that sea ice tends to behave as a creeping material with tensile

Table 4.1 Maximum Radial Strainrates on Ice-Structure Interface (sec^{-1}).

D(ft) U(ft/hr)	200	300	400	500
0.1	$5.6x10^{-7}$	$3.7x10^{-7}$	$2.8x10^{-7}$	$2.2x10^{-7}$
1	$5.6x10^{-6}$	$3.7x10^{-6}$	$2.8x10^{-6}$	$2.2x10^{-6}$
10	$5.6x10^{-5}$	$3.7x10^{-5}$	$2.8x10^{-5}$	$2.2x10^{-5}$

Table 4.2 Maximum Radial Stresses on Ice-Structure Interface (psi).

D(ft) U(ft/hr)	200	300	400	500
0.1	166	145	132	71
1	358	313	284	264
10	771	674	612	568

and compressive strengths being approximately equal. Table 4.2 presents the maximum radial stresses on the ice-structure interface. The local radial stresses predicted by the strain path method are on the order of 260 psi (1.8 MPa). The radial stresses are compressive upstream of the indenter and tensile on the downstream side, and are distributed in a cosinusoidal fashion. Tables 4.3 and 4.4 present the average global pressures using the upper bound method without friction (Eq. 4.39) and that obtained by integrating the stress field from the strain path method (Eq. 4.41). The pressures in the latter case are exactly half that of the former, as expected for N=3. The typical order of magnitude value for the global pressure is about 270 psi (1.9 MPa) for the latter case and 540 psi (3.8 MPa) for the upper bound method without friction. A key inference can be made based on these results: the local and global pressures are of the same order of magnitude. The local pressures (compressive or tensile) for the model studied here are not several times the average global pressure. This finding is important since it is generally believed that local stresses can be three times the average pressure.

4.5 COMPARISON WITH OTHER STUDIES

Average global pressures during sea ice indentation can be estimated using any one of the many predictive models available in the literature. In this study, the global pressures predicted by Kinematic Model B are compared with the

Table 4.3 Average Global Pressure Using Upper Bound Method without Friction (psi).

D(ft) U(ft/hr)	200	300	400	500
0.1	348	304	276	256
1	750	655	595	552
10	1615	1411	1282	1190

Table 4.4 Average Global Pressure Based on Integrated Stress Field (psi).

D(ft) U(ft/hr)	200	300	400	500
0.1	174	152	138	128
1	375	327	298	276
10	808	706	641	595

models of API (1982), Ponter et al. (1983), and Bruen and Vivatrat (1984). The general form of all these models may be expressed as:

$$\frac{P}{Dt} = \phi\ \sigma(\dot{\varepsilon}_a) \tag{4.42}$$

where ϕ is a constant depending in general on N, and $\sigma(\dot{\varepsilon}_a)$ is the uniaxial strength of ice evaluated at some average strain-rate $\dot{\varepsilon}_a$ expressed as:

$$\dot{\varepsilon}_a = \frac{U}{\phi \Psi D} \tag{4.43}$$

with Ψ being a second constant. In order to compare the various formulations, $\phi\Psi$ is assumed to equal two as suggested by API (1982) and the comparison can therefore be based on the parameter ϕ.

The values of ϕ predicted by the four formulations under consideration for a power-law creep model with N=3 is given in Table 4.5. At first glance the numbers seem highly scattered, varying from 1.91 to 7.61. However, there are some important differences among the models. The first two formulations apply for a flat indenter with ice pressures being allowed to develop only on the upstream side. For the API model, the sea ice is assumed to be columnar and the contact factor is set to one. In the Bruen and Vivatrat model (or Kinematic Model A), the problem geometry (Fig. 4.1) is different from that for the other models. In particular, the choice of indenter diameter

Table 4.5 Comparison of Average Global Pressures for Power-Law Creep with N=3 and Average Strain-Rate of U/2D.

Model	Constraints	ϕ
API	Plane Strain	4.12
	Plane Stress	3.13
Ponter et al (1983)	Plane Strain	3.28
	Plane Stress	1.91
Bruen and Vivatrat (1984) (Model A)	$D = 2\pi r_o$	3.00
	$D=2r_o$	6.43
Model B	Plane Strain (with friction)	3.81
	Plane Strain (without friction)	7.61

is subjective. If the indenter diameter is chosen as $2\pi r_o$, ϕ is about 47% of the value for $D=2r_o$. In the former case the indenter is located far away ($r\rightarrow\infty$) from the tip of the bluff-body with the region in between consisting of inert ice, while in the latter case the indenter is located at the tip of the bluff-body with the inert region downstream of the indenter. Field data on deformation patterns considered here indicate that both these assumptions may be unrealistic. The ϕ factor for Model B is based on a circular indenter with compressive stresses on the upstream side and tensile stresses on the downstream side. This is more representative of actual field conditions prior to breakout.

If the API and Ponter et al. models are extended to account for downstream tensile stresses, the ϕ factors would probably be twice as much since for the problem and material model considered (a) tensile and compressive strengths are equal, and (b) stress levels are equal but opposite in sign on the upstream and downstream sides. Then, ϕ for the API model would vary between 6.3 and 8.2 while for Ponter et al's it would vary between 3.8 and 6.6. The upper bound estimate without friction for Kinematic Model B yields the plane strain solution as a result of the chosen two-dimensional kinematic field.

In summary, it appears that for an indentation problem of the type encountered in the field, Kinematic Model B and

Ponter et al's reference stress method predict very similar global ice pressures.

4.6 SUMMARY

The prediction of global and local indentation pressures in the creeping mode of sea ice deformation, accounting for the spatial variation of strain-rates, using the upper bound and the strain path methods, leads to the following specific conclusions:

1. Kinematic Model B better models the ice movement survey data obtained from an artificial island in the Beaufort Sea than Kinematic Model A.
2. The maximum strain rate for Model A occurs at the stagnation point on the ice bluff-body interface and is equal to U/r_o, while for Model B it occurs at the same point and is equal to $2U/r_o$.
3. The stress field decays as $r^{-2/N}$ for Kinematic Model A and as $r^{-3/N}$ for Model B. The stress field is axisymmetric for Model A and not so for Model B.
4. In the creeping mode of ice deformation, the local ice pressures are of the same order of magnitude as or lower than the global pressures. The local pressures are not several times the average global pressure as is commonly believed. Even if the global pressures are reduced, e.g., by a factor of three, to account for scale (fracturing) effects, the local pressures

based on the strain path method will only be 1.5 (and not three) times the upper bound global pressure neglecting interface friction. For a typical artificial island just prior to breakout in winter, Model B predicts a pressure of about 260 psi (1.8 MPa).

5. Under essentially plane strain conditions, Kinematic Model B predicts global pressures that are intermediate between that proposed by API and Ponter et al. For a typical artificial island just prior to break-out with ice movements of less than 1 ft/hr (85×10^{-6} m s^{-1}), Model B predicts a pressure (neglecting interface friction) of approximately 530 psi (3.7 MPa).
6. The global pressures predicted by the upper bound method are very sensitive to the statical traction boundary conditions at the ice-structure interface. For Kinematic Model B, assuming no friction at the interface may lead to overconservative pressure estimates.

A key finding of the study in this chapter is that for the rate-dependent material models describing sea ice behavior, interface adfreeze and friction stresses can significantly influence both local and global ice pressures. This has major economic consequences for platform design.

Incorporation of these "non-conservative" stresses within the bound method may yield more accurate global ice pressures, but the solutions will not necessarily be upper bounds. More exact estimates of both local and global ice pressures using the strain path method may be obtained by postulating kinematic models that more correctly model the interface conditions. However, currently available field data does not provide adequate resolution of the ice movements in the immediate vicinity of the structure to calibrate such models. In conclusion, it appears that the development of numerical models based, for example, on the finite element method of analysis is necessary for more realistically studying ice-structure interaction problems where both global and local pressures are of interest.

CHAPTER FIVE

FINITE ELEMENT ANALYSIS OF PLANE STRESS INDENTATION

5.1 INTRODUCTION

Analytical studies of ice-structure interaction reported in the literature have been based on classical plasticity theory and creep limit solutions. In order to model material anisotropy, spatial-temporal variation of the strainrate field, through thickness variation of temperature, and the occurrence of multiple failure modes, it is necessary to resort to numerical solution procedures. Discrete element methods of analysis such as the finite element method or the boundary element method can be applied to solve problems with complex contact conditions and material behavior.

This chapter discusses the development and application of a finite element method of analysis to study sea ice indentation in the creeping mode. Both isotropic and transversely isotropic material models are examined. Numerical simulations are performed under plane stress conditions to predict the influence of (i) interface adfreeze and friction, (ii) material anisotropy, (iii) variability in parameters of the material model, (iv) rubble pile or grounded ice foot, and (v) ice sheet velocity on global forces and local pressures generated on a rigid cylindrical indenter.

The results are compared with those obtained from the approximate methods of analysis discussed in the previous chapter. Interface pressure distributions are obtained in addition to contours of stress and strain. Pressure-area curves constructed from the results are presented.

5.2 MATERIAL MODELING

The rate-dependent material model for sea ice assumes that the total strainrate is the sum of the elastic strainrate and the creep or viscous strainrate, i.e.,

$$\dot{\underline{\varepsilon}} = \underline{C}\ \dot{\underline{\sigma}} + \dot{\underline{\varepsilon}}_{cr} \tag{5.1}$$

where $\underline{C}$ is the linear elastic compliance matrix (see Appendix A), and does not vary in time for an orthotropic material. The creep component consists of primary or delayed elastic strains, secondary creep strains and tertiary creep strains. In general, this may be expressed as:

$$\dot{\underline{\varepsilon}}_{cr} = f(\underline{\sigma}, \dot{\underline{\sigma}}, \underline{\varepsilon}_{cr}, T) \tag{5.2}$$

where T allows for temperature dependence.

In order to provide continuity with previous work, the isotropic, incompressible three-dimensional extension of the uniaxial power-law creep model is extended to a general orthotropic elastic - power law creep model. As this model does not model the primary or tertiary creep strains, the theoretical formulation is slightly different from that presented in Chapter 2. As such, the theoretical formulation is briefly discussed in the following paragraphs.

To derive the relationship between the creep strainrate and stress vectors, an effective stress measure generalized for orthotropic materials with identical behavior in compression and tension is first defined.

$$\sigma_e^2 = 3/\beta\ [\frac{a_1}{3}(\sigma_{xx}-\sigma_{yy})^2 + \frac{a_2}{3}(\sigma_{yy}-\sigma_{zz})^2 + \frac{a_3}{3}(\sigma_{zz}-\sigma_{xx})^2 + 2a_4\,\sigma_{xy}^2 + 2a_5\,\sigma_{yz}^2 + 2a_6\,\sigma_{zx}^2\ ] \tag{5.3}$$

with $\beta=a_1+a_2$. This may be expressed in compact form using matrix notation as:

$$\sigma_e{}^2 = 3/\beta\ \underline{\sigma}^T\ \underline{G}\ \underline{\sigma} \tag{5.4}$$

where $\underline{G}$ is the matrix defined in Appendix A.

Under uniaxial (compressive) loading conditions, creep in ice is usually expressed in terms of a power law (Glen,1955). Then, the effective strainrate and effective stress are related by:

$$\dot{\varepsilon}_e = a\ \sigma_e{}^N \tag{5.5}$$

where a and N are constants. Comparison with the theoretical formulation given in Chapter 2 shows that $a=(M/A)^N$, and no primary or tertiary creep strains are included. The temperature dependence is included in the parameter A, as before, following an Arrhenius activation energy law which is valid for temperatures less than -10°C.

The creep strainrate vector can now be related to the effective stress vector by defining a scalar potential function ϕ which obeys the associated flow rule, i.e.,

$$\underline{\dot{\varepsilon}}_{cr} = \frac{\partial \phi}{\partial \underline{\sigma}} \qquad (5.6)$$

with

$$\phi = a \frac{\sigma_e^{N+1}}{N+1} \qquad (5.7)$$

Combining Eqs. 5.6, 5.7 and 5.4 yields the desired relationship:

$$\underline{\dot{\varepsilon}}_{cr} = \lambda \, \underline{S}^* \qquad (5.8)$$

where

$$\lambda = 3/\beta \; a \; \sigma_e^{N-1} \qquad (5.9)$$

and

$$\underline{S}^* = \underline{G} \; \underline{\sigma} \qquad (5.10)$$

Note that $\underline{S}^*$ is not the conventional deviatoric stress vector. It may be thought of as a pseudo deviatoric stress vector for an anisotropic material.

Given the stress vector, the pseudo deviatoric stresses may be obtained from Eq. 5.10. Then applying Eqs. 5.4, 5.9, and 5.8 in succession leads to the creep strainrate vector. Note that under isotropic conditions, i.e., a_1 to a_6 equal to one, all these equations reduce to the formulation proposed by

Palmer (1967). Methods for obtaining the model parameters a, N, and a_1 to a_6 have already been discussed in Chapter 2 and will not be repeated here.

5.3 FINITE ELEMENT FORMULATION

Governing Equations -- For general viscoplastic behavior, which includes creep, it is convenient to work with time derivatives of the governing equations for a solid. The weighted equilibrium-rate equation which forms the basis of the finite element displacement method is then given by:

$$\int \underline{B}^T \dot{\underline{\sigma}}\, dV = \dot{\underline{P}} \qquad (5.11)$$

where $\underline{B}$ is the strainrate - nodal velocity transformation matrix derived from the chosen displacement expansion for the finite element, i.e.,

$$\dot{\underline{\varepsilon}} = \underline{B}\, \dot{\underline{U}} \qquad (5.12)$$

Combining Eqs. 5.11 and 5.12 with Eq. 5.1 and defining $\underline{K}$ as the elastic stiffness matrix of the element leads to the element equilibrium equation:

$$\underline{K}\, \dot{\underline{U}} = \dot{\underline{P}} + \int \underline{B}^T \underline{D}\, \dot{\underline{\varepsilon}}_{cr}\, dV \qquad (5.13)$$

and the element stressrate - nodal velocity relations:

$$\dot{\underline{\sigma}} = \underline{D}\, \underline{B}\, \dot{\underline{U}} - \underline{D}\, \dot{\underline{\varepsilon}}_{cr} \qquad (5.14)$$

where $\underline{D}$ is the linear elastic rigidity matrix for an orthotropic material. The global stiffness matrix $\underline{K}_G$ is obtained from Eq. 5.13 using conventional procedures.

Solution Algorithm -- An iterative solution algorithm is developed to solve the pseudo-force form of the nonlinear governing equations given in Eqs. 5.13 and 5.14. Although the algorithm is applied to the specific material model presented, it can be easily generalized to account for cracking based on the limiting tensile strain criterion discussed earlier. For purposes of discussion, attention is focussed at the element level rather than the global level. At first the governing equations are integrated in time between t_i and t_{i+1} to yield:

$$\underline{K}\ (\underline{U}_{i+1}-\underline{U}_i) = \underline{P}_{i+1}-\underline{P}_i+\int \underline{B}^T\ \underline{D}\ (\underline{\varepsilon}_{cr,i+1}-\underline{\varepsilon}_{cr,i})\ dV \qquad (5.15)$$

$$\underline{\sigma}_{i+i}-\underline{\sigma}_i = \underline{D}\ \underline{B}\ (\underline{U}_{i+1}-\underline{U}_i) - \underline{D}\ (\underline{\varepsilon}_{cr,i+1}-\underline{\varepsilon}_{cr,i}) \qquad (5.16)$$

Creep strains which appear in both equations are nonlinear functions of stress since λ in Eq. 5.8 is not a constant. A two-level iterative algorithm is used to solve these equations for each new time step t_{i+1}. The key steps in the solution algorithm are as follows:

1. Compute the displacement increments from (the global form of) Eq. 5.15 for the given loading vector. In the first iteration on the equation, the incremental creep strains are assumed to be zero.
2. Compute the incremental stresses and incremental creep strains from Eq. 5.16 for the displacement increments obtained in step 1 using the iterative algorithm (lower-level iteration in k) discussed

below. In the first iteration on this equation assume the incremental creep strains to be zero.

3. Return to step 1 and iterate on Eq. 5.15 (higher-level iteration in j) using the incremental creep strains obtained in step 2 until convergence is achieved. Two convergence criteria are used: (a) ratio of norm of displacement increment vector to norm of displacement vector at given time step is less-than-or-equal-to 10^{-3}; and (b) absolute value of energy norm is less-than-or-equal-to 10^{-5}, i.e.,

$$\left| \frac{\underline{\Delta P}^j \cdot \underline{\Delta U}^j}{\underline{\Delta P}^o \cdot \underline{\Delta U}^o} \right| < 10^{-5} \qquad (5.17)$$

where $\underline{\Delta P}$ refers to the entire right hand side of Eq. 5.15. The evaluation of the integral defining the inelastic load vector is based on a Gaussian quadrature formula. Typically, 4-6 iterations are required for convergence at the higher level.

The evaluation of the incremental stresses and incremental creep strains in step 2 requires the simultaneous consideration of Eq. 5.16 and Eq. 5.8. In addition to a nonlinear equation solver, a numerical time integrator is needed to obtain results. Previous investigators (Snyder and Bathe, 1981, Hughes and Taylor, 1978, and Krieg, 1977) have used a simple successive substitution type algorithm to decouple the two equations. This involves the use of incremental creep strains from iteration k to evaluate the incremental stresses for iteration k+1 using Eq. 5.16. The incremental creep strains for iteration k+1 are evaluated with the α-method of numerical time integration which expresses Eq. 5.8 as:

$$(\underline{\varepsilon}_{cr,i+1} - \underline{\varepsilon}_{cr,i}) = \lambda_\alpha \underline{S}^*_\alpha (t_{i+1} - t_i) \qquad (5.18)$$

where $\underline{S}^*_\alpha$ is a weighted average of the pseudo deviatoric stress vector in the time interval $(t_{i+1} - t_i)$ and λ_α is derived from a similar weighting on the effective stress. Since $\underline{G}$ in Eq. 5.10 is independent of time, $\underline{S}^*_\alpha$ is equal to the product of $\underline{G}$ with the weighted average of the total stress vector over the same time interval given by:

$$\underline{\sigma}_\alpha = (1-\alpha) \underline{\sigma}_i + \alpha \underline{\sigma}_{i+1} \qquad (5.19)$$

Typical values of α lie in the range zero to one. A value of α equal to zero yields the forward (explicit) Euler method, while α equal to one yields the backward (implicit) Euler method. Both these formulas are first-order accurate (for linear problems in which λ is a constant, and not dependent on the effective stress), although the actual error of the backward formula is considerably less than that of the forward formula assuming that the former is iterated up to convergence. A value of α equal to 0.5 yields the well-known trapezoidal rule, also called the improved Euler's method since it is second-order accurate. A linear stability analysis of the α-method shows that it is unconditionally stable only for α greater than or equal to 0.5.

For quasi-elastic problems in which creep deformations are not dominant, experience has shown that for small time increments $\alpha=0.5$ is more accurate, and that for large time increments $\alpha=1$ is to be preferred. However for creep dominant problems of concern here, the convergence rate slows down considerably for highly stressed elements when $\alpha=1$ is used, and more than 10 to 12 iterations may be needed for convergence at the lower-level. This is computationally unattractive since iteration is necessary at each integration point within an element (four in the case of a quadrilateral element) and highly stressed elements may occur often in a reasonably large finite element grid, e.g., consisting of 250 elements.

For accelerating solution convergence in creep dominant problems of concern here, a lower-level algorithm is developed which combines a Newton-Raphson or tangent type nonlinear equation solver with the α-method. The resulting equations are listed below (refer to Appendix E):

$$[\underline{I}+\underline{D}\frac{\partial \underline{\Delta\varepsilon}_{cr}}{\partial \underline{\sigma}^T_{i+1}}]^k \underline{\sigma}_{i+1}{}^{k+1}=\underline{\sigma}_i+\underline{D}[\underline{B}\ \underline{\Delta U}-\underline{\Delta\varepsilon}_{cr}{}^k]+\underline{D}[\frac{\partial \underline{\Delta\varepsilon}_{cr}}{\partial \underline{\sigma}^T_{i+1}}]^k \underline{\sigma}_{i+1}{}^k \tag{5.20}$$

where $\underline{\Delta\varepsilon}_{cr}{}^k$ is obtained by applying Eq. 5.18 after obtaining the stress quantities at iteration k, and similarly:

$$[\frac{\partial \underline{\Delta\varepsilon}_{cr}}{\partial \underline{\sigma}^T_{i+1}}]^k = \Delta t \ \alpha \ [\lambda \underline{G} + 3/\beta \ \ \sigma_e^{-1} \ \frac{\partial \lambda}{\partial \sigma_e} \ \underline{S}^* \ \underline{S}^{*T}]^k_\alpha \qquad (5.21)$$

For the given material model, $\partial\lambda/\partial\sigma_e$ can be obtained from Eq. 5.9. Notice that the algorithm becomes explicit for $\alpha=0$ as it should and no iteration is required. Convergence is defined to occur when the maximum absolute value of the relative change in point stresses between iteration k and k+1 is less than 0.01. Iteration is also stopped if the actual point stresses are zero at k and their maximum absolute value is less than 0.01 at k+1. Application of this iterative scheme with $\alpha=1$ shows that convergence is typically obtained in 4 iterations instead of more than 10 to 12, thereby cutting down the computational effort by approximately 50% if the increased computational effort per iteration is accounted for.

Computer Implementation and Code Verification -- The generalization of the finite element analysis algorithm for material anisotropy has been implemented in the computer code called DECNEC (Discrete Element Computational NEtwork Controller). A post-processor called ORION, originally developed at the Lawrence Livermore Laboratory, can produce graphical display of stress, strain, and strainrate contours as well as interface pressure distributions. The current implementation is a two-dimensional version for plane stress problems. A four-noded quadrilateral element is currently available. Although an eight-noded quadratic element is often preferred, accurate results can and have been obtained with the four-noded element using a finer finite element mesh.

The accuracy of the computer code for the anisotropic material model has been verified for the case of transverse isotropy through the following test problems:

(a) Constant strainrate unconfined compression tests in and transverse to the plane of isotropy.

(b) Constant stress and constant strainrate tests with boundary conditions similar to Frederking's (1977) type A tests.

(c) Pure shear test with stresses applied in the plane of isotropy.

The first test in (a) checks on the parameters a and N of the material model, while the second is a check on β_1 when it is conducted at the same strainrate. The two tests in (b) are further checks on a, N, and β_1. For an applied constant y-direction stress σ_y, a simple analysis shows that the lateral stress, σ_z, is given by (refer to Appendix F):

$$\sigma_z=-\sigma_y[\{a_2/(a_2+a_3)-\nu\}e^{-\{(a_2+a_3)/3\}E\lambda t}-a_2/(a_2+a_3)] \quad (5.22)$$

where ν is the Poisson's ratio in the plane of isotropy and E is the corresponding Young's modulus. This solution is valid for a constant value of λ, which in an average sense may be defined as its value at steady state. Under steady state conditions, i.e., large t, Eq. 5.22 shows that the lateral stress is equal to a_2/β or $1-0.5\beta_1^{-n}$ times the y-stress. Application of DECNEC verified this analysis. If the strainrate in the plane of isotropy for the second test is kept the same as that in (a), then the stress in the direction of the applied strainrate must be greater than the corresponding stress in (a) by the factor γ_z of Eq. 2.37. Note that γ_z is a function of only β_1. The pure shear test in (c) is a check on Eq. 2.35 for a_5 which is a function of only β_1 in the case of transverse isotropy. Verification is achieved by comparing the theoretical predictions for shear strains with the numerical results. The test conditions for (b) and (c) are illustrated in Fig. 5.1. No checks are needed for parameters β_4 and β_6 or a_4 and a_6 since they do not influence plane stress indentation behavior.

5.4 NUMERICAL SIMULATIONS

Description of Case Studies -- Numerical simulations are performed for the 20 cases identified in Table 5.1 based on isotropic and transversely isotropic behavior of sea ice. The first seven cases, 1 to 7, are for isotropic sea ice, where $\beta_1=1$, while the rest, 8 to 20, are for transversely isotropic sea ice with β_1 varying from 2 to 5, which are typical values of β_1 found in the field. The objectives of simulation cases 1 to 3, 8 to 10, 15 to 17, 19 and 20 are to quantify the effect of interface adfreeze and friction on predicted indentation pressures under different β_1 values. Four values of β_1 equal to 1, 2, 3 and 5 are studied. For global forces, the fixed condition provides an upper bound solution since the ice-structure interface is considered to be infinitely strong. The free condition corresponds to no adfreeze and friction,

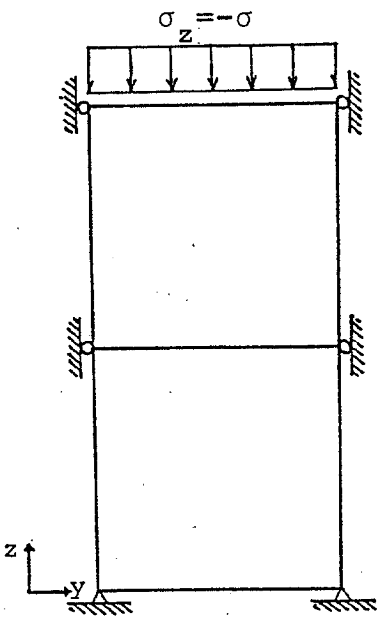

(a) Confined Test

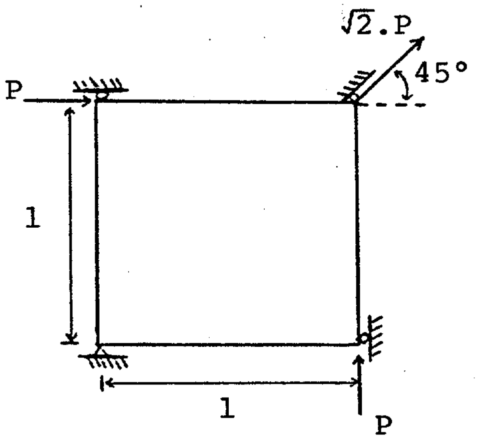

(b) Shear Test

Figure 5.1 Tests for Code Verification.

TABLE 5.1 - Summary Of Cases

Case	Velocity (ft/hr)	Diameter (ft)	N	β_1	Interface Condition
1	0.64	350	3	1	Fixed
2	0.64	350	3	1	Roller
3	0.64	350	3	1	Free
4	0.10	350	3	1	Roller
5	1.00	350	3	1	Roller
6	0.64	1000	3	1	Roller
7	0.64	350	4	1	Roller
8	0.64	350	3	3	Fixed
9	0.64	350	3	3	Roller
10	0.64	350	3	3	Free
11	0.10	350	3	3	Roller
12	1.00	350	3	3	Roller
13	0.64	1000	3	3	Roller
14	0.64	350	4	3	Roller
15	0.64	350	3	5	Fixed
16	0.64	350	3	5	Roller
17	0.64	350	3	5	Free
18	0.64	328000	3	5	Free
19	0.64	350	3	2	Fixed
20	0.64	350	3	2	Free

Note: 1 ft = 0.3048 m

while the roller condition provides an intermediate solution. The roller condition allows no normal motion of the finite element nodes at the cie-structure interface but tangential motion is not constrained. On the other hand, the free condition allows only normal compressive stresses to develop at the interface. Thus the upstream side tends to follow the roller condition and may be modelled as such. However, the interface nodes of the ice and the structure are completely disconnected if a normal stress develops. This is an adaptive process in general, but for the numerical simulations in this study it was found adequate to disconnect the downstream interface nodes to achieve the desired no-tension condition.

Simulation cases 4, 5, 11 and 12 study the influence of ice sheet velocity on pressures. The chosen base velocity of 0.195 m/hr corresponds to the recorded maximum average velocity over a twelve-hour period just prior to "breakout" (macrocracking) for an artificial island in the Beaufort Sea. This was selected in order to predict the maximum pressures that the structure will experience. The basic assumption here is that the ice pressure on the indenter will be greatest just prior to macrocrack formation or "break-out", and that ice deforms primarily in the creeping mode prior to break-out. Macrocracks and fracture processes will tend to relieve the built-up stresses.

Simulation cases 6 and 13 attempt to quantify the effect of a grounded rubble pile or an accreted ice foot on ice pressures by defining a larger effective indenter diameter (2.86 times the structural diameter). Simulation case 18 is used to check the construction of the pressure-area curve for large contact areas.

Simulation cases 7 and 14 study the effect of variability in constants a and N defining the material model on ice pressures. Two sets of the parameters a and N for sea ice based on the work of Sanderson (1984) and Wang (1982), respectively, are considered: $N=3$, $a=2.125\text{x}10^{-6}$ $(\text{MPa})^{-3}$ s^{-1}; and $N=4$, $a=1.848\text{x}10^{-6}$ $(\text{MPa})^{-4}$ s^{-1}.

The elastic constants in the plane of isotropy, which have negligible influence on the steady state solutions, are taken to be $E=9.5$ GPa and $\nu=0.33$.

Numerical Implementation -- Prior to carrying out the above studies, it is necessary to set up the finite element mesh, specify a time increment for the analysis, and define the excitation.

The finite element mesh is defined such that (i) the aspect ratio of each element is as close to one as possible, (ii) the scatter in stresses predicted by adjacent elements at their commmon boundary is less than 10%, and (iii) the boundary of the ice sheet is a circle whose extent is sufficient to simulate the infinite medium. The first criterion is maintained by the pre-processor which makes the radial length of each element equal to its arc length nearer the indenter. The second criterion is controlled by specifying the number of radial segments into which a quarter-plane may be divided. A value of nine is considered here (for an eight-noded element five or six may suffice). The last criterion is also implemented by the pre-processor which makes the radius of the circular boundary equal to 9.5 times the indenter radius. Accounting for symmetry about the z-axis, the above discretization leads to a finite element mesh with 252 elements and 285 nodal points (Fig. 5.2). The number of degrees-of-freedom is 476 for the fixed condition, 538 for the roller condition, and 540 for the free condition.

The choice of time increment is made to satisfy the conflicting requirements of accuracy and computational effort. Accuracy, in turn, is achieved by allowing sufficient time for the solution to reach steady state and by specifying a time increment that captures the variability in response prior to reaching steady state. Experience with the simulations has shown that it is appropriate to consider a time increment which makes the exponential in Eq. 5.22 equal to 10^{-3} in 20 time steps. For typical values of λ and E, the time increment is approximately 100 s.

The chosen uniform far-field velocity listed in Table 5.1 defines the excitation here, although other types of excitation such as environmental traction on the ice sheet can be handled equally well. For a given time step, the excitation is defined in terms of an imposed displacement in the z-direction at the far-field boundary nodes. This displacement value is made to increase linearly with time, consistent with the chosen uniform velocity.

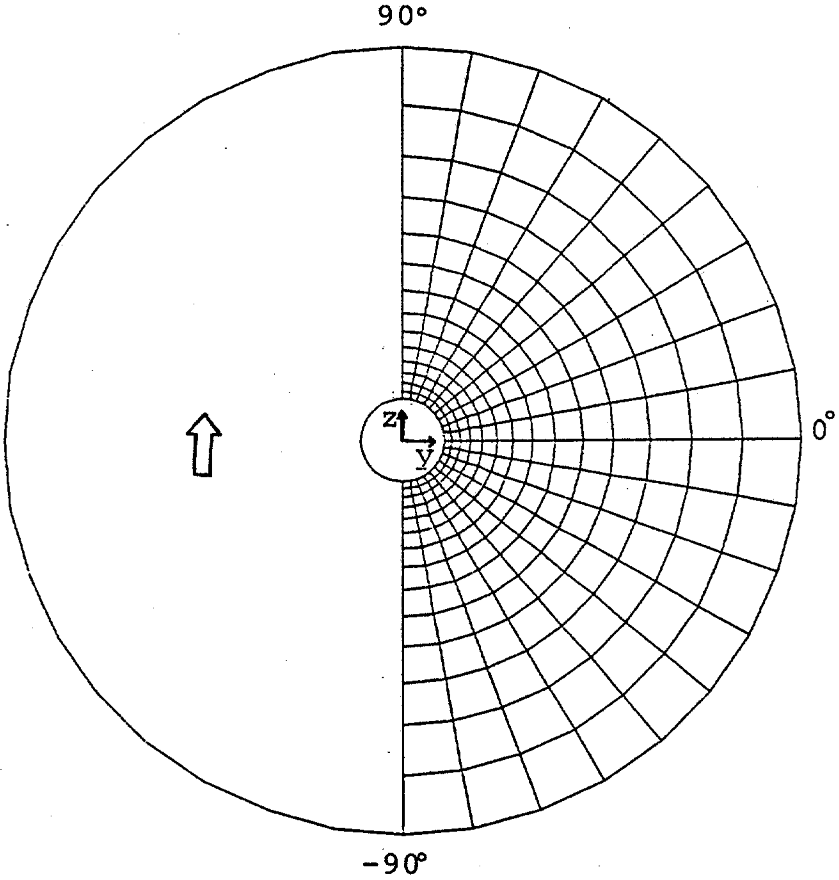

Figure 5.2 Finite Element Grid.

TABLE 5.2 - Summary Of Results

Case	P/Dt (MPa)		Maximum Interface Normal Stress (MPa)		Anisotropy/ Isotropy	
	Finite Element Analysis	Modified Upper Bound	Finite Element Analysis	Modified Upper Bound	Global Pressure	Maximum Interface Normal Stress
1	2.24	2.44	0.82	0.86	1.00	1.00
2	1.77	1.87	0.98	1.05	1.00	1.00
3	0.89	0.94	0.98	1.07	1.00	1.00
4	0.94	1.01	0.52	0.57	1.00	1.00
5	2.03	2.18	1.12	1.22	1.00	1.00
6	1.23	1.32	0.68	0.74	1.00	1.00
7	2.11	2.20	1.14	1.23	1.00	1.00
8	2.41	2.62	0.87	0.95	1.08	1.06
9	1.98	2.06	1.10	1.15	1.12	1.12
10	0.99	1.03	1.13	1.17	1.11	1.15
11	1.03	1.11	0.58	0.62	1.10	1.12
12	2.33	2.39	1.29	1.34	1.15	1.15
13	1.33	1.45	0.74	0.81	1.08	1.09
14	2.57	2.43	1.43	1.36	1.22	1.25
15	2.46	2.71	0.88	0.98	1.10	1.07
16	1.99	2.13	1.14	1.19	1.12	1.16
17	1.01	1.07	1.17	1.22	1.13	1.19
18	0.10	0.11	0.11	0.12	-	-
19	2.35	2.49	0.85	0.90	1.05	1.04
20	0.96	0.98	1.12	1.12	1.08	1.12

Note: The maximum interface shear stress for the fixed condition is 0.62 MPa for β_1, 0.60 MPa for $\beta_1=2$, 0.61 MPa for $\beta_1=3$ and 0.63 MPa for $\beta_1=5$.
1 MPa = 145 psi

5.5 DISCUSSION OF RESULTS

Global forces -- Table 5.2 lists the global pressures predicted by the finite element analysis for the 20 cases of interest. Pressure values are the global forces divided by the indenter diameter D and ice sheet thickness t. The table also lists the factor by which the global pressure increases as a result of anisotropy.

Comparing the global pressures for cases 1 to 3, 8 to 10, 15 to 17, 19 and 20, it is seen that the fixed condition does provide an upper bound to the ice global indentation pressures. The global pressure for the fixed condition is greater than that for the roller condition by a factor of about 1.22 to 1.27. In turn, the global pressure for the roller condition is 1.97 to 2.00 times that for the free condition. This spread in global pressures is indicative of the influence of interface friction and adfreeze bond. The hundred percent reduction in pressure between the roller and free case can be explained by examining the stresses within the ice sheet. For the roller case, the upstream and downstream stresses are equal in magnitude and their resultants act together in the z-direction. In the free case, the downstream stresses are almost zero since the lack of contact at the interface on this side tends to eliminate any influence of the indenter on the ice sheet. As a result, the downstream part of the ice sheet acts predominantly like a rigid body. This tends to reduce global pressures by almost a half. In the field, due to tidal movements, the downstream part is usually better simulated by the free condition.

The global pressures of cases 4, 5, 11 and 12 indicate that reducing the ice sheet velocity by a factor of 6.4 leads to a 47-48% reduction in pressures while increasing the velocity by a factor of 1.6 leads to a 15-18% increase in pressures. Thus even a factor of two uncertainty in velocity will affect the pressures by only about 20-30%.

Comparing cases 6 with 2 and 13 with 9, provide some idea of the effect of a grounded rubble pile or an accreted ice foot. The global pressures reduce by 31% to 33% when the effective indenter diameter is taken to be 2.86 times the structural diameter. However, the global force increases by a factor of 1.92 to 1.99. Two extreme scenarios can be considered to estimate the global force felt by the structure when there is a grounded rubble pile: (i) the entire global force is transmitted to the structure, which in turn transmits it to the foundation, and (ii) both the structure and the grounded rubble pile resist the global force, each transmitting to the foundation a force proportional to its contact area with the foundation. Under the first scenario, which is probably overconservative, the global force on the structure is 97% to 99% greater than that without any rubble pile. Under the second scenario, which may be reasonable only if the rubble pile is consolidated and grounded firmly in the foundation soil such as in the case of constructed ice packs, the global force on the structure is only about 25% of that without the rubble pile. This explains why constructed ice packs serve to reduce ice force acting on the structure. The results for the transversely isotropic material are identical to that from the isotropic analysis, although the absolute value of the global force for the anisotropic case is greater than that for the isotropic case by a factor of 1.12.

Cases 7 and 14 show that for β_1 equal to 1 (isotropic) and 3, the two sets of values for the material constants a and N lead to ice pressures for the roller condition which differ by a factor of 1.19 and 1.30, respectively. However for N=3 and the corresponding a, and β_1 varying between 1 and 5 (cases 1 to 3, 8 to 10, 15 to 17, 19 and 20), global ice pressures vary by a factor of 1.10, 1.12, and 1.13 for the fixed, roller and free conditions, respectively. This indicates that the degree of anisotropy β_1 is approximately two to three times less important than the actual values of a and N.

Calibration with Approximate Solutions -- The global pressures for cases 4 through 7 indicate the influence of ice sheet velocity U, indenter diameter D, and material constants a and N on the results. In order to provide perspective and calibration with solutions based on approximate methods of analysis, the upper bound solution presented earlier corresponding to a two-dimensional velocity field obtained by superposing a uniform flow and a doublet, is considered. The resulting kinematic model resembles the flow of an infinite ice sheet past a circular indenter with the interface matching most the roller condition. According to the solution, the global pressure is proportional to $(U/D)^{1/N}$. If this variation is valid, the ratio of global pressures in cases 4 to 6 with case 2 should be 0.54, 1.16 and 0.70, respectively. The finite element analysis predicts the ratios to be 0.54, 1.17 and 0.69. For the two sets of material constants in cases 7 and 2, the approximate solution predicts a ratio of 1.17 while the finite element analysis predicts a ratio of 1.19. In all cases, the effect of changes in U, D, a and N on the finite element solutions is almost identical to that predicted by the upper bound, creep law solution. This suggests that the form of the upper bound solution for predicting global pressures is valid.

The approximate upper bound formula may be expressed as given below (refer to Appendix D for a detailed derivation):

$$\frac{P}{Dt} = \Theta(\beta_1)\ \Gamma_p(\beta_1)\ \frac{4\pi}{\sqrt{3}}\ \frac{N}{N+3}\ \left[\frac{4}{\sqrt{3}}\ \frac{1}{a}\ \frac{2U}{D}\right]^{1/N} \tag{5.23}$$

where P is the global force, U is the ice sheet velocity, and Γ_p is the theoretically obtained ratio of global pressures for the anisotropic and isotropic cases which is a function of only β_1, i.e.,

$$\Gamma_p = \frac{\beta_1}{[(4\beta_1^n - 1)/3]^{1/n}} \tag{5.24}$$

where $n=2N/(N+1)$. Note that $\Gamma_p=1$ under isotropic conditions, i.e., $\beta_1=1$, and that $\Gamma_p=(3/4)^{1/n}$ as $\beta_1\rightarrow\infty$. For $2.5<N<4$, this asymptotic value varies between 0.818-0.835. A fraction equal to 98.5% of the asymptotic value is reached at $\beta_1=5$. The factor Θ is used to modify the upper bound solution, which corresponds to a plane strain condition as a result of the two-dimensional kinematic field selected, in order to be able to apply it under plane stress conditions. Ponter et al.'s (1983) analysis for both plane strain and plane stress based on the reference stress method can be used to derive the factor by which to divide the approximate solution for applying it under plane stress conditions. Ponter et al.'s analysis yields $\Theta=0.5$ for the isotropic case. On the other hand as $\beta_1\rightarrow\infty$, i.e., the material becomes infinitely strong transverse to the plane of isotropy, the difference between the plane strain and plane stress conditions disappears. Thus, the ratio of the global pressures at these two extremes of anisotropy is equal to $\Theta_\infty(3/4)^{1/n}/0.5$, which for $N=3$ is $1.65\Theta_\infty$ and for $N=4$ is $1.67\Theta_\infty$. Table 5.2 shows that case 11 with $N=3$ and $\beta_1=5$ predicts the ratio of global pressures to be 1.124 which suggests that $\Theta_\infty\simeq0.69$. The variation of Θ with β_1 may be expressed as:

$$\Theta = 0.69 - 0.19\exp[-0.7(\beta_1-1)] \qquad (5.25)$$

Table 5.2 shows that the predictions based on Eqs. 5.23 to 5.25 differ from the finite element solutions by less than 10%. The fixed condition is obtained by multiplying Eq. 5.23

by 1.27, while the free condition uses a multiplying factor of 0.5 (Table 5.3).

Local Pressures -- The maximum (peak) interface normal stress for each of the twenty simulations is listed in Table 5.2. The table also lists the maximum interface shear stress for the fixed cases. There are no interface shear stresses for the roller and free cases. Notice that in all cases the maximum normal pressure is approximately 0.36 to 1.16 times the global pressure, and not several (e.g., three) times the global pressure.

The maximum normal stress for the fixed condition is lower than that for the roller condition by 16% to 23%, although a reverse trend is observed for global pressures. This occurs because part of the force in the fixed condition is carried by interface shear stress. On the other hand, the maximum normal stress for the free condition is about zero to three percent higher than that for the roller condition. There are no interface stresses on the downstream side for the free condition due to lack of contact between the ice sheet and the indenter. The small level of stresses that exist in the predominantly rigid continuum on the downstream side are transmitted to the structure from the upstream side, thereby increasing the normal stresses on that side by the zero to three percent mentioned above.

Comparison of the local and global pressures shows that

TABLE 5.3 - Multiplying Factors For Approximate Model (Eq. 5.23)

Condition	Global Pressures	Maximum Interface Normal Stress
Roller	1.00	0.56
Fixed	1.27	0.46
Free	0.50	0.57

Note: Factor for Maximum Interface Shear Stress in Fixed Condition = 0.33

the ratio of the maximum normal interface stress to the global pressure is approximately 0.36 for the fixed condition, 0.56 for the roller condition, and 1.14 for the free condition. Furthermore, the variation of local pressures with U, D, a and N is similar to that for global pressures. Thus multiplication of Eq. 5.23 by 0.46, 0.56, and 0.57 can be used to estimate the respective maximum normal pressures (Table 5.3). In a similar fashion, the maximum interface shear stress for the fixed condition may be estimated from the equation with a multiplication factor of 0.33.

For purposes of design it is necessary to consider not only the maximum values of normal stress but also its distribution on the structure. The design of individual structural components is typically based on a tributary loaded area. It is possible that the average integrated stress on this area due to contact with the ice sheet is significantly less than the point maxima of stress. Further, the average stress may reduce for structural components which have larger tributary areas. Figures 5.3 and 5.4 present the normal stress distributions on the interface for the isotropic cases. Note that the normal stresses are always zero where the indenter is tangential to the direction of ice sheet movement (i.e., angle equal to zero degrees). At the end of the first time step where the solution is predominantly elastic, the distributions are cosinusoidal as one may expect. However as

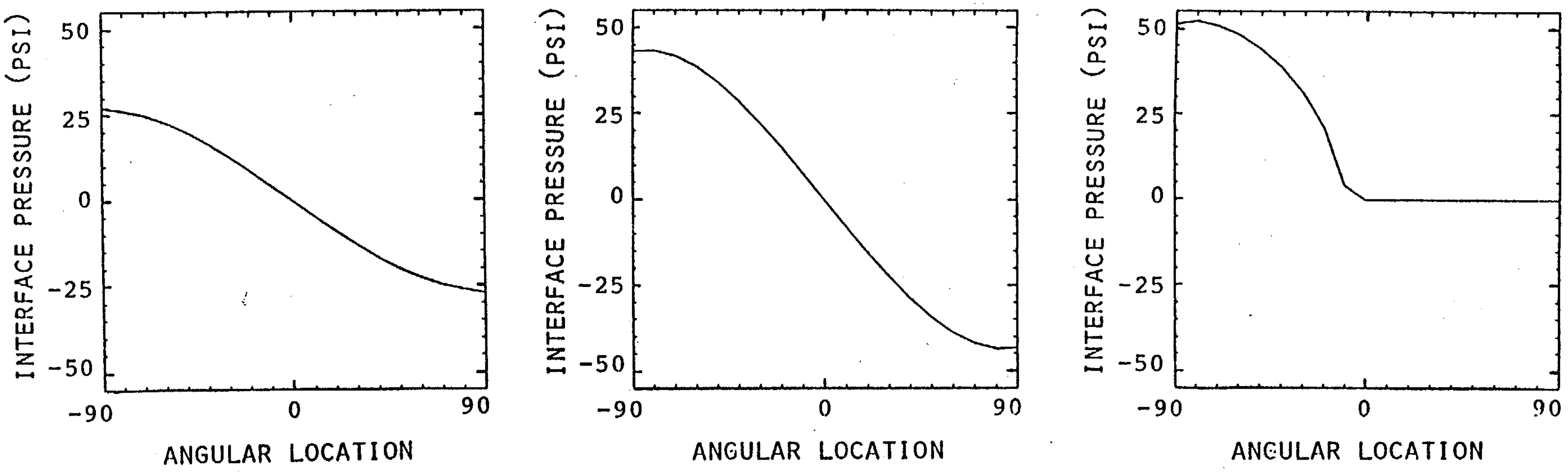

(a) Fixed Condition

(b) Roller Condition

(c) Free Condition

Figure 5.3 Normal Stress Distribution on Interface at Time Step 1 for $\beta_1 = 1$.

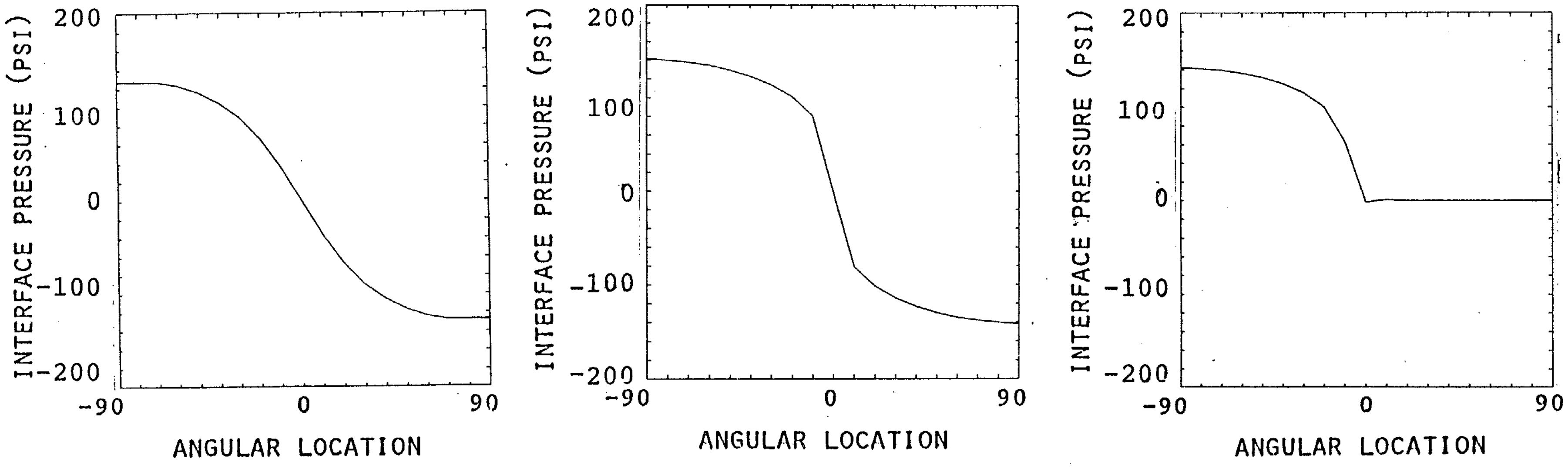

(a) Fixed Condition

(b) Roller Condition

(c) Free Condition

Figure 5.4 Normal Stress Distribution on Interface at Steady State for $\beta_1 = 1$.

steady state is reached, there is a tendency for the distributions to become rectangular or uniform. The distribution is more rectangular for the free and roller conditions than for the fixed condition which appears to be predominantly cosinusoidal due to lower stress levels, as well as for the N=4 case than for the N=3 case since an increasing value of N makes the ice behave more like a rigid-plastic material. The figures also show that downstream interface stresses are zero for the free condition. The distributions are not affected, at least visually, as U, D, N and β_1 are varied, although they have to be scaled according to the maximum normal stresses in Table 5.2. A conservative design approach may be to assume a uniform distribution of stresses based on the maximum normal interface stress. The normal stress distributions on the interface corresponding to $\beta_1=5$ is presented in Fig. 5.5, which shows that the stress distributions are very similar to the isotropic cases.

A careful consideration of the interface stress levels sheds some light on which of the three conditions, fixed, roller or free, is realistic. Figure 5.6 shows the distribution of interface shear stresses for the fixed condition. At steady state, the distribution is predominantly sinusoidal with the maximum value of 0.62 MPa occurring at the tangent point. The shear strength of adfreeze bond and sea ice as reported in the literature (Gershunov, 1984, and

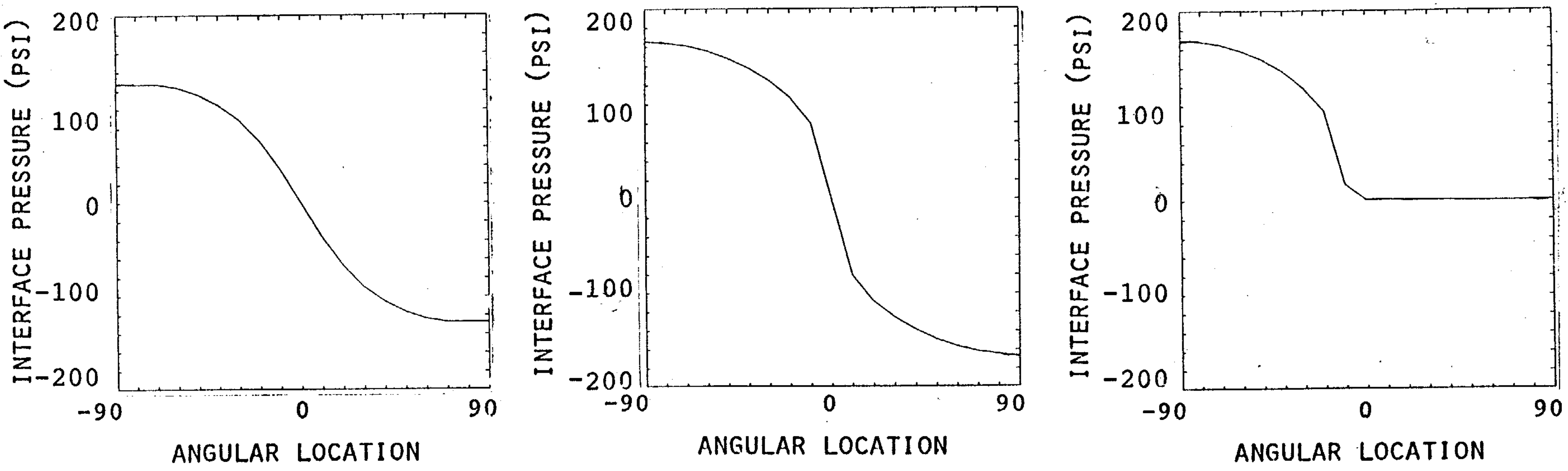

(a) Fixed Condition

(b) Roller Condition

(c) Free Condition

Figure 5.5 Normal Stress Distribution on Interface at Steady State for $\beta_1 = 5$.

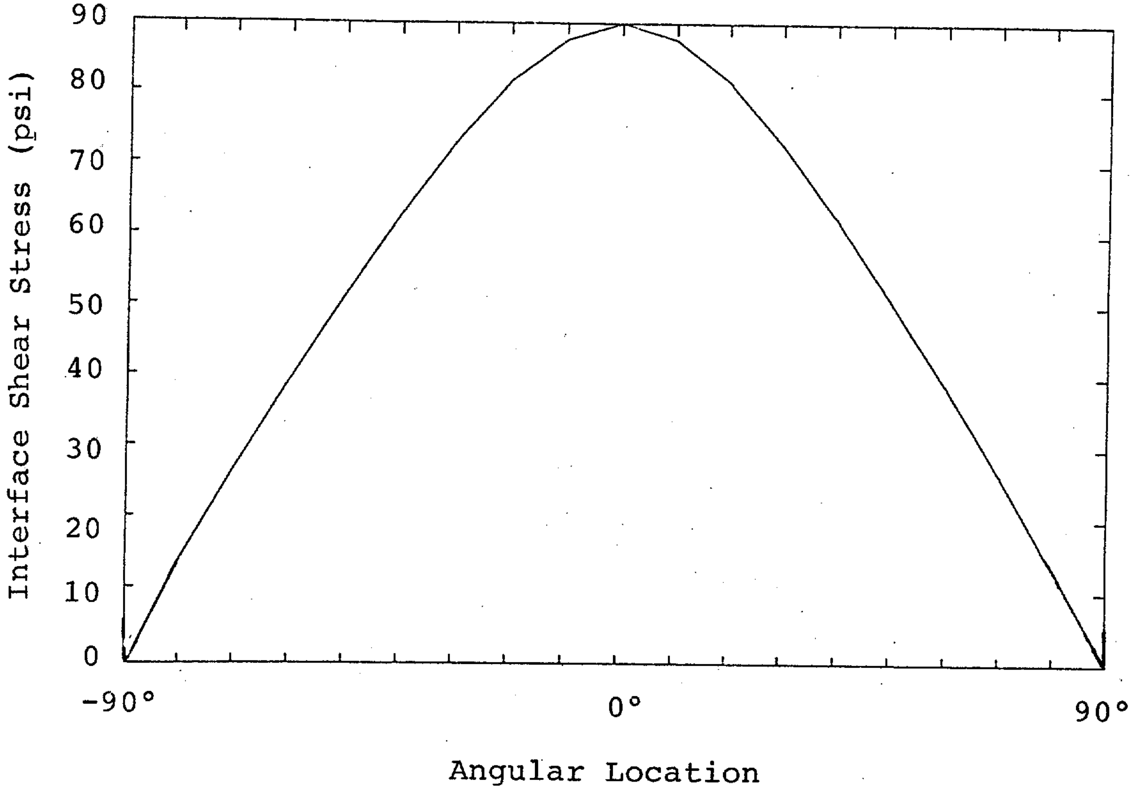

Figure 5.6 Shear Distribution on Interface for Fixed Condition at Steady State for β_1=1.

Oksanen, 1981,1983) varies over a wide range 0.02-1.38 MPa. It is very likely that either the adfreeze bond will give way or the ice will fracture in shear over a significant fraction of the indenter perimeter. In addition, for the typical range of effective strainrates close to the downstream tip of the indenter, the tensile strength of ice is less than the downstream normal interface stresses for the fixed and roller conditions, both of which are tensile. Once again, if the adfreeze bond does not give way, a tensile fracture may occur in the ice over the perimeter close to the interface on the downstream side. Thus, for local pressures the use of the free condition should be preferred. The choice will be conservative over the fixed condition and, marginally so, over the roller condition. However, the free condition may be unconservative for global pressures if the indentation problem is one in which the structure is surrounded by an infinite ice sheet and it is possible for frictional stresses or adfreeze bond to develop at the interface.

Comparison with Pressure-Area Curves -- Pressure-area curves are often constructed to help designers obtain the average pressures over tributary loaded areas for structural components (Bruen et al., 1982). A typical curve developed by Sanderson (1984b) is shown in Fig. 5.7. The darkly shaded areas on the figure correspond to actual measurements of ice pressure under widely varying conditions, while the lightly

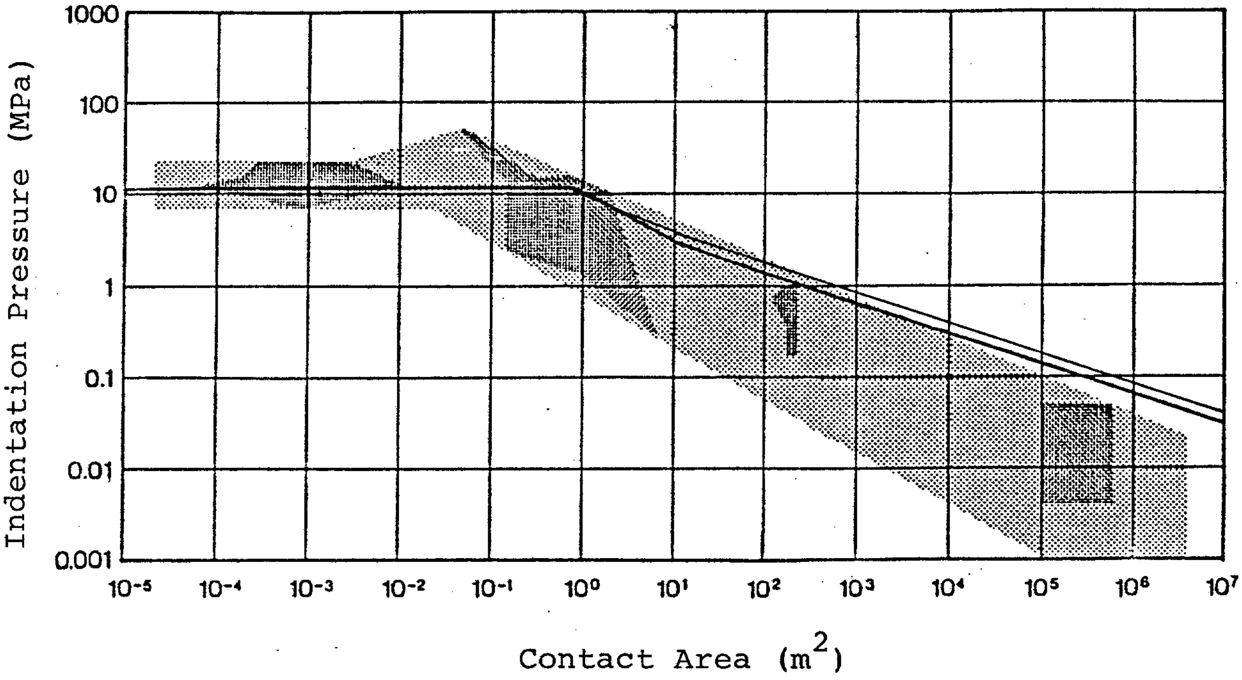

Figure 5.7 Pressure-Area Curve.

shaded areas represent Sanderson's extrapolation of the measurements. The dark regions in the extreme left are from laboratory indentation tests such as those of Frederking and Gold (1975), and Michel and Toussaint (1977). The central region reflects measurements from ice breakers traveling in the Arctic, while the two smaller regions on the right correspond to global forces on artificial islands estimated from pressure sensor measurements in the ice sheet. The contact area is defined as the indenter area of contact for the laboratory and artificial island data. For the ice breaker data, the contact area is the local area over which the pressure measurement is made and not the form area of the ice breaker. This figure shows that for an artificial island with a contact area of 200 m^2, the indentation pressure may be around 1 MPa. However for a local area of 10 m^2 on the same structure, the indentation pressure may be around 3 MPa.

The local to global pressure ratio of three obtained from the pressure-area curve seems to contradict the findings in the previous subsection. Fortunately, this is not so. If the contact area in Fig. 5.7 is interpreted as Dt, then a smaller contact area implies a smaller indenter diameter if the ice thickness remains unchanged. The effect of indenter diameter is well modelled by Eq. 5.23. A plot of the maximum normal interface pressure estimate from the equation, under free interface conditions and assuming isotropy with N=3, leads to the lower solid line in the figure. Equation 5.23 is appropriately modified to account for transition from plane stress to plane strain using Ponter et al.'s reference stress method (1983). This affects the curve, in an insignificant manner, over the region 1-10 m^2. When the effective strainrate, i.e., $(8/\sqrt{3})U/D$, exceeds 5×10^{-4} s^{-1}, ice is assumed to have fractured (crushed) and the uniaxial strength is capped at 5.9 MPa, leading to the flat portion of the curve on the extreme left. The predicted behavior provides an excellent match to Fig. 5.7. Thus, a more appealing interpretation of the figure is to consider the contact area as the indenter area (Dt in our case) and not the tributary loaded area for a structural component, and the indenter pressure corresponding to a given contact area as the maximum normal interface pressure for that indenter. The distribution of the interface stresses may be assumed uniform over the indenter area of contact as concluded earlier. However, a different boundary value problem involving a smaller contact area, as opposed to contact over half the perimeter in the free condition may lead to interface pressures that differ from the current prediction.

The upper solid line corresponds to an extreme level of anisotropy, i.e., $\beta_1=5$. For contact areas greater than 10 m^2 where plane stress conditions exist, the two lines only differ by a factor of 1.2.

The key assumption in generating the analytical curve in Fig. 5.7 concerns the choice of U. The value of 0.195 m/hr considered here is based on data for an artificial island just prior to "breakout" or macrocracking, which leads to an excellent match between predicted and measured indentation pressures for the structure. However, significantly higher velocities do occur in the field for which the current predictive models based purely on a continuum orthotropic power-law creep model will lead to increasing pressures. Fracture in ice will be the key mechanism that limits pressures generated under higher velocities.

Multiaxial Behavior of Ice Sheet -- A study of the multiaxial behavior of an ice sheet during indentation in the creeping mode provides clues to likely failure modes, particularly fracture. Most forms of fracture (crushing, spalling, splitting) initiate as a result of tensile strains perpendicular to the crack direction. Even if the applied loads at the element level are not tensile, it is possible for tensile conditions to occur in a rotated frame of reference, e.g., a 45° rotation in the case of pure shear.

Stress contours identifying the compression-compression, compression-tension, and tension-tension regions in the ice sheet are generally similar for both the isotropic and anisotropic material models, i.e., (a) tensile stresses occur almost all over the ice sheet, (b) the compression-compression region on the upstream side is much smaller for the free condition than for the fixed condition, and (c) under free interface conditions the relatively small downstream stresses are predominantly tension-tension. The biaxial stress state at the first time step is compression-tension for all the cases except for the fixed condition where it is compression-compression. As creep starts to dominate, all the cases tend to compression-compression. Figures 5.8 and 5.9 show, for the isotropic model, how this compression-compression region grows in time for the fixed and free cases. The region is much larger for the fixed condition than for the free condition. The roller condition is somewhere in between although it resembles more the free condition. Biaxial tension tends to occur on the downstream side, while compression-tension states of stress are present on both sides. Figures 5.10 and 5.11 show that increasing anisotropy, i.e., β_1, leads to increasing compression-compression and tension-tension regions. Experimental evidence for compression-tension states of stress (Haynes, 1973) shows that the occurrence of even small tensile stresses weakens ice considerably, leading to premature fracture when compared with uniaxial tensile loading.

Figure 5.12 shows the strain fields, which are more relevant to explaining fracture initiation. The strain fields also are very similar for isotropic and anisotropic material

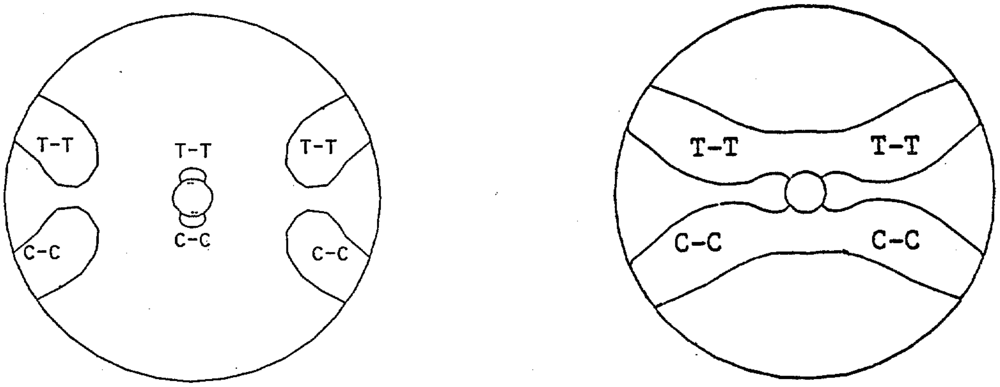
T-T
T-T
T-T
C-C
C-C
C-C
T-T
T-T
C-C
C-C

(a) Time Step 1

(b) Time Step 20

Figure 5.8 Biaxial Stress States for Fixed Condition (β_1=1)

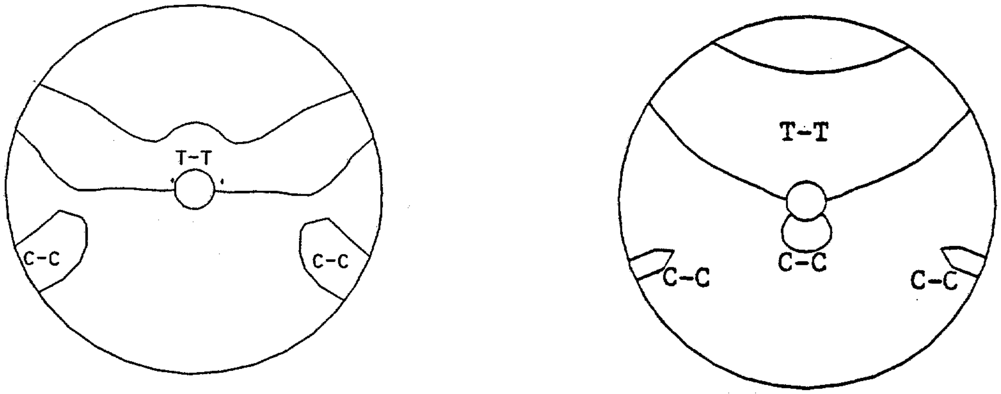
T-T
C-C
C-C
T-T
C-C
C-C
C-C

(a) Time Step 1 (b) Time Step 20

Figure 5.9 Biaxial Stress States for Free Condition (β_1=1)

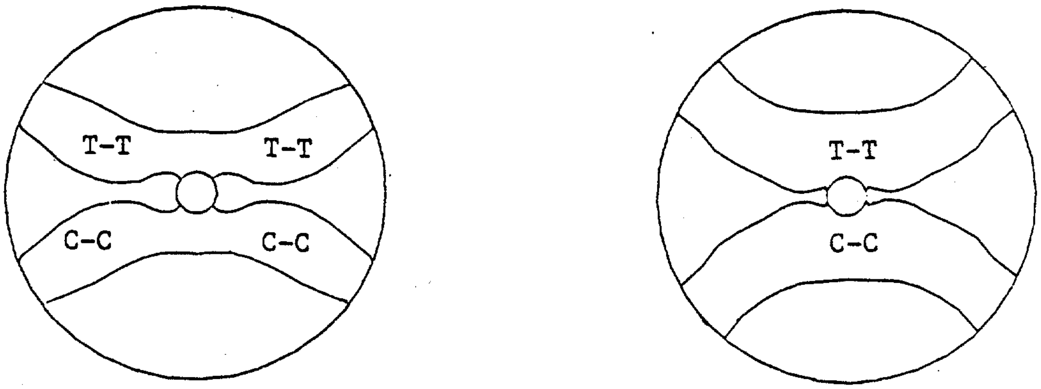
T-T
T-T
C-C
C-C
T-T
C-C

(a) Isotropic Case (β_1=1)　　(b) Anisotropic Case (β_1=5)

Figure 5.10 Biaxial Stress States at Steady State for Fixed Condition.

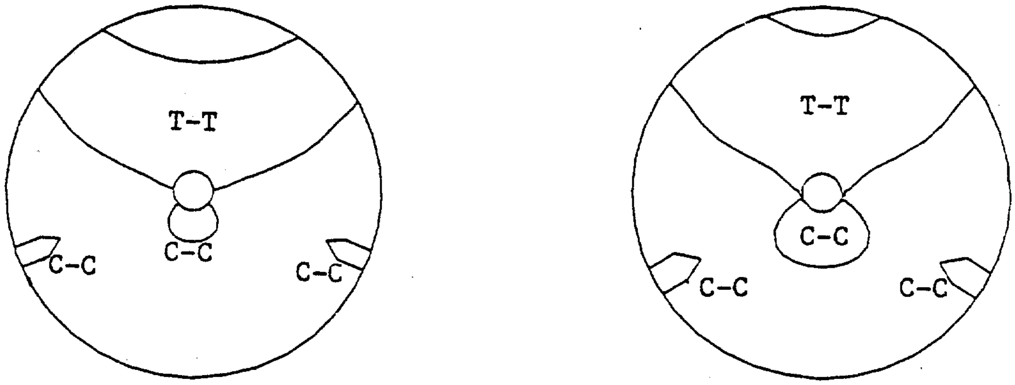
T-T
C-C
C-C
C-C
T-T
C-C
C-C
C-C

(a) Isotropic Case ($\beta_1=1$)   (b) Anisotropic Case ($\beta_1=5$)

Figure 5.11 Biaxial Stress States at Steady State for Free Condition.

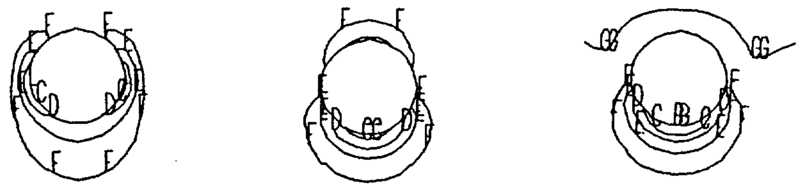

(i) Isotropic Case (β_1=1)

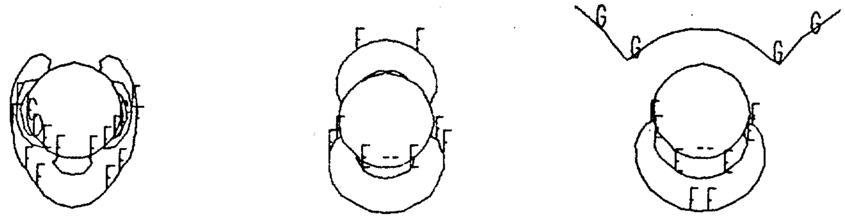

(ii) Anisotropic Case (β_1=5)

(a) Fixed Case (b) Roller Case (c) Free Case

Contour Levels
A = -0.0030
B = -0.0025
C = -0.0020
D = -0.0015
E = -0.0010
F = -0.0005
G = 1.2×10^{-10}

Figure 5.12 Minimum Principal Strain Contours (Time Step 20)

behavior. The strains are smaller as β_1 increases for the roller and free conditions but remain almost unchanged for the fixed condition. The reduction in strains is associated with the increase in lateral confinement near the upstream and downstream tips of the indenter which in turn significantly affects the behavior of transversely isotropic sea ice. Lateral confinement effects are smaller for the fixed condition since the influence of anisotropy is more evenly distributed over the interface due to the presence of interface shear stresses. The peak values of these stresses occur not at the tips but at points tangential to the direction of the ice movement. The strains are compression-tension almost everywhere on the ice sheet with tensile strains exceeding 0.001 at steady state. Since tensile failure strain for sea ice is about 0.001 or less for strainrates greater than 10^{-7} s^{-1} under just uniaxial loading, it seems likely that cracking will occur even before steady state is reached. Similar conclusions apply for the free condition, the only difference being that downstream strains are negligible.

5.6 SUMMARY

This chapter developed and applied a finite element method of analysis to study the effect of sea ice indentation in the creeping mode. Numerical simulations of ice-structure interaction for a rigid cylindrical indenter under plane stress conditions, a problem of general interest for structural concepts in the Arctic, and a transversely isotropic elastic - power law creep model for sea ice showed that:

1. Global forces vary by a factor of 2.5 depending upon whether the interface condition is fixed (infinite adfreeze bond strength), roller, or free (no adfreeze bond strength or interface friction). The fixed condition is about 1.3 times and the free condition about 0.5 times the roller condition.
2. Finite element predictions of global forces and local pressures differ from a (approximate) modified upper bound solution by less than about 10% for varying velocity, indenter diameter, and material constants.
3. Anisotropy, as represented by the stress ratio β_1 varying between 1 and 5, can cause global forces to increase by almost 15 percent depending upon whether the interface condition is fixed (infinite adfreeze bond strength), roller, or free (no adfreeze bond strength or interface friction). The factor is 1.10 for the fixed condition, 1.12 for the roller condition, and 1.13 for the free condition.
4. The ratio of maximum normal interface pressure to global pressure approximately varies in the range 0.36-1.16 depending upon the interface condition. It

is 0.36 for the fixed condition, 0.56 for the roller condition, and 1.16 for the free condition.

5. Anisotropy can cause maximum (peak) normal interface pressures to increase by almost 20 percent depending upon the interface condition. The factor is 1.07 for the fixed condition, 1.16 for the roller condition, and 1.19 for the free condition. The interface shear stress for the fixed condition essentially remains unchanged.

6. Pressure-area curves should be considered as providing the maximum normal interface pressure for a given indenter area of contact (form area), rather than the average integrated normal pressure over a tributary loaded area for a structural component. It is conservative to assume a uniform or rectangular distribution of the local pressure over the indenter area of contact for purposes of design.

7. Tensile stresses, strains and strainrates occur almost all over the ice sheet, and may be the key to explaining fracture behavior during indentation. While biaxial compression and tension states tend to occur for stress on the upstream and downstream sides, respectively, the state of strain is almost always compression-tension. The levels of tensile strain are often sufficient to cause cracking even

before steady state creep is reached.

8. Anisotropy leads to an increase in the size of the compression-compression and tension-tension states of stress on the upstream and downstream sides, respectively, of the indenter.
9. Anisotropy leads to decreasing strains for the roller and free conditions but to almost no change for the fixed condition. This is associated with the increase in lateral confinement near the upstream and downstream tips of the indenter which in turn significantly affects the behavior of transversely isotropic sea ice. Lateral confinement effects are smaller for the fixed condition since the influence of anisotropy is more evenly distributed over the interface due to the presence of interface shear stresses.

The possible effect of a grounded rubble pile or accreted ice foot on ice pressures was assessed by defining an effective indenter equal to a multiple (2.86) of the structural diameter. This resulted in a factor of 1.97 to 1.99 increase in global force. In the case of a grounded rubble pile, it would be overconservative to consider that all this force is transmitted to the foundation by the structure. On the other hand, the force transmitted to the foundation by the structure would decrease by a factor of about 4.0 if both the structure and the grounded rubble pile could transmit a force proportional to the contact area of each to the foundation. This may be reasonable only if the rubble pile is consolidated and grounded firmly in the foundation soil such as in the case of constructed ice packs.

The numerical simulations also showed that (i) even a factor of two uncertainty in velocity will affect ice pressures only by about 20-30%, (ii) variability in average material constants for an isotropic power-law creep model may yield ice pressures that vary by about 15-30%, and (iii) the uncertainties in pressures resulting from variability in the degree of anisotropy is approximately two to three times less important than the variability in the reference power-law constants, a and N. However, experimental data for sea ice strength can vary by almost a factor of five. As a result the actual variation in the power-law constant can be much higher than that considered here. Further, improved material models that include strain softening, fracture and temperature effects may have an important influence on ice pressure predictions. In particular, fracture in ice will be the key mechanism that limits ice pressures generated under the significantly higher velocities that occur in the field when compared with the value just prior to "breakout" or macrocracking considered here.

Further research is required to (a) predict the level of force that can be directly transmitted to the foundation by a rubble pile, (b) study the influence of boundary value problems other than "breakout" on pressure-area curves, and (c) study the influence of improved material models that consider damage, temperature gradients, and fracture in problems of ice-structure interaction.

CHAPTER SIX

CONCLUSIONS AND RECOMMENDATIONS FOR FUTURE RESEARCH

6.1 SUMMARY

A rate-sensitive constitutive model for describing the mechanical behavior of sea ice is developed and then applied to the study of steady indentation problems in the creeping mode. The constitutive model combines a pressure-insensitive potential function description for deriving creep deformations based on the associative flow rule and a pressure-sensitive surface to describe ultimate failure by macrocracking leading to yielding or fracture. The constitutive model is characterized by its ability to:

(a) Decompose the various recoverable and irrecoverable components of strain.

(b) Represent continuously damaging or strain-softening material behavior during ductile to brittle transition.

(c) Describe materially anisotropic material behavior.

(d) Predict first crack occurrence with a rate-dependent limiting tensile strain criterion.

A finite element method of analysis is then developed and applied to the study of sea ice indentation in the creeping mode. Numerical simulations are performed under plane stress conditions to predict the influence of (i) interface adfreeze and friction, (ii) material anisotropy, (iii) variability in parameters of the material model, (iv) rubble pile or grounded ice foot, and (v) ice sheet velocity on global forces and local pressures generated on a rigid cylindrical indenter. The results are compared with those from an approximate method of analysis based on the upper bound theorem. In the following, conclusions from the various contributions of this study are summarized:

Summary of Continuum Modeling -- A rate-sensitive damage model for describing the continuum behavior of sea ice under variable loading conditions was presented. The model, based on a nonlinear generalization of the Maxwell differential formulation, is characterized by its ability to (a) decompose the various recoverable and irrecoverable components of strain, (b) represent continuously damaging or strain-softening material behavior in the ductile to brittle transition region, (c) capture the rate-dependent behavior of sea ice with rate-independent model parameters, and (d) describe materially anisotropic mechanical behavior. Furthermore, the model shows strong dependency of the creep and constant strainrate behavior. Calibration of the model is achieved with several independent sets of data, particularly those for first-year sea ice. The following specific conclusions can be drawn:

1. The uniaxial model developed here is described by 8 parameters. For comparable models, i.e., those of Sinha and

Michel, the number of parameters is 7 and 9 respectively. It must be recognized that Sinha's model does not capture material damage with strain-softening, while calibration of Michel's model with experimental data has been very limited.

2. All parameters of the proposed model, i.e., 8 for the uniaxial model and 5 for the orthotropic generalization, can be determined from conventional tests conducted on ice. The experimental data base is generally adequate to determine the model parameters. In particular, normalization of the uniaxial strength data for salinity and temperature is a useful way of including test results for pure polycrystalline ice in model calibration.

3. Material damage that can be described by the continuum model proposed here is significant in the strainrate range of 2×10^{-4} s^{-1} to 10^{-2} s^{-1}. At higher strainrates the presence of macrocracks precludes a solely continuum description of ice behavior.

4. According to the proposed model, an ideal creep test does not lead to primary creep strains. However if the finite rise time required to reach the nominal stress in a creep test is taken into account, primary creep strains are simulated by the model. Experimental evidence appears to support this conclusion.

5. The pressure-insensitive orthotropic model proposed here predicts very well the plane strain uniaxial compression tests conducted by Frederking. Further, experimental data of

Richter-Menge et al. on first-year sea ice and that of Hausler on saline ice indicate that sea ice is only moderately pressure sensitive in comparison with pure ploycrystalline ice which is highly pressure-sensitive.

Summary of Yield and Fracture Modeling -- A rate-sensitive model in stress-strain domain for describing the macroscale fracture behavior of sea ice was dicussed. The model, unified with a rate-sensitive damage model developed for the continuum behavior of sea ice, is characterized by its ability to (a) predict first crack occurrence with a rate-dependent limiting tensile strain criterion, (b) represent fracture under multiaxial states of stress with a Drucker-Prager failure surface, and (c) distinguish the mechanisms of multiaxial flow by creep and ultimate failure by macrocracking leading to yielding or fracture. Calibration of the model is achieved with the limited existing experimental data base. The following specific conclusions can be drawn:

1. The prediction of first crack nucleation under uniaxial compressive creep conditions using a rate-dependent limiting tensile strain criterion for the lateral tensile strains arising from Poisson's effect and incompressibility of flow compares very well with the experimental data of Gold.

2. The time to first crack occurrence tends to approach zero as the uniaxial compressive stress approaches a value corresponding to fracture, i.e., 5.0 MPa. At these higher stresses, the delayed elastic strain criterion of Sinha

continues to predict longer first crack nucleation times.

3. The prediction of first crack occurrence under constant stress-rate conditions using the rate-dependent limiting tensile strain criterion agrees very well at low to intermediate stressrates with the analysis of Sanderson and Child based on the delayed elastic strain criterion. At high stressrates, the proposed model predicts a significantly lower stress for nucleation of the crack.

4. A rate-sensitive and isotropic Drucker-Prager failure surface is used to describe yield of ice under compressive states of stress and fracture of ice whenever a tensile stress is present. The constants of the model are derived from two uniaxial tests, one in tension and the other in compression. In the latter case, the compressive stress at which the first crack nucleates using the rate-dependent limiting tensile strain criterion defines the "yield" point.

5. The ratio of the yield stress in uniaxial compression to the fracture stress in uniaxial tension obtained from the Drucker-Prager formulation appears to provide the best match to data from the tensile triaxial tests of Haynes.

Summary of Approximate Analysis of Sea Ice Indentation -- The predictions of global and local indentation pressures in the creeping mode of sea ice deformation, accounting for the spatial variation of strain-rates, using the upper bound and the strain path methods, leads to the following specific conclusions:

1. Kinematic Model B, based on the superposition of a uniform flow and a doublet, models the ice movement survey data obtained from an artificial island in the Beaufort Sea than Kinematic Model A, which is based on the superposition of a uniform flow and a source.
2. The maximum strain rate for Model A occurs at the stagnation point on the ice bluff-body interface and is equal to U/r_o, while for Model B it occurs at the same point and is equal to $2U/r_o$.
3. The stress field decays as $r^{-2/N}$ for Kinematic Model A and as $r^{-3/N}$ for Model B, where N is the power-law index. The stress field is axisymmetric for Model A and not so for Model B.
4. In the creeping mode of ice deformation, the local ice pressures are of the same order of magnitude as or lower than the global pressures. The local pressures are not several times the average global pressure as is commonly believed. Even if the global pressures are reduced, e.g., by a factor of three, to account for scale (fracturing) effects, the local pressures based on the strain path method will only be 1.5 (and not three) times the upper bound global pressure neglecting interface friction.
5. Under essentially plane strain conditions, Kinematic Model B predicts global pressures that are inbetween that of the Ponter et al. model and the API model. For a typical artificial island just prior to

break-out with ice movements of less than 1 ft/hr ($85x10^{-6}$ m s^{-1}), Model B predicts a pressure (neglecting interface friction) of approximately 530 psi (3.7 MPa).

6. The global pressures predicted by the upper bound method are very sensitive to the statical traction boundary conditions at the ice-structure interface. For Kinematic Model B, assuming no friction at the interface may lead to overconservative pressure estimates.

A key finding of this study is that for the rate-dependent material models describing sea ice behavior, interface adfreeze and friction stresses can significantly influence both local and global ice pressures. This has major economic consequences for platform design. Incorporation of these "non-conservative" stresses within the bound method may yield more accurate global ice pressures, but the solutions will not necessarily be upper bounds. More exact estimates of both local and global ice pressures using the strain path method may be obtained by postulating kinematic models that more correctly model the interface conditions. However, currently available field data does not provide adequate resolution of the ice movements in the immediate vicinity of the structure to calibrate such models. In conclusion, it appears that the development of numerical models based, for example, on the finite element method of analysis is necessary for more realistically studying ice-structure interaction problems where both global and local pressures are of interest.

Summary of Finite Element Analysis of Sea Ice Indentation -- A finite element method of analysis was developed and applied to study the effect of sea ice indentation in the creeping mode. Numerical simulations of ice-structure interaction for a rigid cylindrical indenter under plane stress conditions, a problem of general interest for structural concepts in the Arctic, and a transversely isotropic elastic - power law creep model for sea ice showed that:

1. Global forces vary by a factor of 2.5 depending upon whether the interface condition is fixed (infinite adfreeze bond strength), roller, or free (no adfreeze bond strength or interface friction). The fixed condition is about 1.3 times and the free condition about 0.5 times the roller condition.
2. Finite element predictions of global forces and local pressures differ from a (approximate) modified upper bound solution by less than about 10% for varying velocity, indenter diameter, and material constants.
3. Anisotropy, as represented by the stress ratio β_1 varying between 1 and 5, can cause global forces to increase by almost 15 percent depending upon whether the interface condition is fixed (infinite adfreeze bond strength), roller, or free (no adfreeze bond

strength or interface friction). The factor is 1.10 for the fixed condition, 1.12 for the roller condition, and 1.13 for the free condition.

4. The ratio of maximum normal interface pressure to global pressure approximately varies in the range 0.36-1.16 depending upon the interface condition. It is 0.36 for the fixed condition, 0.56 for the roller condition, and 1.16 for the free condition.
5. Anisotropy can cause maximum (peak) normal interface pressures to increase by almost 20 percent depending upon the interface condition. The factor is 1.07 for the fixed condition, 1.16 for the roller condition, and 1.19 for the free condition. The interface shear stress for the fixed condition essentially remains unchanged.
6. Pressure-area curves should be considered as providing the maximum normal interface pressure for a given indenter area of contact (form area), rather than the average integrated normal pressure over a tributary loaded area for a structural component. It is conservative to assume a uniform or rectangular distribution of the local pressure over the indenter area of contact for purposes of design.
7. Tensile stresses, strains and strainrates occur almost all over the ice sheet, and may be the key to explaining fracture behavior during indentation.

While biaxial compression and tension states tend to occur for stress on the upstream and downstream sides, respectively, the state of strain is almost always compression-tension. The levels of tensile strain are often sufficient to cause cracking even before steady state creep is reached.

8. Anisotropy leads to an increase in the size of the compression-compression and tension-tension states of stress on the upstream and downstream sides, respectively, of the indenter.
9. Anisotropy leads to decreasing strains for the roller and free conditions but to almost no change for the fixed condition. This is associated with the increase in lateral confinement near the upstream and downstream tips of the indenter which in turn significantly affects the behavior of transversely isotropic sea ice. Lateral confinement effects are smaller for the fixed condition since the influence of anisotropy is more evenly distributed over the interface due to the presence of interface shear stresses.

The possible effect of a grounded rubble pile or accreted ice foot on ice pressures was assessed by defining an effective indenter equal to a multiple (2.86) of the structural diameter. This resulted in a factor of 1.97 to 1.99 increase in global force. In the case of a grounded rubble pile, it would be overconservative to consider that all this force is transmitted to the foundation by the structure. On the other hand, the force transmitted to the foundation by the structure would decrease by a factor of about 4.0 if both the structure and the grounded rubble pile could transmit a force proportional to the contact area of each to the foundation. This may be reasonable only if the rubble pile is consolidated and grounded firmly in the foundation soil such as in the case of constructed ice packs.

The numerical simulations also showed that (i) even a factor of two uncertainty in velocity will affect ice pressures only by about 20-30%, (ii) variability in average material constants for an isotropic power-law creep model may yield ice pressures that vary by about 15-30%, and (iii) the uncertainties in pressures resulting from variability in the degree of anisotropy is approximately two to three times less important than the variability in the reference power-law constants, a and N. However, it must be noted that experimental data for sea ice strength can vary almost by a factor of five. As a result the actual variation in the power-law constant can be much higher than that considered here. Further, improved material models that include strain-softening, fracture and temperature effects may have an important influence on ice pressure predictions. In particular, fracture in ice will be the key mechanism that limits ice pressures generated under the significantly higher velocities that occur in the field when compared with the value just prior to "breakout" or macrocracking considered here.

6.2 RECOMMENDATIONS FOR FUTURE RESEARCH

It is apparent from the present work that many aspects related to the prediction of global and local ice pressures acting on strutures in the Arctic need further study and verification. The following discussion focus on the areas covered in this thesis:

1. In the area of constitutive modeling, additional research is needed to resolve several questions, including (a) the presence or lack thereof of primary creep strains in ideal creep tests, (b) the possible pressure sensitivity of the damage parameter, (c) the adequacy of the incremental damage accumulation model based on Miner's rule particularly for variable loading histories, (d) the generation of hysteresis loops during unloading/reloading and cyclic loading, (e) the value of peak stress at failure in stress-strain curves obtained from tests conducted at low stressrates (i.e., lower than 0.1 MPa s^{-1}), (f) the extent of stress relaxation in sea ice, and (g) the equivalence, if any, in the triaxial behavior of pure and sea ice. Both experimental and theoretical research is very much needed to better characterize

the multiaxial behavior of sea ice particularly under cyclic loading.

2. In the area of yielding and fracture, additional research is needed to address the following concerns: (a) the influence of temperature on the fracture strength in tension and compression and the strain and strainrate at which it occurs, (b) experimental data under biaxial and triaxial loading conditions to better define the failure surface defining yield in compression and fracture in tension, and its use in the development of an orthotropic failure surface, and (c) the equivalence, if any, in the strains and triaxial behavior of pure polycrystalline ice and sea ice.
3. The deficiency of the strain path method in predicting the correct interface stresses may be improved by the used of non-ideal, viscous fluid to obtain a better approximation to the interface conditions. This would then result in better analytical predictions of the local ice pressures. The upper bound prediction of the global pressures will also improve as a result.
4. From the numerical simulations, further research is required to (a) predict the level of force that can be directly transmitted to the foundation by a rubble pile, (b) study the influence of boundary value problems other than "breakout" on pressure-area

curves, and (c) study the influence of improved material models that consider damage, temperature gradients, and fracture in problems of ice-structure interaction.

5. Several approaches are available to account for cracking in a finite element framework. Two of the more common approaches are the _discrete cracking models_ which follow individual discrete cracks between elements and the _smeared cracking models_ which treat the gross (smeared) effect of cracks in an element. The latter approach has been preferred in finite element analyses of concrete since it is computationally far more convenient. An added advantage is that smeared crack models can be extended easily to allow for an objective energy release rate criterion for fracture propagation. The resulting theory, called the blunt crack band theory, will require the development of an appropriate modification to the rate-dependent limiting tensile stress fracture criterion. A major research effort should be undertaken to (i) extend the plane stress finite element analysis computer code to incorporate smeared cracking models, and (ii) implement the constitutive model, developed in this thesis, in the program. The influence of fracture on both global forces and local pressure may then be quantified through numerical simulations.

REFERENCES

1. API Bulletin on Planning, Designing, and Constructing Fixed Offshore Structures in Ice Environments, Bul. 2N, First Edition, American Petroleum Institute Production Department, Dallas, Texas, January 1982, 49 p.

2. Task Committee on Finite Element Analysis of Reinforced Concrete Structures, "Finite Element Analysis of Reinforced Concrete," ASCE, New York, NY, 1982, 545 p.

3. Baligh, M.M., "Theory of Deep Site Static Cone Penetration Resistance," Research Report R75-56, No. 517, Department of Civil Engineering, Massachusetts Institute of Technology, Cambridge, Massachusetts, 1975, 133 p.

4. Baligh, M.M., "The Strain Path Method," Research Report R84-01, No. 761, Department of Civil Engineering, Massachusetts Institute of Technology, Cambridge, Massachusetts, January 1984, 47 p.

5. Bergdahl, L., "A Theory on the Elasticity of Sea Ice," Proceedings of the 7th International Conference on Port and Ocean Engineering under Arctic Conditions (POAC 83), Helsinki, Finland, Vol. 1, April 1983, pp. 52-68.

6. Brill, R. and Camp, P.R., "Properties of Ice," U.S. Army Snow, Ice and Permafrost Research Establishment, Research Report 68, 1961, 48 p.

7. Brown, E., "Experiments on the Strength of Ice," St. Lawrence Waterway Project, Report to the Joint Board of Engineering, Appendix F, Ottawa, 1926, 423 p.

8. Bruen, F.J., Byrd, R.C., Vivatrat, V., and Watt, B.J., "Selection of Local Design Ice Pressures for Arctic Systems," Offshore Technology Conference, OTC 4334, Houston, Texas, May 1982, pp. 417-435.

9. Bruen, F.J. and Vivatrat, V., "Ice Force Prediction Based on Strain-Rate Field," Proceedings of the Third International Offshore Mechanics and Arctic Engineering Symposium, ASME, New Orleans, Louisiana, February 12-16, 1984, pp. 275-281.

10. Butkovich, T.R., "On the Mechanical Properties of Sea-Ice," Research Report 54, U.S. Snow, Ice and Permafrost Research Establishment, Thule, Greenland, 1959.

11. Chehayeb, F.S., Ting, S-K., Shyam Sunder, S. and Connor, J.J., "Sea Ice Indentation in the Creeping Mode," Offshore Technology Conference, OTC 5056, Houston, Texas, May 1985, pp. 329-341.

12. Cherepanov, N.V., "Spatial Arrangement of Sea Ice Crystal Structure," Problemy Arktiki i Antarktiki, Vol. 38, 1971, pp. 176-181.

13. Cole, D., "The Effect of Stress Application Rate on the Creep Behavior of Polycrystalline Ice," Proceedings of the Second Symposium on Offshore Mechanics and Arctic Engineering, Houston, Texas, 1982, pp. 614-621.

14. Cole, D., "The Relationship Between Creep and Strength Behavior of Ice at Failure," Cold Regions Science and Technology, Vol. 8, 1983, pp. 189-197.

15. Cox, G.F.N., Richter-Menge, J.A., Weeks, W.F., Mellor, M. and Bosworth, H., "Mechanical Properties of Multi-Year Sea Ice, Phase I: Test Results," U.S. Army Cold Regions Research and Engineering Laboratory, CRREL Report 84-9, April 1984, 105 p.

16. Croasdale, K.R., "Ice Engineering II," Symposium on Offshore Mechanics and Cold Ocean Engineering, Calgary, Canada, 1983.

17. Croasdale, K.R., Morgenstern, N.R. and Nuttall, J.B., "Indentation Tests to Investigate Ice Pressures on Vertical Piers," Journal of Glaciology, Vol. 19, No. 81, 1977, pp. 301-312.

18. Croteau, P., "Dynamic Interactions Between Floating Ice and Offshore Structures," Report No. UCB/EERC-83/06, Earthquake Engineering Research Center, College of Engineering, University of California, Berkeley, California, May 1983, 335 p.

19. Croteau, P., Rojansky, M., and Gerwick, B.C., "Summer Ice Floe Impacts against Caisson-Type Exploratory and Production Platforms," Proceedings of the Third International Offshore Mechanics and Arctic Engineering Symposium, ASME, New Orleans, Louisiana, February 12-16, 1984.

20. Currier, J.H. and Schulson, E.M., "The Tensile Strength of Ice as a Function of Grain Size," Acta Metallurgica, Vol. 30, 1982, pp. 1511-1514.

21. Durham, W.B., Heard, H.C. and Kirby, S.H., "Deformation of Ice at Pressures to 350 MPa at 77 to 195 K," EOS, 63(45), T51B-01, 1982, 1094p.

22. Dykins, J.E., "Ice Engineering - Tensile Properties of Sea Ice Grown in a Confined System," U.S. Naval Civil Engineering Laboratory Technical Report R-689, July 1970, 57 p.

23. Frankenstein, G., and Garner, R., "Equations for Determining the Brine Volume of Sea Ice From -0.5° to -22.9°C," Journal of Glaciology, Vol. 6, No. 48, 1967, pp. 943-944.

24. Frederking, R., "Plane-Strain Compressive Strength of Columnar-Grained and Granular Snow-Ice," Journal of Glaciology, Vol. 18, No. 80, 1977, pp. 505-516.

25. Frederking, R., "Ice Engineering I," Symposium on Offshore Mechanics and Cold Ocean Engineering, Canada, 1983.

26. Frederking, R. and Gold, L.W., "Ice Forces on An Isolated Circular Pile," Proceedings of the 1st International Conference on Port and Ocean Engineering under Arctic Conditions (POAC 71), Trondheim, Norway, August 1971, pp. 73-92.

27. Frederking, R. and Gold, L.W., "Experimental Study of Edge Loading of Ice Plates," Canadian Geotechnical Journal, Vol. 12, No. 4, 1975, pp. 456-463.

28. Frederking, R.M.W., and Timco, G.W., "Mid-Winter Mechanical Properties of Ice in the Southern Beaufort Sea," Proceedings of the 6th International Conference on Port and Ocean Engineering under Arctic Conditions (POAC 81), Quebec, Canada, July 1981, pp. 225-234.

29. Frederking, R., and Timco, G.W., "Uniaxial Compressive Strength and Deformation of Beaufort Sea Ice," Proceedings of the 7th International Conference on Port and Ocean Engineering under Arctic Conditions (POAC 83), Helsinki, Finland, Vol. 1, April 1983, pp. 89-98.

30. Frederking, R.M.W. and Timco, G.W., "Measurement of Shear Strength of Granular/Discontinuous-Columnar Sea Ice," Cold Regions Science and Technology, Vol. 9, 1984, pp. 215-220.

31. Gershunov, E.M., "Shear Strength of Adfreeze Bond and Its Effect on Global Ice Load Applied to Mobile Offshore Drilling Units Under Artic Conditions," Offshore Technology Conference, OTC 4687, Houston, Texas, May 1984, pp. 357-362.

32. Glen, J.W., "The Creep of Polycrystalline Ice," Proceedings of the Royal Society of London, Ser. A, Vol. 228, No. 1175, 1955, pp. 519-538.

33. Gold, L.W., "The Cracking Activity in Ice During Creep," Canadian Journal of Physics, Vol. 38, 1960, pp. 1137-1148.

34. Gold, L.W., "The Process of Failure of Columnar-grained Ice," The Philosophical Magazine, Vol. 26, No. 2, 1972, pp. 311-328.

35. Grant, N.J., "Fracture Under Conditions of Hot Creep Rupture," Fracture - An Advanced Treatise, H. Liebowitz (Editor), Academic Press, New York, Vol. 3, 1971, pp. 483-533.

36. Hausler, F.U., "Multiaxial Compressive Strength Tests on Saline Ice with Brush-Type Loading Platens," Proceedings of the IAHR International Symposium on Ice, International Association for Hydraulic Research, Quebec, Canada, July 1981, pp. 526-539.

37. Hawkes, I. and Mellor, M., "Deformation and Fracture of Ice under Uniaxial Stress," Journal of Glaciology, Vol. 11, No. 61, 1972, pp. 103-131.

38. Haynes, F.D., "Tensile Strength of Ice under Triaxial Stresses," U.S. Army Cold Regions Research and Engineering Laboratory, CRREL Research Report 312, December 1973, 21 p.

39. Haynes, F.D., "Temperature Effect on the Uniaxial Strength of Ice," Proceedings of the 5th International Conference on Port and Ocean Engineering under Arctic Conditions (POAC 79), Trondheim, Norway, August 1979, pp. 667-681.

40. Haynes, F.D. and Mellor, M., "Measuring the Uniaxial Compressive Strength of Ice," Journal of Glaciology, Vol. 19, No. 81, 1977, pp. 213-223.

41. Hill, R., "The Mathematical Theory of Plasticity," Oxford University Press, London, 1950, 355 p.

42. Hill, R., "A General Method of Analysis for Metal-Working Process," Journal of the Mechanics and Physics of Solids, Vol. 11, 1963, pp. 305-326.

43. Hughes, T.J.R. and Taylor, R.L., "Unconditionally Stable Algorithms for Quasi-Static Elasto/Visco-Plastic Finite Element Analysis," Computer and Structures, Vol. 8, 1978, pp. 169-173.

44. Jones, S.J., "Triaxial Testing of Polycrystalline Ice," Proceedings of the Third International Conference on Permafrost, Edmonton, Alberta, Canada, July 1978, pp. 671-674.

45. Jones, S.J. "The Confined Compressive Strength of Polycrystalline Ice," Journal of Glaciology, Vol. 28, No. 98, 1982, pp. 171-177.

46. Karr, D.G., and Das, S.C., "Ice Strength in Brittle and Ductile Failure Modes," Journal of Structural Engineering, ASCE, Vol. 109, No. 12, December 1983, pp. 2802-2811.

47. Karr, D.G., "Applications of Continuous Damage Models in Ice Mechanics," Proceedings, Fourth International Conference on Applied Numerical Modeling, Taiwan, December 1984.

48. Karr, D.G., "A Damage Mechanics Model for Uniaxial Deformation of Ice," Proceedings, Fourth International Symposium on Offshore Mechanics and Arctic Engineering, Dallas, Texas, February 1985.

49. Karr, D.G., "Constitutive Equations for Ice as a Damaging Material," Proceedings, ASCE Speciality Conference: ARCTIC '85 -Civil Engineering in the Arctic Offshore, San Francisco, California, March 1985.

50. Kivisild, H.R., "Ice Mechanics," Proceedings of the 3rd International Conference on Port and Ocean Engineering under Arctic Conditions (POAC 75), University of Alaska, Fairbanks, Alaska, August 1975, pp. 287-313.

51. Korzhavin, K.N., "Action of Ice on Engineering Structures," U.S. Army cold Regions Research and Engineering Laboratory, CRREL Translation TL260, 1962.

52. Kovacs, A. and Morey, R.M., "Investigations of Sea Ice Anisotropy, Electromagnetic Properties, Strength, and Under-Ice Current Orientation," CRREL Research Report 80-20, U.S. Army Cold Regions Research and Engineering Laboratory, Hanover, New Hampshire, 1980, 18 p.

53. Krieg, R.D., "Numerical Integration of Some New Unified Plasticity-Creep Formulations," 4th International Conference on Structural Mechanics in Reactor Technology (SMIRT-4), San Francisco, Paper No. M6/4, August 1977, 12 p.

54. Kry, P.R., "A Statistical Prediction of Effective Ice Crushing Stresses on Wide Structures," 5th International Symposium on Ice Problems, International Association for Hydraulic Research, Lulea, Sweden, August 1978, pp. 33-47.

55. Kry, P.R., "Scale Effects in Continuous Crushing of Ice," Proceedings of the IAHR International Symposium on Ice, International Association for Hydraulic Research, Quebec, Canada, July 1981, pp. 565-580.

56. Langhorne, P.J., "Crystal Alignment in Sea Ice," Ph.D. Thesis, University of Cambridge, U.K., 1982.

57. Langhorne, P.J., "Laboratory Experiments on Crystal Orientation in NaCl Ice," Annals of Glaciology, Vol. 4, 1983, pp. 163-169.

58. Mellor, M., "Mechanical Properties of Polycrystalline Ice," Proceedings, IUTAM Symposium on Physics and Mechanics of Ice, Copenhagen, 1979, P. Tryde (Ed.), Springer-Verlag, Berlin, 1980, pp. 117-128.

59. Mellor, M., "Mechanical Behavior of Sea Ice," U.S. Army Cold Regions Research and Engineering Laboratory, CRREL Monograph 83-1, June 1983, 105 p.

60. Mellor, M. and Cole, D., "Cyclic Loading and Fatigue in Ice," Cold Regions Science and Technology, Vol. 4, 1981, pp. 41-53.

61. Mellor, M. and Cole, D., "Deformation and Failure of Ice Under Constant Stress or Constant Strain-Rate," Cold Regions Science and Technology, Vol. 5, 1982, pp. 201-219.

62. Mellor, M. and Cole, D., "Stress/Strain/Time Relations for Ice Under Uniaxial Compression," Cold Regions Science and Technology, Vol. 6, 1983, pp. 207-230.

63. Meyers, M.A. and Chawla, K.K., "Mechanical Metallurgy -Principles and Applications," Prentice-Hall Inc., Englewood Cliffs, New Jersey, 1984, 761 p.

64. Michel, B., "Ice Mechanics," Les Presse De L'Universite Laval, Quebec, 1978, 499 p.

65. Michel, B., "Advances in Ice Mechanics," Proceedings of the 6th International Conference on Port and Ocean Engineering under Arctic Conditions (POAC 81), Universite Laval, Quebec, Canada, July 1981, pp. 189-204.

66. Michel, B. and Toussaint, N., "Mechanisms and Theory of Indentation of Ice Plates," Journal of Glaciology, Vol. 19, No. 81, 1977, pp. 285-300.

67. Morland, L.W., "Constitutive Laws for Ice," Cold Regions Science and Technology, Vol. 1, 1979, pp. 101-108.

68. Morland, L.W. and Spring, U., "Viscoelastic Fluid Relation for the Deformation of Ice," Cold Regions Science and Technology, Vol. 4, 1981, pp. 255-268.

69. Nawwar, A.M., Nadreau, J.P. and Wang, Y.S., "Triaxial Compressive Strength of Saline Ice," Proceedings of the 7th International Conference on Port and Ocean Engineering under Arctic Conditions (POAC 83), Helsinki, Finland, Vol. 3, April 1983, pp. 193-202.

70. Oksanen, P., "Friction and Adhesion of Ice," Proceedings of the IAHR International Symposium on Ice, International Association for Hydraulic Research, Quebec, Canada, July 1981, pp. 628-640.

71. Oksanen, P., "Adhesion Strength of Ice," Proceedings of the 7th International Conference on Port and Ocean Engineering under Arctic Conditions (POAC 83), Helsinki, Finland, Vol. 2, April 1983, pp. 710-719.

72. Paige, R.A., and Lee, C.W., "Preliminary Studies on Sea Ice in McMurdo Sound, Antarctica, During "Deep Freeze 65"," Journal of Glaciology, Vol. 6, No. 46, 1967, pp. 515-528.

73. Palmer, A.C., "Creep-Velocity Bounds and Glacier-Flow Problems," Journal of Glaciology, Vol. 6, No. 46, 1967, pp. 479-488.

74. Palmer, A.C., Goodman, D.J., Ashby, M.F., Evans, A.G., Hutchinson, J.W., and Ponter, A.R.S., "Fracture and Its Role in Determining Ice Forces on Offshore Structures," Symposium on Applied Glaciology, Hanover, New Hampshire, August 1982, and Annals of Glaciology, Vol. 4, 1983, pp. 216-221.

75. Panov, V.V., and Fokeev, N.V., "Compression Strength of Sea Ice Specimens under Complex Loading," Problemy Arktiki i Antarktiki, Vol. 49, 1977, pp. 81-86 (English Translation, pp. 97-104).

76. Peyton, H.R., "Sea-Ice Strength," Research Report No. UAG R-182, University of Alaska, Geophysical Institute, 1966.

77. Peyton, H.R., "Ice and Marine Structures," Ocean Industry, Vol. 3, No. 3, March 1968, pp. 40-41; Vol. 3, No. 9, September 1968, pp. 59-65; Vol. 3, No. 12, December 1968, pp. 51-58.

78. Ponter, A.R.S., Palmer, A.C., Goodman, D.J., Ashby, M.F., Evans, A.G., and Hutchinson, J.W., "The Force Exerted by A Moving Ice Sheet on An Offshore Structure: Part I - The Creep Mode," Cold Regions Science and Technology, Vol. 8, 1983, pp. 109-118.

79. Ralston, T.D., "An Analysis of Ice Sheet Indentation," 5th International Symposium on Ice Problems, International Association for Hydraulic Research, Lulea, Sweden, August 1978, pp. 13-31.

80. Ralston, T.D., "Sea Ice Loads," Technical Seminar on Alaskan Beaufort Sea Gravel Island Design presented by Exxon Company, U.S.A., Houston, Texas, October 1979.

81. Ralston, T.D., "Yield and Plastic Deformation in Ice Crushing Failure," Sea Ice Processes and Models (edited by R.S. Pritchard), University of Washington Press, 1980, pp. 234-245.

82. Ralston, T.D., "Plastic Limit Analysis of Ice Splitting Failure," Proceedings of the 6th International Conference on Port and Ocean Engineering under Arctic Conditions (POAC 81), Universite Laval, Quebec, Canada, July 1981, pp. 205-215.

83. Reinicke, K.M. and Ralston, T.D., "Plastic Limit Analysis with an Anisotropic, Parabolic Yield Function," International Journal of Rock Mechanics, Mining Sciences and Geomechanics, Vol. 14, 1977, pp. 147-154.

84. Reinicke, K.M. and Remer, R., "A Procedure for the Determination of Ice Forces - Illustrated for Polycrystalline Ice," 5th International Symposium on Ice Problems, International Association for Hydraulic Research, Lulea, Sweden, August 1978, pp.217-238.

85. Richter-Menge, J.A., Cox, G.F.N., Perron, N., Durell, G. and Bosworth, H.W., "Triaxial Testing of First-Year Sea Ice," Internal Research Report 877, U.S. Army Cold Regions Research and Engineering Laboratory, Hanover, New Hampshire, 1985.

86. Saeki, H., Nomura, T. and Ozaki, A., "Experimental Study on the Testing Methods of Strength and Mechanical Properties of Sea Ice," 5th International Symposium on Ice Problems, International Association for Hydraulic Research, Lulea, Sweden, August 1978, pp. 135-149.

87. Sanderson, T.J.O., "Theoretical and Measured Ice Forces on Wide Structures," Proceedings of the 7th International Symposium on Ice, International Association for Hydraulic Research, Hamburg, August 1984, 32 p.

88. Sanderson, T.J.O., BP Development, London, Personal Communications, 1984.

89. Sanderson, T.J.O. and Child, A.J., "Ice Loads on Offshore Structures: The Transition from Creep to Fracture," 1984, 8 p.

90. Schulson, E.M., "An Analysis of the Brittle to Ductile Transition in Polycrystalline Ice Under Tension," Cold Regions Science and Technology, Vol. 1, 1979, pp. 87-91.

91. Schulson, E.M., Personal Communications, 1984.

92. Schulson, E.M. and Cannon, N.P., "The Effect of Grain Size on the Compressive Strength of Ice," IAHR Ice Symposium, International Association for Hydraulic Research, Hamburg, August 1984, pp. 29-38.

93. Schulson, E.M., Lim, P.N. and Lee, R.W., "A Brittle to Ductile Transition in Ice Under Tension," Philosophical Magazine A, Vol. 49, No. 3, 1984, pp. 353-363.

94. Schwarz, J. and Weeks, W.F., "Engineering Properties of Sea Ice," Journal of Glaciology, Vol. 19, No. 81, 1977, pp. 499-531.

95. Shapiro, L.H., "Development of Hardware and Procedures for In-Situ Measurement of Creep in Sea Ice," OCSEAP Annual Report, Research Unit 265, Contract No. 03-5-022-55, March 1978.

96. Shyam Sunder, S. and Ting, S-K., "Ductile to Brittle Transition in Sea Ice under Uniaxial Loading," Proceedings of the 8th International Conference on Port and Ocean Engineering under Arctic Conditions, Narssarssuaq, Greenland, September 1985, 12 p.

97. Sinha, N.K., "Rheology of Columnar-grained Ice," Experimental Mechanics, Vol. 18, No. 12, December 1978, pp. 464-470.

98. Sinha, N.K., "Grain Boundary Sliding in Polycrystalline Materials," Philosophical Magazine A, Vol. 40, No. 6, 1979, pp. 825-842.

99. Sinha, N.K., "Comparative Study of Ice Strength Data," Proceedings of the IAHR International Symposium on Ice, International Association for Hydraulic Research, Quebec, Canada, July 1981, pp. 581-595.

100. Sinha, N.K., "Delayed Elastic Strain Criterion for First Cracks in Ice," IUTAM Symposium on Deformation and Failure of Granular Materials, Delft, A.A. Balkema, Rotterdam, 1982, pp. 323-330.

101. Sinha, N.K., "Field Tests on Rate Sensitivity of Vertical Strength and Deformation of First-Year Columnar-Grained Sea Ice," Proceedings of the 7th International Conference on Port and Ocean Engineering Under Arctic Conditions, (POAC 83), Helsinki, Finland, Vol. 1, April 1983, pp. 909-919.

102. Sinha, N.K., "Creep Model of Ice for Monotonically Increasing Stress," Cold Regions Science and Technology, Vol. 8, 1983, pp. 25-33.

103. Smith, G.D. and Morland, L.W., "Viscous Relations for the Steady Creep of Polycrystalline Ice," Cold Regions Science and Technology, Vol. 4, 1981, pp. 141-150.

104. Snyder, M.D. and Bathe, K.J., "A Solution Procedure for Thermo-Elastic-Plastic and Creep Problems," Nuclear Engineering and Design, Vol. 64, 1981, pp. 49-80.

105. Spring, U. and Morland, L.W., "Viscoelastic Solid Relations for the Deformation of Ice," Cold Regions Science and Technology, Vol. 5, 1982, pp. 221-234.

106. Spring, U. and Morland, L.W., "Integral Representation for the Viscoelastic Deformation of Ice," Cold Regions Science and Technology, Vol. 6, 1983, pp. 185-193.

107. St. Lawrence, W.F. and Cole, D.M., "Acoustic Emissions from Polycrystalline Ice," Cold Regions Science and Technology, Vol. 5, 1982, pp. 183-199.

108. Timco, G.W. and Frederking, R., "Confined Compressive Strength of Sea Ice," Proceedings of the 7th International Conference on Port and Ocean Engineering under Arctic Conditions (POAC 83), Helsinki, Finland, Vol. 1, April 1983, pp. 243-253.

109. Timco, G.W. and Frederking, R.M.W., "An Investigation of the Failure Envelope of Granular/Discontinuous Columnar Sea Ice," Cold Regions Science and Technology, Vol. 9, 1984, pp. 17-27.

110. Ting, S.K. and Shyam Sunder, S., "Sea Ice Indentation Accounting for Strain-Rate Variation," Proceedings of the ASCE Specialty Conference: Arctic '85 - Civil Engineering in the Arctic Offshore, San Francisco, California, March 1985, pp. 931-941.

111. Traetteberg, A., Gold, L.W. and Frederking, R., "The Strain Rate and Temperature Dependence of Young's Modulus of Ice," Proceedings of the 3rd International Symposium on Ice Problems, International Association for Hydraulic Research, Hanover, New Hampshire, August 1975, pp. 479-486.

112. Vaudrey, K.D., "Ice Engineering - Study of Related Properties of Floating Sea-Ice Sheets and Summary of Elastic and Viscoelastic Analyses," Technical Report R860, Naval Civil Engineering Laboratory, Port Hueneme, California, December 1977, 81 p.

113. Vittoratos, E.S., "Existence of Oriented Sea Ice by the Mackenzie Delta," Proceedings of the 5th International Conference on Port and Ocean Engineering under Arctic Conditions (POAC 79), Trondheim, Norway, Vol. 1, August 1979, pp. 643-650.

114. Vivatrat, V., "Strains and Strain Rates in Sea Ice Indentation," Offshore Technology Conference, OTC 4311, Houston, Texas, May 1982, pp. 133-140.

115. Vivatrat, V. and Chen, V.L., "Ice Load Prediction with the Use of A Rate-Dependent Anisotropic Constitutive Law," Proceedings of the ASCE Specialty Conference: Arctic '85 - Civil Engineering in the Arctic Offshore, San Francisco, California, March 1985, pp. 942-952.

116. Vivatrat, V., and Slomski, S., "A Probabilistic Basis for Selecting Design Ice Pressures and Ice Loads for Arctic Offshore Structures," Offshore Technology Conference, OTC 4457, Houston, Texas, May 1983, pp. 121-131.

117. Vivatrat, V., Chen, V., and Bruen, F.J., "Ice Load Prediction for Arctic Nearshore Zone," Cold Regions Science and Technology, 1984, 26 p.

118. Wang, Y.S., "Crystallographic Studies and Strength Tests of Field Ice in the Alaskan Beaufort Sea," Proceedings of the 5th International Conference on Port and Ocean Engineering under Arctic Conditions (POAC 79), Trondheim, Norway, August 1979, pp. 651-665.

119. Wang, Y.S., "Sea Ice Properties," Technical Seminar on Alaskan Beaufort Sea Gravel Island Design presented by Exxon Company, U.S.A., Houston, Texas, October 1979.

120. Wang, Y.S., "Uniaxial Compression Testing of Arctic Sea Ice," Proceedings of the 6th International Conference on Port and Ocean Engineering under Arctic Conditions (POAC 81), Universite Laval, Quebec, Canada, July 1981, pp. 346-355.

121. Wang, Y.S., "A Rate-Dependent Stress-Strain Relationship for Sea Ice," Proceedings of the First International Symposium on Offshore Mechanics and Arctic Engineering, ASME, New Orleans, Louisiana, March 1982, pp. 243-248.

122. Watt, B.J., "Design of Prefabricated Offshore Structures for Ice Forces," Design for Ice Forces, A state of the practice report prepared by the Technical Council on Cold Regions Engineering of the American Society of Civil Engineers, edited by S.R. Caldwell and R.D. Crissman, 1983, pp. 17-37.

123. Whang, B., "Elasto-Plastic Analysis of Orthotropic Plates and Shells," Ph.D. Thesis, Department of Civil Engineering, Massachusetts Institute of Technology, Cambridge, Massachusetts, October 1968, 316 p.

124. Weeks, W., and Assur, A., "The Mechanical Properties of Ice," U.S. Army Cold Regions Research and Engineering Laboratory, CRREL Report II-C3, Hanover, New Hampshire, September 1967, 80 p.

125. Weeks, W.F., and Ackley, S.F., "The Growth, Structure, and Properties of Sea Ice," U.S. Army Cold Regions Research and Engineering Laboratory, CRREL Monograph 82-1, Hanover, New Hampshire, November 1982, 130 p.

126. Weeks, W.F. and Gow, A.J., "Preferred Crystal Orientations Along the Margins of the Arctic Ocean," Journal of Geophysical Research, 84(C10), 1978, pp. 5105-5121.

127. Weeks, W.F. and Mellor, M., "Mechanical Properties of Ice in the Arctic Seas," Arctic Technology and Policy, Proceedings of the Second Annual MIT Sea Grant College Program Lecture and Seminar, edited by I. Dyer and C. Chryssostomidis, Massachusetts Institute of Technology, Cambridge, Massachusetts, March 1983, pp. 235-259.

128. Zaretsky, Y.K., Chumichev, B.D. and Solomatin, V.I., "Ice Behavior Under Load," Engineering Geology, Vol. 13, 1979, pp. 299-309.

APPENDIX A

MATRICES USED IN CONSTITUTIVE MODEL

$$\underline{C} = \begin{bmatrix} \frac{1}{E_1} & -\frac{\nu_{12}}{E_2} & -\frac{\nu_{13}}{E_3} & & & \\ -\frac{\nu_{21}}{E_1} & \frac{1}{E_2} & -\frac{\nu_{23}}{E_3} & & \underline{0} & \\ -\frac{\nu_{31}}{E_1} & -\frac{\nu_{32}}{E_2} & \frac{1}{E_3} & & & \\ & & & \frac{2}{G_{12}} & & \\ & \underline{0} & & & \frac{2}{G_{23}} & \\ & & & & & \frac{2}{G_{31}} \end{bmatrix}$$

$$\underline{G} = \begin{bmatrix} \frac{a_1+a_3}{3} & -\frac{a_1}{3} & -\frac{a_3}{3} & & & \\ -\frac{a_1}{3} & \frac{a_1+a_2}{3} & -\frac{a_2}{3} & & \underline{0} & \\ -\frac{a_3}{3} & -\frac{a_2}{3} & \frac{a_2+a_3}{3} & & & \\ & & & 2a_4 & & \\ & \underline{0} & & & 2a_5 & \\ & & & & & 2a_6 \end{bmatrix}$$

$$\underline{H} = \begin{bmatrix} \frac{3(a_1+a_3)a_2^2}{a^{*2}} & -\frac{3a_1a_2a_3}{a^{*2}} & -\frac{3a_1a_2a_3}{a^{*2}} & & & \\ -\frac{3a_1a_2a_3}{a^{*2}} & \frac{3(a_1+a_2)a_3^2}{a^{*2}} & -\frac{3a_1a_2a_3}{a^{*2}} & & \underline{0} & \\ -\frac{3a_1a_2a_3}{a^{*2}} & -\frac{3a_1a_2a_3}{a^{*2}} & \frac{3(a_2+a_3)a_1^2}{a^{*2}} & & & \\ & & & \frac{2}{a_4} & & \\ & \underline{0} & & & \frac{2}{a_5} & \\ & & & & & \frac{2}{a_6} \end{bmatrix}$$

where a^* is given by:

$$a^* = (a_1a_2 + a_2a_3 + a_3a_1)$$

APPENDIX B

ORTHOTROPIC MATERIAL PARAMETERS

B.1 DEFINITION OF SYMBOLS

In order to derive the material parameters it is necessary to choose a reference direction. For this purpose the sea ice is assumed to lie on the y-z plane with its c-axis pointing along the y direction. The stress ratios are calculated using the strengths obtained from the same constant strainrate tests in the respective directions. The number in the parenthesis indicate the normal range of their values.

β_1 = ratio of the stress in x direction to the stress in y direction (2.0-5.0)

β_2 = ratio of the stress in z direction to the stress in y direction (0.5-0.9)

β_3 = ratio of the stress at 45° on y-z plane to the stress in y direction (0.25-0.50)

β_4 = ratio of the stress at 45° on x-y plane to the stress in y direction (0.25-0.50)

β_5 = ratio of the stress at 45° on z-x plane to the stress in y direction (0.25-0.50)

The coefficients, b_1 to b_6, are the constants for the uniaxial power-law (Eq. 5.5) along the y, x and z directions, and the 45° axes on the y-z, x-y and z-x planes respectively. It has been experimentally verified that N is, in general, independent of the loading directions for the orthotropic sea ice. Furthermore, without loss of generality, we can set $a_1=1$.

B.2 UNIAXIAL TEST IN X-DIRECTION

The uniaxial test is performed in the x direction. This implies that only normal stress in the x direction is present and all other stresses are zero. Using Eqs. 5.8 and 5.9 the strainrate in the x direction is given as:

$$\dot{\varepsilon}_{xx} = \frac{3}{a_1+a_2} \, a\sigma_e^{N-1} \left(\frac{a_1+a_3}{3}\right) \sigma_{xx} \tag{B.1}$$

where ε and σ represent the strains and stresses respectively with the subscript indicating their directions. Using Eq. 5.3 the effective stress is obtained as:

$$\sigma_e = \left(\frac{a_1 + a_3}{a_1 + a_2}\right)^{\frac{1}{2}} \sigma_{xx} \tag{B.2}$$

Substituting Eq. B.2 in Eq. B.1 we have, with $a_1=1$:

$$\dot{\varepsilon}_{xx} = a\left(\frac{1 + a_3}{1 + a_2}\right)^{\frac{N+1}{2}} \sigma_{xx}^N \tag{B.3}$$

The uniaxial power-law in the x direction may be written as:

$$\dot{\varepsilon}_{xx} = b_2\sigma^N_{xx} \tag{B.4}$$

Comparing Eqs. B.3 and B.4 and solving for a_2 with $\beta_1=(a/b_2)^{1/N}$, we obtain:

$$a_2 = (1 + a_3)\beta_1^{\frac{2N}{N+1}} - 1 \tag{B.5}$$

B.3 UNIAXIAL TEST IN Z-DIRECTION

Using Eqs. 5.8 and 5.9 and proceeding as before we have:

$$\dot{\varepsilon}_{xx} = \frac{a_2 + a_3}{a_1 + a_2} a\sigma_e^{N-1} \sigma_{zz} \tag{B.6}$$

The effective stress is given by:

$$\sigma_e = (\frac{a_2 + a_3}{a_1 + a_2})^{\frac{1}{2}} \sigma_{zz} \tag{B.7}$$

Substituting Eq. B.7 in Eq. B.6 we get:

$$\dot{\varepsilon}_{zz} = a(\frac{a_2 + a_3}{1 + a_2})^{\frac{N+1}{2}} \sigma_{zz}^n \tag{B.8}$$

The uniaxial power-law in the z direction may be written as:

$$\dot{\varepsilon}_{zz} = b_3\sigma^N_{zz} \tag{B.9}$$

Comparing Eqs. B.8 and B.9, with $\beta_2=(a/b_3)^{1/N}$, we have:

$$a_2 = (a_2 + a_3)\beta_2^{\frac{2N}{N+1}} - 1 \tag{B.10}$$

It is now possible to express the orthotropic material parameters, a_2 and a_3, in terms of the β_i's. Solving Eqs. B.5 and B.10 for a_2 and a_3 in terms of β_1 and β_2, we obtain:

$$a_1 = 1 \tag{B.11}$$

$$a_2 = - \frac{\beta_1^{\frac{2N}{N+1}} - \beta_2^{\frac{2N}{N+1}}(1 - \beta_1^{\frac{2N}{N+1}})}{\beta_1^{\frac{2N}{N+1}} - \beta_2^{\frac{2N}{N+1}}(1 + \beta_1^{\frac{2N}{N+1}})} \tag{B.12}$$

$$a_3 = - \frac{\beta_1^{\frac{2N}{N+1}} + \beta_2^{\frac{2N}{N+1}}(1 - \beta_1^{\frac{2N}{N+1}})}{\beta_1^{\frac{2N}{N+1}} - \beta_2^{\frac{2N}{N+1}}(1 + \beta_1^{\frac{2N}{N+1}})} \tag{B.13}$$

B.4 UNIAXIAL TEST AT 45° ON Y-Z PLANE

In this test, the stress, applied at 45° to the coordinate axes in the y-z plane, is denoted by σ_{45}. The corresponding strain is denoted by ε_{45}. The effective stress is computed using Eq. 5.3 after performing a Mohr's circle transformation and is given by:

$$\sigma_e^2 = \frac{3}{1 + a_2} \left(\frac{1 + a_3}{3} + 2a_5\right) \frac{\sigma_{45}^2}{4} \tag{B.14}$$

Using Eqs. 5.8 and 5.9, the inplane strains are computed as:

$$\dot{\varepsilon}_{yy} = K\frac{a_1}{6}\,\sigma_{45}^{N} \tag{B.15}$$

$$\dot{\varepsilon}_{zz} = K\frac{a_3}{6}\,\sigma_{45}^{N} \tag{B.16}$$

$$\dot{\varepsilon}_{yz} = K\frac{a_5}{2}\,\sigma_{45}^{N} \tag{B.17}$$

where

$$K = a\left(\frac{3}{a_1 + a_2}\right)^{\frac{N+1}{2}}\left(\frac{a_1 + a_3}{3} + 2a_5\right)^{\frac{N-1}{2}}\left(\frac{1}{2}\right)^{N-1}$$

Using Mohr's transformation, the strainrate at 45° to the coordinate axes is obtained as:

$$\dot{\varepsilon}_{45} = \frac{1}{4}\left(\frac{a_1 + a_3}{3} + 2a_5\right)K\sigma_{45}^{N} \tag{B.18}$$

The uniaxial power-law may be written as:

$$\dot{\varepsilon}_{45} = b_4\sigma^{N}{}_{45} \tag{B.19}$$

Comparing Eqs. B.18 and B.19 with $\beta_3=(a/b_4)^{1/N}$ and $n=2N/(N+1)$, we get:

$$a_5 = \frac{1 + a_2}{6}\left(4\beta_3^{-n} - \beta_1^{-n}\right) \tag{B.20}$$

In order to obtain parameters a_4 and a_6, similar 45° tests are conducted in the x-y and z-x planes respectively.

These parameters can be expressed in terms of the β_i's in the same way as a_5 and are given as follows:

$$a_4 = \frac{1 + a_2}{6} (4\beta_4^{-n} - \beta_2^{-n}) \tag{B.21}$$

$$a_6 = \frac{1 + a_2}{6} (4\beta_5^{-n} - 1) \tag{B.22}$$

For a transversely isotropic case, $\beta_2=\beta_3=1$ and $\beta_4=\beta_5$. This simplifies Eqs. B.11-B.13 and Eqs. B.20-B.22 and they are summarized as follows:

$$a_1 = 1 \tag{B.23}$$

$$a_2 = 2\beta_1^n - 1 \tag{B.24}$$

$$a_3 = 1 \tag{B.25}$$

$$a_4 = \frac{2\beta_1^n}{6} [4\beta_4^{-n} - 1] \tag{B.26}$$

$$a_5 = \frac{2\beta_1^n}{6} [4 - \beta_1^{-n}] \tag{B.27}$$

$$a_6 = \frac{2\beta_1^n}{6} [4\beta_5^{-n} - 1] \tag{B.28}$$

APPENDIX C

FREDERKING'S TESTS

C.1 TYPE A TEST

The ice sheet is considered to be in the y-z plane. The x axis is assumed to represent the out-of-plane direction. The sea ice is considered to be transversely isotropic i.e., its properties are same in any direction along the y-z plane. The ice sheet is subjected to normal stress σ_{yy} in the y direction, and its in-plane movement in the z direction, perpendicular to the direction of application of σ_{yy}, is restrained. Furthermore, stresses in the x direction are assumed to be zero. These imply:

$$\sigma_{xx} = 0 \tag{C.1}$$

$$\dot{\varepsilon}_{zz} = 0 \tag{C.2}$$

Using Eqs. 5.8, 5.9 and C.2 we have:

$$\sigma_{zz} = \frac{a_2}{a_2 + a_3}\sigma_{yy} \tag{C.3}$$

Using Eqs. 5.3 and C.3 we obtain:

$$\sigma_e = \frac{1}{\sqrt{(1 + a_2)}} \left(1 + \frac{a_2 a_3}{a_2 + a_3}\right)^{\frac{1}{2}} \sigma_{yy} \tag{C.4}$$

Using Eqs. 5.8 and 5.9 we have:

$$\dot{\varepsilon}_{yy} = a\left[\frac{1}{1 + a_2}\left(1 + \frac{a_2 a_3}{a_2 + a_3}\right)\right]^{\frac{N+1}{2}} (\sigma^c_{yy})^N \qquad (C.5)$$

where the superscript c on σ_{yy} implies that it is confined. For an unconfined test we have:

$$\dot{\varepsilon}_{yy} = a(\sigma^u_{yy})^N \qquad (C.6)$$

where the superscript u on σ_{yy} implies that it is unconfined.

Now if the strainrates are the same, then, we can equate Eqs. C.4 and C.5 to obtain the following ratio:

$$\gamma_z = \frac{\sigma^c_{yy}}{\sigma^u_{yy}} = \left[\frac{1}{1 + a_2}\left(1 + \frac{a_2 a_3}{a_2 + a_3}\right)\right]^{-\frac{N+1}{2N}} \qquad (C.7)$$

For the case of transverse isotropy, a3=1, and Eq. C.7 simplifies to:

$$\gamma_z = \left[\frac{(1 + a_2)^2}{1 + 2a_2}\right]^{\frac{N+1}{2N}} \qquad (C.8)$$

C.2 TYPE B TEST

The load is applied in the y direction. However, in this test, stresses in the z direction are assumed to be zero. Furthermore, displacements are restrained in the x direction. These imply:

$$\sigma_{zz} = 0 \qquad (C.9)$$

$$\dot{\varepsilon}_{xx} = 0 \qquad (C.10)$$

Using Eqs. 5.8, 5.9 and C.10 we obtain:

$$\sigma_{xx} = \frac{a_1}{a_1 + a_3}\sigma_{yy} \tag{C.11}$$

and from Eqs. 5.3 and C.11 we have:

$$\sigma_e = \frac{1}{\sqrt{(1 + a_2}} \left(\frac{a_3}{1 + a_3} + a_2\right)^{\frac{1}{2}} \sigma_{yy} \tag{C.12}$$

Using Eqs. 5.8 and 5.9 we have:

$$\dot{\varepsilon}_{yy} = a \left[\frac{1}{1 + a_2} \left(\frac{a_3}{1 + a_3} + a_2\right)\right]^{\frac{N+1}{2}} (\sigma^c_{yy})^N \tag{C.13}$$

For an unconfined test we have:

$$\dot{\varepsilon}_{yy} = a(\sigma^u_{yy})^N \tag{C.14}$$

Now, we equate Eqs. C.13 and C.14 for the same strainrates and obtain:

$$\gamma_x = \frac{\sigma^c_{yy}}{\sigma^u_{yy}} = \left[\frac{1}{1 + a_3} \left(\frac{a_3}{1 + a_3} + a_2\right)\right]^{-\frac{N+1}{2N}} \tag{C.15}$$

For transverse isotropy, $a_3 = 1$, and Eq. C.15 simplifies to:

$$\gamma_x = \left[\frac{2(1 + a_2)}{1 + 2a_2}\right]^{\frac{N+1}{2N}} \tag{C.16}$$

C.3 TRIAXIAL TEST

In the triaxial test of a transversely isotropic ice sheet subjected to a normal stress σ in the y direction, we have the following stress state:

$$\begin{aligned} \sigma_{yy} &= \sigma \\ \sigma_{zz} = \sigma_{xx} &= \tau\sigma \\ \sigma_{xy} = \sigma_{yz} = \sigma_{zx} &= 0 \end{aligned} \tag{C.17}$$

where τ = ratio of confining stress to axial stress. Using the above relations in the definition of the effective stress as given in Eq. 5.3 we get:

$$\sigma_e = (1-\tau)\sigma \tag{C.18}$$

Next the strainrate in the y direction is obtained from Eqs. 5.8 and 5.9 as follows:

$$\dot{\varepsilon}_{yy} = a(1-\tau)^N(\sigma^{tr}_{yy})^N \tag{C.19}$$

Furthermore

$$\dot{\varepsilon}_{yy} = a(\sigma^u_{yy})^N \tag{C.20}$$

From the above two equations we have the following ratio:

$$\gamma_t = \frac{\sigma^{tr}_{yy}}{\sigma^u_{yy}} = \frac{1}{1-\tau} \tag{C.21}$$

Also,

$$\frac{\sigma_{yy}-\sigma_{zz}}{\sigma^u_{yy}} = \frac{(1-\tau)\sigma^{tr}_{yy}}{\sigma^u_{yy}} = 1 \tag{C.22}$$

APPENDIX D

UPPER BOUND SOLUTION

D.1 VELOCITY AND STRAINRATE FIELD

The kinematic model is obtained by superposition of a uniform flow and a doublet. This resembles the flow of an infinite ice sheet past a circular indenter with the interface boundary condition similar to the roller condition. The velocity and strain rate field in polar coordinates is given by:

$$U_r = U\left(1 - \frac{r_0^2}{r^2}\right) \mathrm{Cos}\,\theta \tag{D.1}$$

$$U_\theta = -U\left(1 + \frac{r_0^2}{r^2}\right) \mathrm{Sin}\,\theta \tag{D.2}$$

$$\dot{\varepsilon}_r = \frac{\partial U_r}{\partial r} = \frac{2Ur_0^2}{r^3} \mathrm{Cos}\,\theta \tag{D.3}$$

$$\dot{\varepsilon}_\theta = \frac{U_r}{r} + \frac{\partial U_0}{r\,\partial\theta} = -\frac{2Ur_0^2}{r^3} \mathrm{Cos}\,\theta \tag{D.4}$$

$$2\dot{\varepsilon}_{r\theta} = \dot{\gamma}_{r\theta} = \frac{\partial U_r}{r\,\partial\theta} + \frac{\partial U_\theta}{\partial r} - \frac{U_\theta}{r} = \frac{4Ur_0^2}{r^3} \mathrm{Sin}\,\theta \tag{D.5}$$

where r_0 is the radius of the indenter. In Cartesian coordinates, the above set of equations can be written as:

$$U_{yy} = U[1+ \frac{r_0^2(z^2 - y^2)}{(y^2 + z^2)^2}] \qquad (D.6)$$

$$U_{zz} = - \frac{2Ur_0^2yz}{(y^2 + z^2)^2} \qquad (D.7)$$

$$\dot{\varepsilon}_{yy} = \frac{\partial U_{yy}}{\partial y} = \frac{2Ur_0^2y(y^2 - 3z^2)}{(y^2 + z^2)^3} \qquad (D.8)$$

$$\dot{\varepsilon}_{zz} = \frac{\partial U_z}{\partial z} = - \frac{2Ur_0^2y(y^2 - 3z^2)}{(y^2 + z^2)^3} \qquad (D.9)$$

$$\dot{\varepsilon}_{yz} = \frac{\dot{\gamma}_{yz}}{2} = \frac{1}{2} (\frac{\partial U_y}{\partial z} + \frac{\partial U_z}{\partial y}) = \frac{2Ur_0^2z(z^2 - 3y^2)}{(y^2 + z^2)^3} \qquad (D.10)$$

Under plane strain condition, we have the following:

$$\dot{\varepsilon}_{xx} = \dot{\varepsilon}_{xy} = \dot{\varepsilon}_{xz} = 0 \qquad (D.11)$$

The strains may also be expressed in terms of r and θ as:

$$\dot{\varepsilon}_{yy} = \frac{2Ur_0^2\mathrm{Cos}3\theta}{r^3} \qquad (D.12)$$

$$\dot{\varepsilon}_{zz} = - \frac{2Ur_0^2\mathrm{Cos}3\theta}{r^3} \qquad (D.13)$$

$$\dot{\varepsilon}_{yz} = \frac{2Ur_0^2\mathrm{Sin}3\theta}{r^3} \qquad (D.14)$$

D.2 CONSTITUTIVE MODEL

Equations 5.8 and 5.10 are now presented in a slightly different form containing all the nine components. Note that the strains and the pseudo deviatoric stresses are now tensor quantities. To distinguish this, superscripts ^ are used on $\underline{S}$ and $\underline{G}$.

$$\underline{\dot{\varepsilon}}_{cr} = \lambda\ \underline{\hat{S}} \qquad \text{(D.15)}$$

$$\underline{\hat{S}} = \underline{\hat{G}}\ \underline{\sigma} \qquad \text{(D.16)}$$

where $\underline{\hat{G}}$ is given by:

$$\underline{\hat{G}} = \begin{bmatrix} \frac{a_1+a_3}{3} & -\frac{a_1}{3} & -\frac{a_3}{3} & & & & & & \\ -\frac{a_1}{3} & \frac{a_1+a_2}{3} & -\frac{a_2}{3} & & & \underline{0} & & & \\ -\frac{a_3}{3} & -\frac{a_2}{3} & \frac{a_2+a_3}{3} & & & & & & \\ & & & a_4 & & & & & \\ & & & & a_5 & & & & \\ & & & & & a_6 & & & \\ & \underline{0} & & & & & a_4 & & \\ & & & & & & & a_5 & \\ & & & & & & & & a_6 \end{bmatrix}$$

Further, the effective strainrate is obtained from:

$$\dot{\varepsilon}_e^2 = \frac{\beta}{3}\ \underline{\dot{\varepsilon}}^T\ \underline{\hat{H}}\ \underline{\dot{\varepsilon}} \qquad \text{(D.17)}$$

where $\beta = a_1 + a_2$ and $\underline{\hat{H}}$ is given by:

$$\underline{\hat{H}} = \begin{bmatrix} \frac{3(a_1+a_3)a_2^2}{a^{*2}} & -\frac{3a_1a_2a_3}{a^{*2}} & -\frac{3a_1a_2a_3}{a^{*2}} & & & & & & \\ -\frac{3a_1a_2a_3}{a^{*2}} & \frac{3(a_1+a_2)a_3^2}{a^{*2}} & -\frac{3a_1a_2a_3}{a^{*2}} & & & & \underline{0} & & \\ \frac{3a_1a_2a_3}{a^{*2}} & -\frac{3a_1a_2a_3}{a^{*2}} & \frac{3(a_2+a_3)a_1^2}{a^{*2}} & & & & & & \\ & & & \frac{1}{a_4} & & & & & \\ & & & & \frac{1}{a_5} & & & & \\ & \underline{0} & & & & \frac{1}{a_6} & & & \\ & & & & & & \frac{1}{a_4} & & \\ & & & & & & & \frac{1}{a_5} & \\ & & & & & & & & \frac{1}{a_6} \end{bmatrix}$$

where a* is given by:

$$a^* = (a_1a_2 + a_2a_3 + a_3a_1) \qquad \text{(D.18)}$$

Furthermore,

$$\lambda = \frac{3}{\beta}\,\frac{\dot{\varepsilon}_e}{\sigma_e} = \frac{3}{\beta}a^{\frac{1}{N}}\,\dot{\varepsilon}_e^{\,1-\frac{1}{N}} \qquad \text{(D.19)}$$

The strainrates are then given by:

$$\underline{\dot{\varepsilon}} = \frac{3}{\beta}\,a^{\frac{1}{N}}\,\dot{\varepsilon}_e^{\,1-\frac{1}{N}}\,\underline{\hat{S}} \qquad \text{(D.20)}$$

The components of the strainrate tensor are as follows:

$$\underline{\dot{\varepsilon}} = \frac{3}{\beta}a^{\frac{1}{N}}\dot{\varepsilon}_e^{\,1-\frac{1}{N}} \begin{bmatrix} \frac{a_1+a_3}{3}\sigma_{xx} - \frac{a_1}{3}\sigma_{yy} - \frac{a_3}{3}\sigma_{zz} \\ -\frac{a_1}{3}\sigma_{xx} + \frac{a_1+a_2}{3}\sigma_{yy} - \frac{a_2}{3}\sigma_{zz} \\ -\frac{a_3}{3} - \frac{a_2}{3}\sigma_{yy} + \frac{a_2+a_3}{3}\sigma_{zz} \\ a_4\sigma_{xy} \\ a_5\sigma_{yz} \\ a_6\sigma_{zx} \\ a_4\sigma_{yx} \\ a_5\sigma_{zy} \\ a_6\sigma_{xz} \end{bmatrix} \qquad \text{(D.21)}$$

Equation D.21 can be rearranged to give $\underline{\hat{S}}$ in terms of $\underline{\dot{\varepsilon}}$:

$$\underline{\hat{S}} = \frac{1}{\lambda}\,\underline{F}\,\underline{\dot{\varepsilon}} \qquad \text{(D.22)}$$

where

$$\underline{F} = \begin{bmatrix} \frac{2a_2}{a^*} & -\frac{a_3}{a^*} & -\frac{a_1}{a^*} & & & & & & \\ -\frac{a_2}{a^*} & \frac{2a_3}{a^*} & -\frac{a_1}{a^*} & & & 0 & & & \\ \frac{a_2}{a^*} & -\frac{a_3}{a^*} & \frac{2a_1}{a^*} & & & & & & \\ & & & \frac{1}{a_4} & & & & & \\ & & & & \frac{1}{a_5} & & & & \\ & 0 & & & & \frac{1}{a_6} & & & \\ & & & & & & \frac{1}{a_4} & & \\ & & & & & & & \frac{1}{a_5} & \\ & & & & & & & & \frac{1}{a_6} \end{bmatrix}$$

D.3 GLOBAL FORCE

The global force is estimated by the upper bound method (energy approach) using:

$$PU \leq \int_V \underline{S}^T \underline{\dot{\varepsilon}} dV \tag{D.23}$$

Using Eq. D.22 in Eq. D.23 we obtain:

$$PU \leq \int_V \frac{1}{\lambda} \underline{\dot{\varepsilon}}^T \underline{F} \, \underline{\dot{\varepsilon}} \, dV \tag{D.24}$$

Substituting the expressions for $\dot{\underline{\varepsilon}}$, Eqs. D.8-D.11, and $\underline{F}$, and simplifying, we have:

$$\int_V \hat{\underline{S}}^T \dot{\underline{\varepsilon}} dV = \int_V \frac{U^2 r_0^4}{\lambda(y^2+ z^2)^6}\left[\frac{12y^2(y^2-3z^2)^2(a_1+a_3)}{a^*} + \frac{8z^2(z^2- 3y^2)^2}{a_5}\right]dV \tag{D.25}$$

Equation D.25 can be written in polar coordinates as:

$$\int_V \hat{\underline{S}}^T \dot{\underline{\varepsilon}} dV = \int_V \frac{4U^2 r_0^4}{\lambda r^6}\left[\frac{3(a_1+a_3)}{a^*}\mathrm{Cos}^2 3\theta + \frac{2}{a_5}\mathrm{Sin}^2 3\theta\right]dV \tag{D.26}$$

Now, the effective strainrate, $\dot{\varepsilon}_e$, is needed to evaluate λ and is given in polar co-ordinates as follows:

$$\dot{\varepsilon}_e^2 = \frac{\beta}{3}\,\frac{4U^2 r_0^4}{r^6}\left[\frac{3(a_1 a_3^2 + a_2 a_3^2 + a_2 a_1^2 + a_3 a_1^2 + 2a_1 a_2 a_3)}{a^{*2}}\mathrm{Cos}^2 3\theta + \frac{2}{a_5}\mathrm{Sin}^2 3\theta\right] \tag{D.27}$$

For transversely isotropic material, $a_1=a_3=1$, $a_5=(1+2a_2)/3$. Equation D.27 simplifies to:

$$\dot{\varepsilon}_e^2 = \frac{\beta}{3}\,\frac{6}{1 + 2a_2}\,\frac{4U^2 r_0^4}{r^6} \tag{D.28}$$

Substituting Eq. D.28 in Eq. D.19 we obtain the following expression for λ:

$$\lambda = \frac{3}{\beta} \; a^{\frac{1}{N}} \left[\frac{8\beta}{(1 + 2a_2)} \; \frac{U^2 r_0^4}{r^6} \right]^{\frac{N-1}{2N}} \qquad \text{(D.29)}$$

Finally for transverse isotropy, Eq. D.26 reduces to:

$$\int_V \underline{\hat{S}}^T \underline{\dot{\varepsilon}} \; dV = \int_V \frac{24U^2 r_0^4}{\lambda r^6 (1 + 2a_2)} \; dV \qquad \text{(D.30)}$$

Substituting the expression for λ into Eq. D.30 and evaluating the integral, we obtain:

$$\int_V \underline{\hat{S}}^T \underline{\dot{\varepsilon}} \; dV = \left[\frac{3\beta}{2(1 + 2a_2)} \right]^{\frac{1+N}{2N}} \frac{4}{\sqrt{3}} \; U \left[\frac{4}{\sqrt{3}} \; \frac{1}{a} \; \frac{U}{r_0} \right]^{\frac{1}{N}} 2r_0 t \pi \left(\frac{N}{N + 3} \right) \qquad \text{(D.31)}$$

where t is the thickness of the ice sheet. Finally introducing $D=2r_0$ and $\beta=a_1+a_2$ we have the following upper bound solution:

$$\frac{P}{Dt} = \left[\frac{3(1+ a_2)}{2(1+ 2a_2)} \right]^{\frac{1+N}{2N}} \frac{4}{\sqrt{3}} \pi \left(\frac{N}{N + 3} \right) \left(\frac{4}{\sqrt{3}} \; \frac{1}{a} \; \frac{2U}{D} \right)^{\frac{1}{N}} \qquad \text{(D.32)}$$

APPENDIX E

NONLINEAR EQUATION SOLVER

The incremental elastic stress is given by:

$$\Delta\underline{\sigma} = \underline{D}\;\underline{B}\;\Delta\underline{U} - \underline{D}\;\Delta\underline{\varepsilon}_{cr} \tag{E.1}$$

where $\underline{\varepsilon}_{cr}$ is the incremental creep vector which is given by:

$$\Delta\underline{\varepsilon}_{cr} = \Delta t\,\lambda_{\alpha}\underline{S}_{\alpha} \tag{E.2}$$

Equation E.1 can be rewritten as

$$\underline{f}(\Delta\underline{\sigma}) = \Delta\underline{\sigma} - \underline{D}\;\underline{B}\;\Delta\underline{u} - \underline{D}\;\Delta\underline{\varepsilon}_{cr} = 0 \tag{E.3}$$

Expanding Eq. E.3 using Taylor's series and retaining only the first two terms as in the Newton-Rhapson method, we have:

$$[\Delta\underline{\sigma} - \underline{D}\;\underline{B}\;\Delta\underline{U} + \underline{D}\;\Delta\underline{\varepsilon}_{cr}]^{k} + \frac{\partial\underline{f}}{\partial\Delta\underline{\sigma}^{T}}\left(\Delta\underline{\sigma}^{k+1} - \Delta\underline{\sigma}^{k}\right) = \underline{0} \tag{E.4}$$

Note that:

$$\Delta\underline{\sigma}^{k} = \underline{\sigma}^{k}_{i+1} - \underline{\sigma}_{i} \tag{E.5}$$

$$\Delta\underline{\sigma}^{k+1} = \underline{\sigma}^{k+1}_{i+1} - \underline{\sigma}_{i} \tag{E.6}$$

$$\Delta\underline{\sigma}^{k+1} - \Delta\underline{\sigma}^{k} = \underline{\sigma}^{k+1}_{i+1} - \underline{\sigma}^{k}_{i+1} \tag{E.7}$$

Since the stresses are known at iteration i, i.e., σ_i is known, it follows from Eqs. E.4-E.7 that

$$d\,\Delta\underline{\sigma} = d\underline{\sigma}_{i+1} \tag{E.8}$$

Substituting Eq. E.5 into Eq. E.7, we obtain:

$$\underline{\sigma}^{k}_{i+1} - \underline{\sigma}_{i} - [\underline{D}\;\underline{B}\;\Delta\underline{U} + \underline{D}\;\Delta\underline{\varepsilon}_{cr}]^{k} + \left[\frac{\partial\underline{f}}{\partial\underline{\sigma}^{T}_{i+1}}\right]^{k}\left(\underline{\sigma}^{k+1}_{i+1} - \underline{\sigma}^{k}_{i+1}\right) = 0 \tag{E.9}$$

Further, from Eq. E.3 we have:

$$\left[\frac{\partial \underline{f}}{\partial \Delta \underline{\sigma}^T}\right]^k = \left[\underline{I} + \underline{D}\,\frac{\partial \Delta \underline{\varepsilon}_{cr}}{\partial \Delta \underline{\sigma}^T}\right]^k \tag{E.10}$$

Introducing Eq. E.10 in Eq. E.9 we have:

$$\left[\underline{I} + \underline{D}\frac{\partial \Delta \underline{\varepsilon}_{cr}}{\partial \underline{\sigma}^T_{i+1}}\right]^k \underline{\sigma}^{k+1}_{i+1} = \underline{\sigma}_i + \underline{D}[\underline{B}\ \ \Delta \underline{U} - \Delta \underline{\varepsilon}^k_{cr}] + \underline{D}\left[\frac{\partial \Delta \underline{\varepsilon}_{cr}}{\partial \underline{\sigma}^T_{i+1}}\right]^k \underline{\sigma}^k_{i+1} \tag{E.11}$$

Using the α method we may write:

$$\underline{\sigma}_\alpha = (1-\alpha)\ \underline{\sigma}_i + \alpha\ \underline{\sigma}_{i+1} \tag{E.12}$$

From Eq. E.12 it immediately follows:

$$d\underline{\sigma}_\alpha = \alpha\ d\underline{\sigma}_{i+1} \tag{E.13}$$

In Eq. E.11, the only term that remains to be evaluated is $\frac{\partial \Delta \underline{\varepsilon}_{cr}}{\partial \underline{\sigma}^T_{i+1}}$. This quantity is evaluated as follows:

$$\frac{\partial \Delta \underline{\varepsilon}_{cr}}{\partial \underline{\sigma}^T_{i+1}} = \alpha\ \frac{\partial \Delta \underline{\varepsilon}_{cr}}{\partial \underline{\sigma}^T_{\alpha}} \tag{E.14}$$

and

$$\frac{\partial \Delta \underline{\varepsilon}_{cr}}{\partial \underline{\sigma}^T_{\alpha}} = \Delta t\ \left[\lambda \hat{\underline{G}} + \frac{3}{a_1 + a_2}\ \sigma_e^{-1}\ \ \frac{\partial \lambda}{\partial \sigma_e} \hat{\underline{S}}\ \hat{\underline{S}}^T\right]^k_\alpha \tag{E.15}$$

Equation E.11 can now be solved for the stress by iteration.

APPENDIX F

ANALYTICAL TESTS FOR CODE VERIFICATION

Let the test sample, which is restrained in the z direction, be subjected to a constant stress in the y direction σ_y. Using Eq. 5.3 and accounting for transverse isotropy the effective stress σ_e is obtained:

$$\sigma_e = \left(\sigma_{yy}^2 + \sigma_{zz}^2 - \frac{2a_2}{1+a_2}\sigma_{yy}\sigma_{zz}\right) \qquad \text{(F.1)}$$

From Eqs. 5.8 and 5.9 the creep strain in the y and z directions, i.e., ε_{yy} and ε_{zz} respectively, are given by:

$$\dot{\varepsilon}_{yy,cr} = \lambda\left(\frac{a_1+a_2}{3}\sigma_{yy} - \frac{a_2}{3}\sigma_{zz}\right) \qquad \text{(F.2)}$$

$$\dot{\varepsilon}_{zz,cr} = \lambda\left(-\frac{a_2}{3}\sigma_{yy} + \frac{a_2+a_3}{3}\sigma_{zz}\right) \qquad \text{(F.3)}$$

Since the test sample is restrained in the z direction, ε_{zz} is zero. This implies:

$$\frac{\dot{\sigma}_{zz}}{E} + \dot{\varepsilon}_{zz,cr} = 0 \qquad \text{(F.4)}$$

Substituting Eq. F.4 in Eq. F.3, we obtain the following differential equation:

$$\dot{\sigma}_{zz} + E\lambda \frac{a_2+a_3}{3} \sigma_z = E\lambda \frac{a_2}{3}\sigma_{yy} \quad (F.5)$$

Assuming λ to be constant, the solution to the above differential equation is given by:

$$\sigma_{zz} = Ce^{-E\lambda\frac{a_2+a_3}{3}t} + \frac{a_2}{a_2+a_3}\sigma_{yy} \quad (F.6)$$

where C is a constant. At time t=0, we assume that there is no creep and hence there is no creep stress in the z direction. This implies:

$$\sigma_{zz}(t=0) = \nu\sigma_{yy} \quad (F.7)$$

Using Eqs. G.6 and G.7 we get,

$$C = (\nu - \frac{a_2}{a_2+a_3}) \quad (F.8)$$

Hence the solution to the differential equation, Eq. F.5, is given by:

$$\sigma_{zz} = - [(\frac{a_2}{a_2+a_3} - \nu) e^{- E\lambda\frac{a_2+a_3}{3}t} + \frac{a_2}{a_2+a_3}] \quad (F.9)$$